Remote Sensing For Vital Signs Monitoring

Using Advanced Radar Signal Processing Techniques

by

Yu Rong

A Dissertation Presented in Partial Fulfillment
of the Requirements for the Degree
Doctor of Philosophy

Approved November 2018 by the
Graduate Supervisory Committee:

Daniel W. Bliss, Chair
Christ D. Richmond
Cihan Tepedelenlioglu
Ahmed Alkhateeb

ARIZONA STATE UNIVERSITY

December 2018

ABSTRACT

In the past half century, low-power wireless signals from portable radar sensors, initially continuous-wave (CW) radars and more recently ultra-wideband (UWB) radar systems, have been successfully used to detect physiological movements of stationary human beings.

The thesis starts with a careful review of existing signal processing techniques and state of the art methods possible for vital signs monitoring using UWB impulse systems. Then an in-depth analysis of various approaches is presented.

Robust heart-rate monitoring methods are proposed based on a novel result: spectrally the fundamental heartbeat frequency is respiration-interference-limited while its higher-order harmonics are noise-limited. The higher-order statistics related to heartbeat can be a robust indication when the fundamental heartbeat is masked by the strong lower-order harmonics of respiration or when phase calibration is not accurate if phase-based method is used. Analytical spectral analysis is performed to validate that the higher-order harmonics of heartbeat is almost respiration-interference free. Extensive experiments have been conducted to justify an adaptive heart-rate monitoring algorithm. The scenarios of interest are, 1) single subject, 2) multiple subjects at different ranges, 3) multiple subjects at same range, and 4) through wall monitoring.

A remote sensing radar system implemented using the proposed adaptive heart-rate estimation algorithm is compared to the competing remote sensing technology, a remote imaging photoplethymography (RIPPG) system, showing promising results.

State of the art methods for vital signs monitoring are fundamentally related to process the phase variation due to vital signs motions. Their performance are determined by a phase calibration procedure. Existing methods fail to consider the time-varying nature of phase noise. There is no prior knowledge about which of the corrupted complex signals, in-phase component (I) and quadrature component (Q),

need to be corrected. A precise phase calibration routine is proposed based on the respiration pattern. The I/Q samples from every breath are more likely to experience similar motion noise and therefore they should be corrected independently. High slow-time sampling rate is used to ensure phase calibration accuracy. Occasionally, a 180-degree phase shift error occurs after the initial calibration step and should be corrected as well. All phase trajectories in the I/Q plot are only allowed in certain angular spaces. This precise phase calibration routine is validated through computer simulations incorporating a time-varying phase noise model, controlled mechanic system, and human subject experiment.

ACKNOWLEDGMENTS

I would like to express my sincere gratitude to my PhD advisor Prof. Daniel W. Bliss for his advice, encouragement, and monitoring in the past a few years. I have truly enjoyed doing research under his guidance over the years on radar theory and applied applications. I have been involved in and worked on different projects throughout my PhD study. These projects range from theoretical study in statistical array processing [1–7] and spectral sharing between radar and communications systems [8, 9], to experimental study in drone-based channel phenomenology analysis [10, 11] and remote sensing for vital signs [12–17].

I am also thankful to my colleagues (Alex Chiriath, Andrew Herschfelt, Richard Gutierrez, Hanguang Yu, Wylie Standage-Beier, Sharanya Srinivas, Owen Ma, Arindam Dutta, Christian Chapman, Gerard Gubash, Matthew Kinsinger, Yang Li, Sean Bryan) in Bliss Laboratory of Information Signals, and Systems, Center for Wireless Information Systems and Computational Architectures, Arizona State University. I am very grateful for all the help and happiness they offered.

I would like to thank my wife and my parents for their encouragement and unconditional support. I dedicate this thesis to my family, whose love gives me the courage to my life.

TABLE OF CONTENTS

Page

LIST OF FIGURES vii

LIST OF TABLES xii

CHAPTER

1 INTRODUCTION 1

1.1 Introduction 1

1.2 Contributions 2

1.3 Background 2

2 TECHNOLOGIES FOR VITAL SIGNS MONITORING 6

2.1 Ultra-Wideband Sensing Technology 7

2.2 System Concept 9

2.3 Previous Works 10

3 STATE OF THE ART: RADAR SIGNAL PROCESSING TECHNIQUES FOR VITAL SIGNS EXTRACTION 12

3.1 UWB Signal Model 12

3.2 Direct RF Method 13

3.3 I/Q Channels-Based Methods 14

3.4 Phase-Based Methods 15

3.4.1 Arctangent Demodulation Method 16

3.4.2 Logarithm Method 17

3.4.3 Differentiate and Cross-Multiply (DACM) Method 18

3.4.4 Phase Calibration Technique 19

3.5 Subspace-Based Methods 20

3.5.1 State-Space Method 21

3.5.2 Multiple-Signal Classification Algorithm 24

CHAPTER Page

3.6 Our Approach 26
4 ROBUST HEART-RATE MONITORING METHODS 27
4.1 Harmonics-Based Heartbeat Detection 27
4.2 Advantages: Free of Respiration Harmonics 28
4.3 Robustness Analysis 32
4.3.1 Two-Subject at Same Range 32
4.3.2 Small-scale Motion Resistance 35
4.4 Limitation Analysis 36
4.5 An Adaptive Heart-Rate Combination Algorithm 38
4.5.1 Spectral Peak Selection Criterion 39
4.5.2 Adaptive Heart Rate Selection Scheme 40
5 A PRECISE PHASE CALIBRATION ALGORITHM FOR IMPROVED HEARTBEAT DETECTION 44
5.1 Respiration Modeling 45
5.2 Sources of Phase Noises 45
5.3 Simulation Analysis 46
5.4 Proposed Phase Calibration Criteria 48
5.5 Automated Phase Calibration Algorithm 48
6 MEASUREMENT SYSTEMS 53
6.1 Radar Sensor Parameters 54
6.1.1 System Features: Vital Signs Radar 55
6.2 Remote Imaging PPG System 55
6.2.1 Principle of Operation 58
6.2.2 Signal Model 59

CHAPTER Page

6.3 Standard Reference Devices 61
7 RESEARCH HIGHLIGHT: HEART-RATE DETECTION/MONITORING PERFORMANCE DEMONSTRATION 63
7.1 A Comparative Study 63
7.1.1 1-D Spectral Analysis 63
7.1.2 2-D Time-Frequency Analysis 67
7.2 Continuous Heart-Rate Monitoring Performance 72
7.2.1 Single Subject 72
7.2.2 Multiple Subjects 74
7.3 Comparison With Existing Remote Sensing Technology 77
7.4 Through Wall Heart-Rate Monitoring 81
7.4.1 Single Subject 83
7.4.2 Multiple Subjects 84
7.5 Heart-Rate Detection Performance In Further Distances 87
7.6 Precise Phase Calibration Technique for Improved Heartbeat Detectability 87
7.6.1 Computer Simulation 88
7.6.2 Controlled Mechanic System 89
7.6.3 Human Subject 90
8 SUMMARY 92
REFERENCES 93
APPENDIX
A LIST OF ACRONYMS 102

LIST OF FIGURES

Figure Page

1.1 High-level processing diagram for harmonics aided heart-rate estimation method 3

2.1 Example ECG signal 6

2.2 Green LED-based pulse sensors 7

2.3 Vital sign detection using radar signal 8

3.1 (a) I and Q Data before and after DC calibration; (b) empirical convergence rate of LM algorithm 20

4.1 Harmonics-based heart rate estiamtion 28

4.2 Transmitted UWB pulse 29

4.3 Harmonics strength as a function of chest movement 31

4.4 Intermodulations strength as a function of chest movement 32

4.5 Heart rate readings from the reference systems: (a) camera based monitoring system; (b) chest strap heart-rate monitor 34

4.6 Second-order heartbeat harmonics spectrum of the two subjects measured from the radar system 34

4.7 Two heart-rates detection at equal distance 35

4.8 Small-scale motion performance example. (a) range-slow-time heatmap; (b) vital signs spectrum comparison, top plot: complex signal demodulation (CSD); middle plot: phase-based; bottom plot: 2^{nd} heartbeat harmonic; (c) heart-rate evolution comparison. Note that (b)(c) are generated using range bin 0.69 meter which contains both vital signs motion and hand motion. 37

4.9 Example when heartbeat harmonics is not visible 38

Figure Page

4.10 Heartbeart frequency & its 2nd-order harmonic present in the negative spectrum . . . 40
4.11 Potential estimation error due to spectral peak selection . . . 41
5.1 Piece-wise stationary respiration parameters. Top Plot: received signal levels relative to the nominal received signal magnitude; bottom plot: the corresponding respiration frequencies in BPM. . . . 44
5.2 Comparison of phase recovering performance. X-axis denotes time in seconds. . . . 47
5.3 Circle-fitting results for non-stationary motion. Note the above results are normalized with respect to the unit circle. . . . 47
5.4 Respiration pattern estimation . . . 49
5.5 The common direction of the finely corrected I/Q samples . . . 50
5.6 High-level processing diagram of an automated phase calibration routine 51
5.7 Graphical representation of the phase calibration routine . . . 52
6.1 Typical experimental setup . . . 53
6.2 Characteristics of the UWB signal in frequency and time domains . . . 54
6.3 Operating Principle* . . . 56
6.4 Low-Power UWB pulse* . . . 57
6.5 A signal processing diagram for camera-based heart-rate estimation . . . 58
6.6 Wavelength dependence of the AC/DC ratio γ in contact PPG signal. The ratio of the RGB lights follows $\gamma_G > \gamma_B > \gamma_R$ . . . 61
6.7 Example of standard reference devices in the experiment . . . 62
6.8 Example pulse waveforms from the standard reference devices in Fig. Figure 6.7 . . . 62

Figure Page

7.1 64
7.2 1-D spectral analysis: controlled motorized vital signs simulator. Predefined heart-rate: 58 BPM, respiration rate: 26 BPM. 65
7.3 1-D spectral analysis: stationary human subject seated 0.8 meters away. 65
7.4 Phase calibration result: simulator. 68
7.5 Phase calibration result: human subject example 1. 68
7.6 Phase calibration result: human subject example 2. 69
7.7 Irregular respiration pattern in data for generating Fig. Figure 7.6. 69
7.8 Time-frequency analysis waterfall plots from vital signs simulator. X axis denotes time scale in 40-second interval; y axis denotes frequency scale in BPM. 71
7.9 Time-frequency analysis waterfall plots from human subject 1. X axis denotes time scale in 40-second interval; y axis denotes frequency scale in breaths/beats per minute (BPM). 71
7.10 Time-frequency analysis waterfall plots from human subject 2. X axis denotes time scale in 40-second interval; y axis denotes frequency scale in BPM. 72
7.11 Continuous heart-rate monitoring performance of different algorithms. . 73
7.12 Accuracy demonstration 75
7.13 Two subject heart-rate monitoring setup 75
7.14 Two subject heart-rate monitoring: signal after static background removed 76

Figure Page

7.15 Spectra comparison of subject 1 from various systems. From the top to the bottom plots are the reference system, the camera system, and the radar system. 77
7.16 Spectra comparison of subject 2 from various systems. From the upper to the lower plots are the camera system and the radar system. 78
7.17 Heart-rate estimation accuracy demonstration of subject 1 78
7.18 Heart-rate monitoring demonstration of subject 2 79
7.19 Radar performance demonstration: proposed method vs conventional CSD method 80
7.20 Radar performance against heart-rate extracted from the reference electrocardiogram (ECG) signal 80
7.21 Radar performance compared with the camera-based system 81
7.22 Two-dimensional analysis of vital signs monitoring. Left plot: the range-slow-time heatmap of the raw data. The strong energy reflection at about 0.4 meter is from a dry wall. Middle plot: the range-slow-time heatmap after removing the static background. Right plot: the corresponding range-Doppler map. 82
7.23 High-level processing diagram for through wall vital signs monitoring .. 83
7.24 Through wall single subject monitoring performance against the CSD method 84
7.25 Raw RF signal 85
7.26 Signal after static background removed 85
7.27 Through wall heart-rate monitoring performance against the ECG reference signal 86

Figure Page

7.28 Through wall two subjects monitoring performance. (a) respiration patterns; (b) heart-rate evolutions. 86
7.29 Heartbeat detection performance at different ranges. 87
7.30 Respiration suppression performance demonstration: computer simulation. (a) Phase calibration results when constant DC-offset is applied; (b) CSD result assuming time-varying phase noise; (c) conventional phase calibration result assuming time-varying phase noise; (d) precise phase calibration result in present of time-varying phase noise. Dashed vertical lines denote the nominal respiratory rate and heart-rate. 89
7.31 Respiration suppression performance demonstration: mechanic system. (a) CSD method; (b) conventional method; (c) precise phase calibration method. Dashed vertical lines denote the pre-defined respiratory rate and heart-rate. 90
7.32 Heart-rate monitoring performance from different phase calibration methods. The upper plot and the lower plot are the extracted respiration pattern and the heart-rate evolutions from different methods. . 91

LIST OF TABLES

Table Page

4.1 Vital Signs Simulation Parameters 30

4.2 Summary of Experiment Results (Unit in BPM) 35

4.3 Adaptive HR Selection Scheme 43

6.1 Radar System Parameters 54

6.2 Imaging System Parameters 57

7.1 Summary: Performance (Unit in BPM) At Various Ranges 88

Chapter 1

INTRODUCTION

Heart disease is one of the major causes of death in the western world, so there is a need to find the abnormal changes of the heartbeat rhythm. To diagnosis arrhythmias, a doctor often chooses a complete set of ECG, usually after a life threatening event or when they suspect something is wrong. To obtain high quality ECG, the medical team will attach adhesive electrodes in strategic places around chest and abdomen to get a good recording of pulses. But what about patients or even normal people are living there regular lives? A convenient and comfortable way is needed to provide us a quick diagnosis. Or in more general case information of cardiovascular activity should be available. There are few numbers more helpful than the resting heart-rate. It is one of the most important vital signs parameters that can be used to inspect potential health issues and to change unhealthy daily routine.

By continuous monitoring the heart-rate, the changes of the resting heart-rate are checked. If there is something suspect, then one can go for doctors and get a real diagnosis. Nowadays with the advancement of technology, low-cost smart devices with heart-rate monitoring functionality enter our daily life. More people are using wearable technology like the Apple Watch or the FitBit for continuous monitoring their heart health and fitness since there is relation between the resting heart-rate and the daily habit as shown in these studies [18].

1.1 Introduction

The main goal of this thesis is to demonstrate, through realistic experiments, the possibility of using radar technology for continuous monitoring of cardiac and

respiratory activities of stationary human beings in a non-contact fashion.

1.2 Contributions

Different ways for vital signs detection using UWB impulse radar were carefully reviewed from signal processing perspective and the theory was validated experimentally. The effectiveness of the popular phase-based methods was demonstrated. The advantages and disadvantages of phase-based method were identified. A precise phase calibration routine was proposed to deal with the limitation of the existing phase-based methods.

A new heart-rate estimation algorithm based on the idea of recovering the fundamental heartbeat frequency from its higher-order spectral features was proposed and implemented. The proposed theory was demonstrated numerically and experimentally. What's more, the harmonics-based heart-rate estimation algorithm is possible for real-time processing. A high-level signal processing chain for heart-rate estimation based on its higher-order harmonics is illustrated in Fig. Figure 1.1. The competing remote technologies for vital signs monitoring: radar system and remote imaging system, such as camera-based system, were compared. The proposed method, the radar system, has similar performance as that of the camera-based system.

1.3 Background

Monitoring a patient's heartbeat and respiration is important in the medical field for many situations. The gold standard tool used for heartbeat monitoring is the voltage-derived ECG. Electrical signals cause the heart muscle to contract and expand. These signals pass through the body and can be measured by electrodes (electrical contacts) attached to the skin. Electrodes on different sides of the heart measure the activity of different parts of the heart muscles. An ECG shows the voltage be-

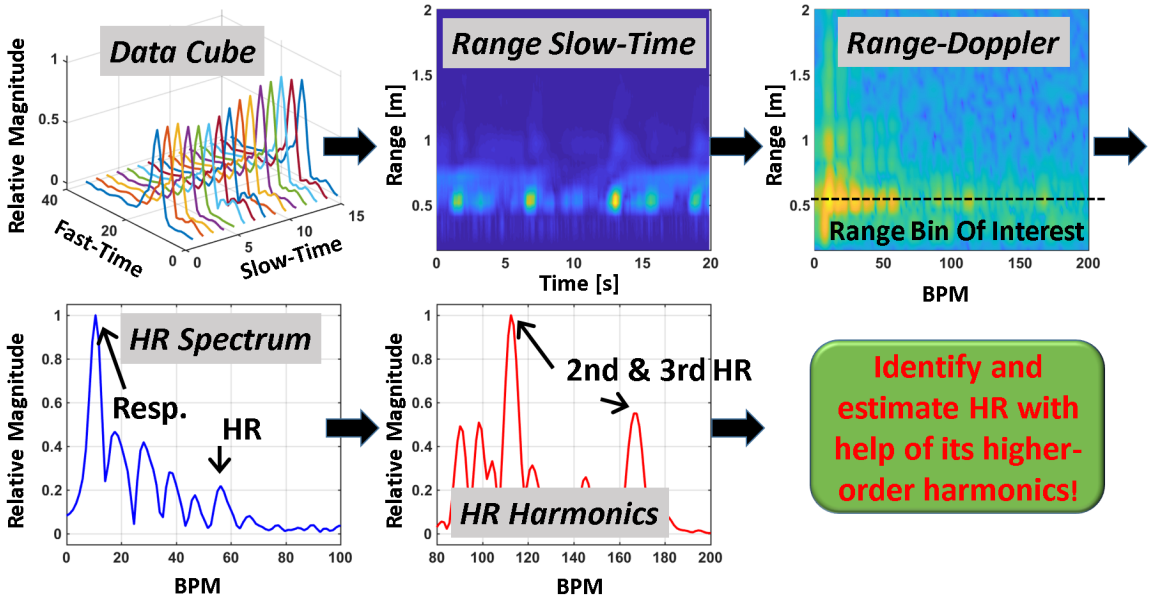


Figure 1.1: High-level processing diagram for harmonics aided heart-rate estimation method

tween pairs of these electrodes, and the muscle activity from different directions. The ECG indicates the overall rhythm of the cardiac activity. For accurate measurement, it requires placement of three to twelve electrodes on the human body. The measurement accuracy increases with the number of electrodes being applied. Another convenient way for a quick measurement is to use photoplethymography (PPG) sensors, such as pulse oximeter. A pulse oximeter measures the amount of oxygen in a patient's blood by observing light reflections. As blood vessels expand and contract with every heartbeat, the pulse oximeter signal fluctuates accordingly. The pulse oximeter probe requires direct contact with the fingertip or ear-lobe. Traditionally, the stethoscope is a simple acoustic tool commonly used by physicians. Stethoscopes can be used to listen to heartbeat sounds and breathing for a quick initial diagnosis of the potential patient. In general, these devices vary in size and have advantages on their own. However, they all require a direct physical contact to the human body. In

some situations, these devices are difficult to use on infants or skin-burned patients. In our daily life, these contact-based devices cannot be used for long-term monitoring of activities and they may cause discomfort to the users. Besides, these devices cannot be applied to multiple subjects at the same time using a single device.

More recently, contact-free sensors such as optical sensors and UWB radar sensors have been applied in healthcare applications. Similar to the contact-PPG sensor, a cam recorder/camera (optical sensor) can be used to measure the cardiovascular pulse wave (or heartbeat pulse) through variations in the transmitted or reflected light with normal ambient light as the illumination source [19–24]. The camera-based vital signs monitoring system is often referred as RIPPG sensor. The main drawbacks of remote imaging sensors are the lighting condition and privacy issue.

UWB systems have unique advantages for medical use [25]. UWB signals are capable of penetrating a great variety of materials, including plastic, wood, rubber, dry soil, glass, and concrete [26–29]. In general, systems with lower center frequencies achieve better material penetration. Biological materials including skin, muscle, fat, and bone can also be penetrated, although not as easily as most low conductivity building materials. Highly conductive materials, such as metals and seawater, cannot be penetrated. UWB imaging systems would allow a physician to monitor internal organ movements without any invasive surgical procedures [30, 31]. Unlike traditional ultrasound systems, which require direct skin contact, UWB sensors and imaging systems can operate at a standoff distance. Since UWB signals are non-ionizing, they do not cause adverse effects associated with X-ray systems such as computerized tomography (CT) scanners [32, 33]. Due to the inherent large bandwidth, UWB radar technology offers the possibility for high-resolution measurements. In combination with the low-power consumption of impulse-based systems and the low radiated power levels, UWB has potential applications in breast cancer detection [31, 34, 35] and vital

signs measurement [36–40].

Chapter 2

TECHNOLOGIES FOR VITAL SIGNS MONITORING

Monitoring patient heart-rate can be of great importance. Beat-to-beat interval, often referred as RR interval, is an instantaneous measurement of cardiac activity. It is very helpful for patient diagnosis. The standard way to measure RR interval is using ECG devices with multiple electrodes. ECG is a standard reference signal that is used for cardio health and wellness by healthcare providers. With ECG, heart-rate can be measured accurately. Heart rate variability (HRV) can be reliably derived from ECG data and RR intervals can be extracted with millisecond accuracy, so that meaningful HRV data can be obtained with short-duration measurements [41–43].

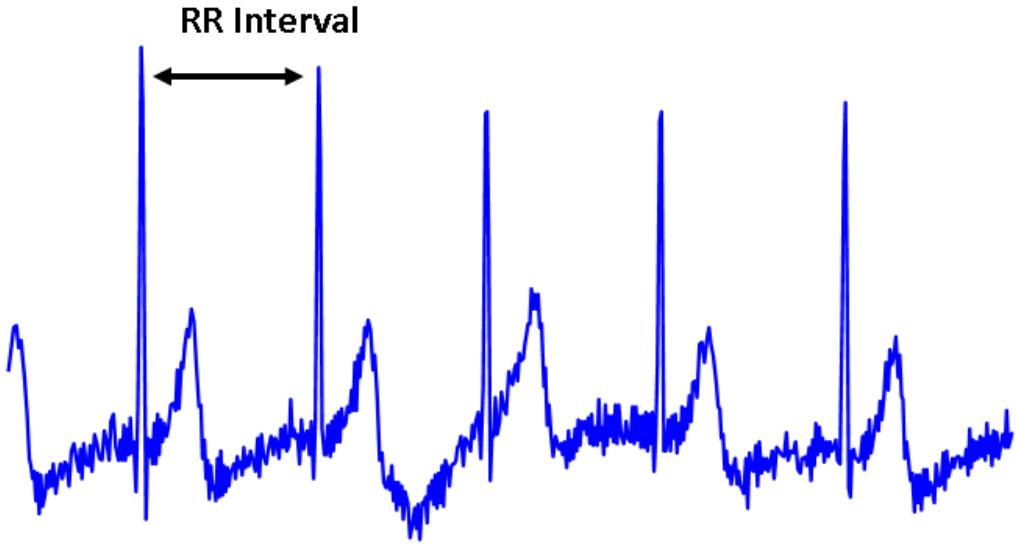


Figure 2.1: Example ECG signal



Figure 2.2: Green LED-based pulse sensors

An example of ECG waveform is shown in Fig. Figure 2.1.

PPG is an electro-optic technique for non-invasively measuring the tissue blood volume pulses in the microvascular tissue bed underneath the skin. Vital physical signs, such as the heart-rate, respiratory, and arterial oxygen saturation, can be accessed by PPG. With the rapid advancement of portable imaging devices, especially for smartphones and laptops, there is a trend for transforming conventional contact PPG to RIPPG technologies [23, 44–52]. This emerging technique has good potential as an innovative way to access cardiac pulsation, because only a low-cost digital camera is needed and contact probes or dedicated light sources are not required.

Heart-rate can be measured with PPG, however it is only suitable for average or moving average measurement. With PPG sensors, the RR interval accuracy is limited by usable sampling rate due to the high power consumption of light-emitting diodes (LEDs) in Fig. Figure 2.2.

2.1 Ultra-Wideband Sensing Technology

Different from other radar systems, UWB radar system has strong penetrating power compared to the optical system [53], and has fine range resolution compared to

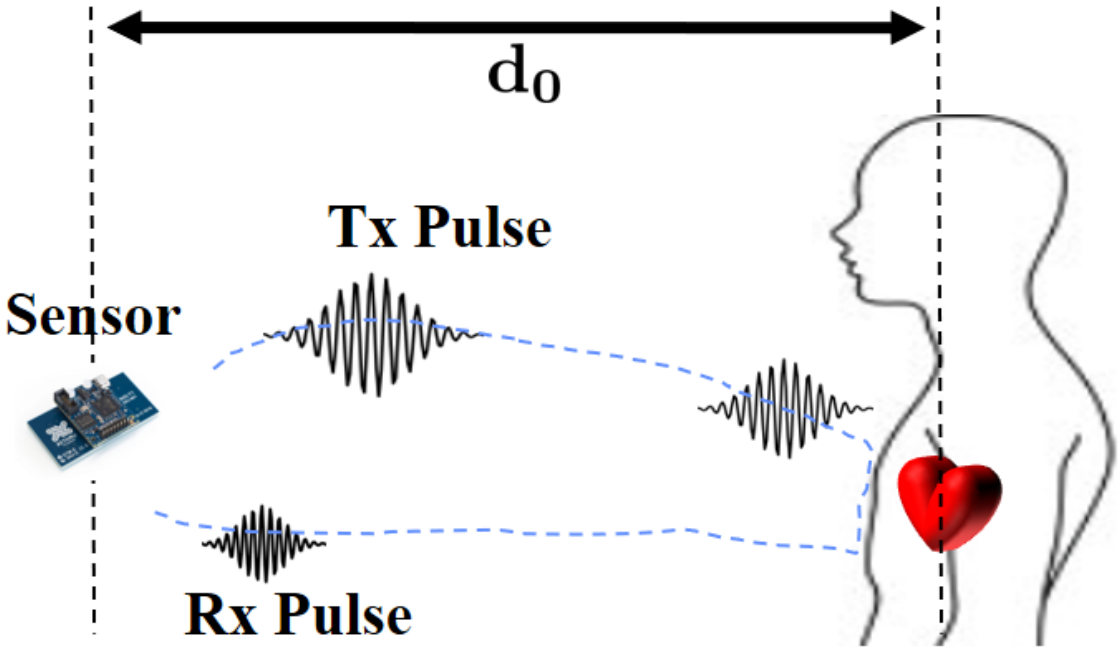


Figure 2.3: Vital sign detection using radar signal

CW radar system [54]. By using impulse or frequency modulated (FM) signal [55–58], UWB radar can not only measure the micro-Doppler motion [59–62][63], such vital signs but can also distinguish closely spaced targets [64–69].

The transmit antenna sends a train of UWB pulses towards the human subject. These pulses are reflected by the moving chest wall. The periodic expansion and contraction of the chest movement generates an observable change in the multi-path profile that is acquired by the receiving antenna, and this variation over time can be exploited for estimating the vital signs. A vital signs radar system is illustrated in Fig. Figure 2.3.

2.2 System Concept

Cardiac and respiratory monitoring can be achieved through detecting the small body motion of the target subject produced by related organs. The transmitter generates a series of short pulses. At the dielectric interfaces of the subjects, portions of the transmitted pulse are reflected back to the receiver. As the chest wall moves, the corresponding variation will be observed through the measured time-delay from the echo waveform. Based on the target properties and the radar parameters, the backscattered energy can be calculated approximately. The main reflection will occur at the air/chest interface. The propagation impedance in free space is defined as [70],

$$\begin{aligned} \eta_0 &= \sqrt{\frac{\mu_0}{\epsilon_0}} = 376.73\ \Omega \\ \mu_0 &= 4\pi \times 10^{-7}\ H/m \\ \epsilon_0 &\approx 8.8542 \times 10^{-12}\ F/m, \end{aligned} \tag{2.1}$$

where μ_0 is the permeability of a vacuum space and ϵ_0 is the permittivity of a vacuum space. By considering the relative permittivity ϵ_r, the propagation impedance η of a material can be determined,

$$\eta = \sqrt{\frac{\mu_0}{\epsilon_0 \epsilon_r}}. \tag{2.2}$$

For example, the dry skin has a relative permittivity $\epsilon_r = 33$ at a frequency of 7.3 GHz. This yields a propagation impedance of,

$$\eta_{\text{Dry Skin}} = \sqrt{\frac{\mu_0}{\epsilon_0 \epsilon_r}} \approx 65.58\ \Omega. \tag{2.3}$$

The reflection coefficient Γ is defined as,

$$\Gamma = \frac{\eta_{\text{Dry Skin}} - \eta_0}{\eta_{\text{Dry Skin}} + \eta_0} \tag{2.4}$$

which has a reflection coefficient of 70.3%, which means that about 70.3% of the energy of the electromagnetic wave at the air to dry skin interface is reflected. Therefore,

the expansion and contraction of the chest chamber creates an observable change in the multipath profile, which is exploited to determine the respiration rate. A similar analysis can be applied for the heartbeat but the backscattered energy due to cardiac activity is much weaker than that of the respiratory activity.

2.3 Previous Works

Theoretical analysis for vital signs extraction has been well-established for CW radar [71–74]. Either I channel or Q channel is selected in single channel selection method for vital signs detection. The method however suffers when the signal sensitivity is very weak in I channel or Q channel. To deal with this channel selection problem, a CSD method is proposed in reference [73]. Theoretical analysis on spectrum representation is developed demonstrating that the Fourier spectrum of the vital signs is actually a pulse train with decaying amplitudes associated with each pulse [75]. This is an important result because it states that the fundamental heartbeat frequency is closely spaced with the higher-order harmonics (usually the 3^{rd}) of the fundamental respiration frequency and often these higher-order harmonics are much stronger than the heartbeat signal strength. Due to these two facts, the long-term heart-rate monitoring using CSD is not possible. Later on, a phase-based method, called Arctangent demodulation (AD) method, is proposed in reference [72] with phase calibration techniques. Similar phase-based method and extension of AD method has been reported in reference [74].

On the other hand, possibility of vital signs extraction using UWB impulse radar has been reported in references [75–77]. However, a detailed discussion and theoretical justification on the feasibility of applying popular CSD and AD methods for UWB impulse radar is not available. Limited discussion has been carried out in reference [78]. Due to the different signaling scheme, the mathematical formulation of UWB

impulse radar for vital signs detection is somewhat different from that of the CW radar. Therefore there are more than one ways to perform vital signs detection using UWB impulse radar compared to the CW radar from a mathematical modeling perspective. In this thesis, existing methods such as CSD and AD and related methods are successfully applied for vital signs detection using UWB impulse radar.

Multiple-subject vital signs detection has been successfully demonstrated in literature. In reference [79], the Variational Mode Decomposition is used to separate and reconstruct respiration waveform from three stationary subjects at an equal distance to an UWB radar. In reference [76], the heart-rates of two subjects are separated and detected at different distances using an UWB sensor array. In reference [80], vital signs detection performance of an UWB radar system and a camera-based system is compared when two subjects are present at difference distances. Most of these works however focus on heartbeat detection performance. Vital signs of multiple-subjects are isolated in either angular-, range- or spectral-domains. Continuous monitoring performance has not been demonstrated.

Chapter 3

STATE OF THE ART: RADAR SIGNAL PROCESSING TECHNIQUES FOR VITAL SIGNS EXTRACTION

3.1 UWB Signal Model

In this section, the signal model for vital signs detection using UWB impulse radar is discussed. The results in references [75][76] are summarized and extended. The received signal is directly sampled in radio frequency (RF) and then digitally converted to the complex-baseband. The fast-time sampling interval (range) is usually on the order of nano-second and the output slow-time sampling interval is on the order of micro-second. In this model, τ denotes the fast-sampling time and ν is the transformed frequency component while t denotes the slow cross-range sample time and f is the corresponding Fourier domain component. The vital signs of a subject at a nominal distance d_0 can be modeled as a sum of two sine waves from respiratory and cardiac activities,

$$d(t) = d_0 + M_b \sin(2\pi f_b t) + M_h \sin(2\pi f_h t), \tag{3.1}$$

where M_b is the magnitude of respiratory activity, and M_h is the magnitude of cardiac activity. f_b and f_h are respiration and heartbeat frequencies. The received signal can be modeled as sum of the target response and the delayed, attenuated versions of the transmitted pulse due to static environment,

$$r(t,\tau) = A_T\, p(\tau - \tau_D(t)) + \sum_i A_i\, p(\tau - \tau_i), \tag{3.2}$$

where $p(t,\tau)$ is the generated short pulse, centered at a nominal center frequency F_c. A_T and A_i denote the amplitudes of the target response and the multi-path

components, while $\tau_D(t)$ and τ_i are the corresponding delays, $\tau_D(t) = 2\,d(t)/c$, where c is the speed of light. The signal of interest can be modeled as,

$$r_0(t,\tau) = A_T\, p(\tau - \tau_D(t)), \tag{3.3}$$

where the multi-path components due to static environment can be eliminated by mean subtraction. The received signal is then down converted to the complex-baseband and is represented as,

$$\begin{aligned} y(t,\tau) &= r_0(t,\tau)\, e^{-\mathrm{j}2\pi F_c \tau} \\ &= A_T\, p(\tau - \tau_D(t))\, e^{-\mathrm{j}2\pi F_c \tau}. \end{aligned} \tag{3.4}$$

3.2 Direct RF Method

In this section, vital signs information is shown to be extracted from the RF signal in Eqn. (Equation (3.3)) at the nominal target distance d_0. One important observation is that the same time-delay variation as a function of t due to chest movement is also preserved in Eqn. (Equation (3.3)) and thus spectrum analysis of Eqn. (Equation (3.3)) and (Equation (3.4)) should generate similar result for vital signs detection [13]. Through forward and backward Fourier transforms with respect to t and τ, the Fourier transform of Eqn. (Equation (3.4)) with respect to t is given as,

$$\begin{aligned} Y^{\mathrm{RF}}(f,\tau) = A_T \sum_{k=-\infty}^{\infty} \sum_{l=-\infty}^{\infty} \delta(f - kf_b - lf_h) \times \int_{-\infty}^{\infty} d\nu \, \Big[P(\nu)\, e^{\mathrm{j}2\pi\nu(\tau-\tau_0)} \\ \times J_k\big(4\pi\nu \frac{M_b}{c}\big)\; J_l\big(4\pi\nu \frac{M_h}{c}\big) \Big] \end{aligned} \tag{3.5}$$

$$= A_T \sum_{k=-\infty}^{\infty} \sum_{l=-\infty}^{\infty} C_{k,l}^{\mathrm{RF}}(\tau)\delta(f - kf_b - lf_h), \tag{3.6}$$

$$\big|Y^{\mathrm{RF}}(f,\tau)\big| \le |A_T| \sum_{k=-\infty}^{\infty} \sum_{l=-\infty}^{\infty} \big|C_{k,l}^{\mathrm{RF}}(\tau_0)\big|\delta(f - kf_b - lf_h) = \big|Y^{\mathrm{RF}}(f,\tau_0)\big|, \tag{3.7}$$

where $P(\nu)$ denotes the Fourier transform of the transmitted pulse $p(\tau)$ and $J_k(.)$ denotes the Bessel function of the first kind [81, 82]. $C_{k,l}^{\mathrm{RF}}(\tau)$ is given as the following equation and its absolute value achieves the maximum at τ_0.

$$C_{k,l}^{\mathrm{RF}}(\tau) = \int_{-\infty}^{\infty} d\nu \Big[P(\nu) e^{\mathrm{j}2\pi\nu(\tau-\tau_0)} J_k\big(4\pi\nu\frac{M_b}{c}\big) J_l\big(4\pi\nu\frac{M_h}{c}\big) \Big] \tag{3.8}$$

3.3 I/Q Channels-Based Methods

In this section, CSD method for vital signs detection is applied to the complex-baseband signal Eqn. (Equation (3.4)) in two different domains. First, CSD method can be performed directly onto Eqn. (Equation (3.4)). Again by two-dimensional (2-D) Fourier transform, the final expression for the Fourier transform of the complex-baseband signal in slow-time is derived,

$$Y^{\mathrm{B}}(f,\tau) = A_T\, e^{-\mathrm{j}2\pi F_c\tau_0} \sum_{k=-\infty}^{\infty} \sum_{l=-\infty}^{\infty} C_{k,l}^{\mathrm{B}}(\tau)\delta(f - kf_b - lf_h), \tag{3.9}$$

$$|Y^{\mathrm{B}}(f,\tau)| \leq |A_T| \sum_{k=-\infty}^{\infty} \sum_{l=-\infty}^{\infty} |C_{k,l}^{\mathrm{B}}(\tau_0)|\ \delta(f - kf_b - lf_h) = |Y(f,\tau_0)|, \tag{3.10}$$

where $C_{k,l}^{\mathrm{B}}(\tau) = \int d\nu\ \big[P(\nu+F_c)\ e^{\mathrm{j}2\pi\nu(\tau-\tau_0)} J_k\big(4\pi(\nu+F_c)M_b/c\big)\ J_l\big(4\pi(\nu+F_c)M_h/c\big)\big]$ and $|C_{k,l}^{\mathrm{B}}|$ achieves the maximum $C_{k,l}(\tau_0)$ at τ_0. $P(\nu+F_c)$ is the fast-time Fourier transform of the transmitted pulse shifted to DC (zero frequency position in spectrum).

As for the second approach for applying CSD method, the fast-time (ν) Fourier transform is applied to Eqn. (Equation (3.4)) to separate out the time-delay in $p(\tau - \tau_D(t))$,

$$Y^{\mathrm{B}}(t,\nu) = A_T P(\nu+F_c) e^{-\mathrm{j}2\pi(\nu+F_c)\tau_D(t)}. \tag{3.11}$$

In order to evaluate the above equation, one can set $\nu = 0$ corresponding to the

fast-time Fourier transform evaluated at DC as suggested in reference [76] and thus,

$$Y^{\mathrm{B}}(t,0) = A_T P(F_c) e^{-\mathrm{j}2\pi F_c \tau_D(t)}. \tag{3.12}$$

Invoking Jacobi-Angle expansion $e^{-\mathrm{j}z\sin(2\pi f_0 t)} = \sum_{m=-\infty}^{\infty} J_m(z) e^{-\mathrm{j}2\pi m f_0 t}$ to Eqn. (Equation (3.12)),

$$Y^{\mathrm{B}}(t,0) = A_T P(F_c)\ e^{-\mathrm{j}\frac{4\pi M_b}{c}\sin(2\pi f_b t)}\ e^{-\mathrm{j}\frac{4\pi M_h}{c}\sin(2\pi f_h t)} \tag{3.13}$$

$$= A_T P(F_c) \sum_{k=-\infty}^{\infty} \sum_{l=-\infty}^{\infty} J_k\big(\frac{4\pi M_b}{c}\big) J_l\big(\frac{4\pi M_h}{c}\big) e^{-\mathrm{j}2\pi k f_b t} e^{-\mathrm{j}2\pi l f_h t}. \tag{3.14}$$

Then the final expression is obtained by applying the slow-time Fourier transform to Eqn. (Equation (3.14)),

$$Y^{\mathrm{B}}(f,0) = A_T P(F_c) \sum_{k=-\infty}^{\infty} \sum_{l=-\infty}^{\infty} J_k\big(\frac{4\pi M_b}{c}\big) J_l\big(\frac{4\pi M_h}{c}\big) \delta(f - k f_b - l f_h). \tag{3.15}$$

3.4 Phase-Based Methods

In this section, phase-based methods that are able to extract phase variation due to vital signs activity are described. The main advantage of phase-based approach is the ability to suppress respiration harmonics as shown in the pulse train in Eqn. (Equation (3.15)) since the phase information in the exponential term as in Eqn. (Equation (3.11)) is linearly related to the chest movement. In order to correctly extract the phase information, a phase calibration process is required to correct a residual phase accumulated in the circuit and along the transmission path. The phase calibration techniques are discussed in in Section Section 3.4.4. By comparing Eqn. (Equation (3.3)), (Equation (3.4)) and (Equation (3.12)), it should be clear now that clean phase information can be only obtained through Eqn. (Equation (3.12)). For convenience, Eqn. (Equation (3.12)) is re-written as,

$$\begin{aligned} Y^{\mathrm{B}}(t,0) &= A_T P(t, F_c) e^{-\mathrm{j}2\pi F_c \tau_D(t)} \\ &= A_T \Big(\int_{-\infty}^{\infty} d\tau\ p(t,\tau) e^{-\mathrm{j}2\pi F_c \tau} \Big)\ e^{-\mathrm{j}2\pi F_c \tau_D(t)}, \end{aligned} \tag{3.16}$$

where $P(t, F_c)$ is a constant complex value. A common pulse is transmitted repeatedly and thus the transmitted pulse $p(t, \tau)$ is constant over the slow-time. $P(t, F_c)$ can be then decomposed as $M_P\ e^{-\mathrm{j}\phi_P}$ with amplitude M_P and phase ϕ_P,

$$Y^{\mathrm{B}}(t, 0) = A_T\, M_P\ e^{-\mathrm{j}\left(2\pi F_c \tau_D(t) + \phi_P\right)}. \tag{3.17}$$

Note that A_T and M_P are real scalars and the vital information is conserved in the phase term above. I and Q channels can be represented as,

$$I(t) = A_T\, M_P\ \cos(2\pi F_c \tau_D(t) + \phi_P) \tag{3.18}$$

$$Q(t) = A_T\, M_P\ \sin(2\pi F_c \tau_D(t) + \phi_P). \tag{3.19}$$

3.4.1 Arctangent Demodulation Method

One way to reliably detect vital information in quadrature demodulation system is to use AD method. By directly calculating the phase variation as Arctangent function of $Q(t)/I(t)$, accurate phase information extraction is possible. The phase variation is linearly related to the vital information as follows,

$$\begin{aligned}
\Phi(t) &= \text{unwrapping}\left\{\text{atan}\left(\frac{Q(t)}{I(t)}\right)\right\} \\
&= \frac{4\pi M_b\ \sin(2\pi f_b t)}{\lambda} + \frac{4\pi M_h\ \sin(2\pi f_h t)}{\lambda} + \frac{4\pi d_0}{c} + \phi_P \\
&= \frac{4\pi M_b\ \sin(2\pi f_b t)}{\lambda} + \frac{4\pi M_h\ \sin(2\pi f_h t)}{\lambda} + \phi_{\mathrm{DC}},
\end{aligned} \tag{3.20}$$

where atan denotes Arctangent function, $\lambda = F_c/c$ is the wavelength and $\phi_{\mathrm{DC}} = 4\pi d_0/c + \phi_P$ denotes the total DC information including two phase terms: the first term $4\pi d_0/c$ is determined by the target position information and the second term is determined by the pulse waveform and the center frequency. Often a phase unwrapping function is needed to deal with the phase discontinuity outside of $[-\pi/2, \pi/2]$ due to Arctangent operation. The result in Eqn. (Equation (3.20)) is the ideal situation. In general, phase noise is inevitable and independently present in I/Q channels as ε_I

and ε_Q because of the hardware imperfection such as antenna mismatch, sampling jitter. The overall vital signal is represented as $V(t) = M_b \sin(2\pi f_b t) + M_h \sin(2\pi f_h t)$. The complete signal model that captures this I/Q imbalance effect is given as follows,

$$\begin{aligned}\dot{\Phi}(t) &= \text{unwrapping}\left\{\text{atan}\left(\frac{\dot{Q}(t)}{\dot{I}(t)}\right)\right\} \\ &= \text{unwrapping}\left\{\text{atan}\left(\frac{A_Q\ \sin(4\pi V(t)/\lambda + \varphi_Q) + \mathcal{D}_Q}{A_I\ \cos(4\pi V(t)/\lambda + \varphi_I) + \mathcal{D}_I}\right)\right\},\end{aligned} \tag{3.21}$$

where A_i, φ_i and $\mathcal{D}_i$, $i = I$ or Q, represent amplitude imbalance, phase imbalance and DC-offset. The total residual phase in I/Q channels contain two parts: DC and phase noise, $\mathcal{D}_I = \phi_{\text{DC}} + \varepsilon_I$ and $\mathcal{D}_Q = \phi_{\text{DC}} + \varepsilon_Q$. Here the raw radar data is directly RF sampled and the down-conversion is done in digital signal processing (DSP). Therefore there are no amplitude imbalance $A_I = A_Q = A_0$ and phase imbalance $\varphi_I = \varphi_Q = \varphi_0$. Only DC-offsets in I/Q channels need to be compensated. If perfect correction is done, Eqn. (Equation (3.21)) is reduced to,

$$\begin{aligned}\dot{\Phi}(t) &= \text{unwrapping}\left\{\text{atan}\left(\frac{A_0\ \sin(4\pi V(t)/\lambda + \varphi_0)}{A_0\ \cos(4\pi V(t)/\lambda + \varphi_0)}\right)\right\} \\ &= \frac{4\pi V(t)}{\lambda} + \varphi_0 \\ &= \frac{4\pi M_b\ \sin(2\pi f_b t)}{\lambda} + \frac{4\pi M_h\ \sin(2\pi f_h t)}{\lambda} + \varphi_0.\end{aligned} \tag{3.22}$$

Now the Fourier transform can be directly applied to the extracted phase information in Eqn. (Equation (3.22)). Two peaks in the spectrum domain correspond to the respiratory frequency and the heartbeat frequency. Since φ_0 has no effect on the vital signs detection performance, it can be safely ignored.

3.4.2 Logarithm Method

Besides AD method, Logarithmic method (Log) [77] is a similar approach to extract the phase variation that directly related to the physiological motion. The Log-

arithmic operation is performed on Eqn. (Equation (3.17)),

$$\begin{aligned}\Theta(t) &= \text{unwrapping}\left\{\log_e\Big(\frac{Q(t)}{I(t)}\Big)\right\} \\ &= -\text{j}\big(2\pi\ F_c\ \tau_D(t) + \phi_P\big) + \log_e(A_T\, M_P)\end{aligned} \tag{3.23}$$

$$\longrightarrow \Phi(t) = 2\pi\ F_c\ \tau_D(t) + \text{Const.} \tag{3.24}$$

Eqn. (Equation (3.24)) is obtained by multiplying j to both side of Eqn. (Equation (3.23)) and grouping the rest terms into a constant term. But phase unwrapping and phase calibration are still needed to correctly recover the phase information.

3.4.3 Differentiate and Cross-Multiply (DACM) Method

Alternatively, an extended differentiate and cross-multiply (DACM) method [74] can be used for vital signs detection. This method consists of two operations: differentiation and integration. The differentiator is represented as follows,

$$\Phi_{\text{Diff}}(t) = \frac{d\Phi(t)}{dt} = \frac{d}{dt}\Big\{\text{atan}\Big(\frac{Q(t)}{I(t)}\Big)\Big\} \tag{3.25}$$

$$= \frac{I(t)\,\big(\frac{d}{dt}Q(t)\big) - \big(\frac{d}{dt}I(t)\big)\,Q(t)}{I^2(t) + Q^2(t)}. \tag{3.26}$$

For convenience, the integrator is represented in discrete sample version in digital domain,

$$\Phi[n] = \sum_{k=2}^{n} \frac{I[k]\ \big(Q[k] - Q[k-1]\big) - \big(I[k] - I[k-1]\big)\ Q[k]}{I^2[k] + Q^2[k]}. \tag{3.27}$$

Due to the differentiation and integration, the phase unwrapping is not required in DACM but phase calibration is required before applying extended DACM method. Extended DACM can be treated as an alternative to other phase-based methods: AD and Log methods, since it only uses a different phase unwrapping method. The goal of phase-based method is to suppress inferencing harmonics, which is determined by the phase calibration process. Extended DACM is thus not an improvement over

other existing methods. On the contrary, this method may introduce additional high frequency noise due to the differentiation and integration operations, which is an undesirable result especially for heartbeat detection.

3.4.4 Phase Calibration Technique

A key process common to all phase-based approaches is phase calibration, which determines the heartbeat detection performance. For our case, the signal model in Eqn. (Equation (3.22)) is adopted and only DC-offsets in the I/Q channels need to be compensated. This calibration process is often referred as circle-fitting [83] or center tracking [84]. Note that if RF to baseband conversion is done in hardware, in which there are two independent I/Q receiver chains, the model in Eqn. (Equation (3.21)) should be considered and the corresponding phase calibration procedure is an elliptical-fitting problem [85].

An iterative least square fit algorithm, called Levenberg-Marquardt (LM) method [83], is considered. It can effectively solve the least square problem with following form, given n data points $(I(i), Q(i))$, $1 \leq i \leq n$,

$$\mathcal{F} = \sum_{i=1}^{n} \left(\sqrt{(I(i) - \mathcal{D}_I)^2 + (Q(i) - \mathcal{D}_Q)^2} - \mathcal{R} \right)^2 \tag{3.28}$$

$$= \sum_{i=1}^{n} d_i^2, \tag{3.29}$$

where $\mathcal{F}$ denotes the objective function. The geometric fit tries to minimize the mean square distance from the fitting circle to the distorted data points and produces a tuple of $(\mathcal{D}_I, \mathcal{D}_Q, \mathcal{R})$, where $\mathcal{D}_I$,$\mathcal{D}_Q$ are the center points and $\mathcal{R}$ is the radius of the fitting circle,

$$\mathcal{R}^2 = (I(i) - \mathcal{D}_I)^2 + (I(i) - \mathcal{D}_Q)^2. \tag{3.30}$$

The efficiency and accuracy of LM circle fitting method has been reported in many papers. A theoretical analysis of LM method is presented in reference [83]. A com-

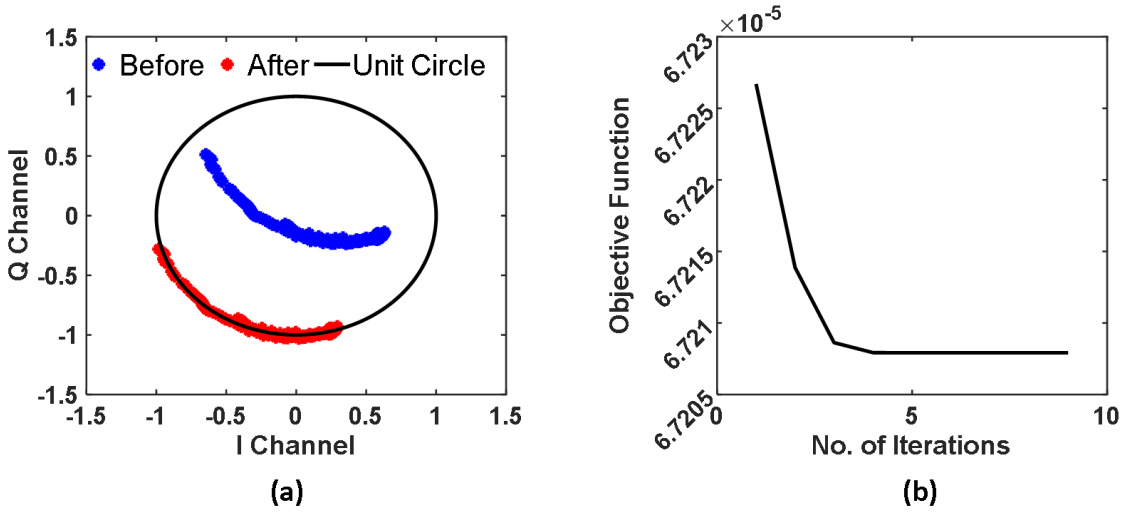


Figure 3.1: (a) I and Q Data before and after DC calibration; (b) empirical convergence rate of LM algorithm

parative study of DC-offset calibration algorithms using Doppler radar is presented in reference [86] and their result shows that the LM is one of the most accurate circle-fitting algorithms. A representative experimental example is illustrated in Fig. Figure 3.1. The DC corrected I/Q data samples are shown in Fig. Figure 3.1(a) and an empirical convergence rate of LM method is shown in Fig. Figure 3.1(b).

3.5 Subspace-Based Methods

In this section, two subspace-based methods for vital signs detection are presented: the State-Space method (SSM) [78] and the well-known Multiple-Signal Classification (MUSIC) algorithm [87, 88]. Both methods can provide improved detection performance but they are much more computational expensive than previous methods. SSM and MUSIC can be applied to RF signal, complex-baseband signal or phase information. Here phase information is used in conjunction with SSM and MUSIC.

3.5.1 State-Space Method

The formulation of SSM for spectral estimation follows references [89, 90]. The key steps of applying SSM to phase variation are reviewed here. Similar procedure is applicable for SSM with the RF signal or the complex-baseband signal.

A state space model of the received signal is defined in the time domain as,

$$\Theta(k) = \sum_{i=1}^{M} a_i z_i^k + w(k), \;\; k = 0, 1, ..., N_s - 1, \tag{3.31}$$

$$a_i = A_i e^{\mathrm{j}\phi_i}, \tag{3.32}$$

$$z_i = e^{-k(\alpha_i + \mathrm{j}2\pi f_i)}, \tag{3.33}$$

where the output sequence Θ comprises N_s time domain samples uniformly spaced at an interval Δt, each representing a sum of M complex exponentials with amplitude A_i, phase ϕ_i, and damping factor a_i. The input to the system is represented by the time sequences $w(k)$, and f_i denotes the frequency of the i-th mode. It can be shown that z_i can be derived from the discrete state update equations [91]. Suppose that N_s discrete phase sample values are demodulated with AD method, such that $\Theta(k), k = 0, 1, ..., N_s - 1$. The state equations are defined as,

$$\mathbf{x}(k+1) = \mathbf{A}\mathbf{x}(k) + \mathbf{B}u(k) \tag{3.34}$$

$$\Theta(k) = \mathbf{C}\mathbf{x}(k) + u(k), \tag{3.35}$$

where $u(k)$ and $\Theta(k)$ are the input and output, respectively. $\mathbf{x}(k) \in \mathcal{C}^{M\times 1}$ is the state vector, $\mathbf{A} \in \mathcal{C}^{M\times M}$ is the state transition matrix, while $\mathbf{B} \in \mathcal{C}^{M\times 1}$ and $\mathbf{C} \in \mathcal{C}^{1\times M}$ are constant matrices. By taking z-transform, the transfer function $H(z)$ is obtained,

$$T(z) = \mathbf{C}(z\mathbf{I} - \mathbf{A})^{-1}\mathbf{B}, \tag{3.36}$$

where $\mathbf{I}$ is an identity matrix. The poles and zeros of $T(z)$ are eigenvalues of $\mathbf{A}$ and $(\mathbf{A} - \mathbf{BC})$, respectively. As a result, the relation between the impulse response of the

model and the state-space parameters is,

$$\Theta(k) = \mathbf{C}\mathbf{A}^{k-1}\mathbf{B}. \tag{3.37}$$

The objective is to estimate the state matrices, $\mathbf{A}, \mathbf{B}$ and $\mathbf{C}$. The process involves forming a Hankel matrix from the data samples and computing its singuar-value decomposition (SVD). The Hankel matrix is give by [92],

$$\mathbf{H} = \begin{bmatrix} \Theta(1) & \Theta(2) & ... & \Theta(L) \\ \Theta(2) & \Theta(3) & ... & \Theta(L+1) \\ \vdots & \vdots & \vdots & \vdots \\ \Theta(N-L+1) & \Theta(N-L+2) & ... & \Theta(N) \end{bmatrix}, \tag{3.38}$$

where the parameter L denotes the length of the correlation window, and is heuristically chosen to be the smallest integer less than or equal to $N/2$. Subspace decomposition methods exploit the eigenstructure of Hankel matrices to estimate the parameters of linear time-invariant signal models. Accordingly, the M-rank reduction is obtained by applying the low-rank truncation to the SVD of $\mathbf{H}$,

$$\tilde{\mathbf{H}} = \mathbf{U}_{\text{sig}}\Sigma_{\text{Sig}}\mathbf{V}_{\text{sig}}^{\dagger}, \tag{3.39}$$

where $\mathbf{U}_{\text{sig}}$ and $\mathbf{V}_{\text{sig}}$ denote the noise-corrupted signal components of the left and right unitary matrices $\mathbf{U}$ and $\mathbf{V}$. $\mathbf{\Sigma}$ is a diagonal matrix with the singular values as its diagonal entries, and † denotes complex conjugate operator. By truncating the Hankel matrix, small singular values can be discarded based on some pre-defined threshold in order to increase the accuracy of state-space identification. However this threshold is generally not known. The model order of the signal subspace can be estimated by applying the information criteria [93–95] to the sorted singular values. By using the balanced coordinate transformation, the low-rank truncation of the Hankel matrix is

factorized as,

$$\tilde{\mathbf{H}} = \mathbf{\Omega}\Gamma \tag{3.40}$$

$$\mathbf{\Omega} = \mathbf{U}_{\text{sig}}\mathbf{\Sigma}_{\text{sig}}^{\frac{1}{2}} \tag{3.41}$$

$$\mathbf{\Gamma} = \mathbf{\Sigma}_{\text{sig}}^{\frac{1}{2}}\mathbf{U}_{\text{sig}}^{\dagger}, \tag{3.42}$$

where $\mathbf{\Omega}$ and $\mathbf{\Gamma}$ denote the observability and controllability matrices, respectively. The matrix $\mathbf{A}$ can be obtained either from $\mathbf{\Omega}$ or $\mathbf{\Gamma}$ as,

$$\mathbf{A} = \left(\mathbf{\Omega}_2^{\dagger}\mathbf{\Omega}_2\right)^{-1}\mathbf{\Omega}_2^{\dagger}\mathbf{\Omega}_1, \tag{3.43}$$

where matrices $\mathbf{\Omega}_1$ and $\mathbf{\Omega}_2$ are obtained by deleting the first and the last rows of matrix $\mathbf{\Omega}$. The intermediate matrix $\mathbf{C}$ is acquired from the first row of the observability matrix,

$$\mathbf{C} = \mathbf{\Omega}(1,:). \tag{3.44}$$

The other state-independent matrix $\mathbf{B}$ is computed as,

$$\mathbf{B} = \left(\mathbf{\Upsilon}^{\dagger}\mathbf{\Upsilon}\right)^{-1}\mathbf{\Upsilon}^{\dagger}\boldsymbol{\Theta}^{T} \tag{3.45}$$

$$\mathbf{\Upsilon} = \begin{bmatrix} \mathbf{C} \\ \mathbf{CA} \\ \vdots \\ \mathbf{CA}^{N_s-1} \end{bmatrix}, \tag{3.46}$$

where T denotes transpose operation. The phase information in $\Theta(k)$ can be approximated in terms of state-space parameters $\mathbf{A}$, $\mathbf{B}$ and $\mathbf{C}$ as in Eqn. (Equation (3.37)). Fourier-based spectral analysis can be applied to the state-space representation of the phase variation. SSM is capable of parametrically characterizing the spectral peaks of heartbeat and respiration frequencies, such that the magnitude and frequency at each peak are identified with the eigenvalues of the state matrix $\mathbf{A}$. The eigenvalues

of the state matrix $\mathbf{A}$,

$$\lambda_1, ..., \ \lambda_M, \tag{3.47}$$

corresponding to the state-space poles z_i in Eqn. (Equation (3.31)) and (Equation (3.36)), yield the damping factors α_i and the frequencies f_i,

$$\alpha_i = \frac{\log|\lambda_i|}{\Delta t} \tag{3.48}$$

$$f_i = \frac{\text{angle}(\lambda_i)}{2\pi\Delta t}, \tag{3.49}$$

where angle(.) denotes phase angle operation.

3.5.2 Multiple-Signal Classification Algorithm

MUSIC algorithm has been widely applied for spectral estimation and direction finding problems [87, 88, 96]. MUSIC algorithm is implemented and compared with other methods for vital signs detection. The main advantage of MUSIC algorithm is the superior fine resolution at the cost of increased computation load. Similar to SSM, MUSIC algorithm is formulated in conjunction with AD method, in which the extracted phase variation is used as input to MUSIC algorithm. Note that the RF signal or the complex-baseband signal formats can be used. The model is constituted of M sinusoids, corrupted by noise,

$$\mathbf{x} = \sum_{m=1}^{M} \beta_m \mathbf{s}(f_m) + \mathbf{w}, \tag{3.50}$$

where $\mathbf{s}(f)$ represents the pseudo-steering vector of the signal component whose frequency f needs to be estimated. The noise vector $\mathbf{w}$ is zero-mean Gaussian with covariance $\sigma^2\mathbf{I}$. The vectors $\mathbf{x}$, $\mathbf{s}$ and $\mathbf{w}$ have dimension $N_s \times 1$. The steering vector $\mathbf{s}$ has following form,

$$\begin{aligned} \mathbf{s}(f) &= e^{-\text{j}2\pi(0:L-1)^T \ \Delta t f} \\ &= e^{-\text{j}(0:L-1)^T \ \frac{f}{F_s}}, \end{aligned} \tag{3.51}$$

where L denotes the number of temporal delays (in the unit of temporal samples) and Δt, F_s denote the sampling interval and the sampling rate. The sample correlation matrix $\mathbf{R}$ is computed as,

$$\mathbf{R} = \frac{1}{N_s - L + 1}\mathbf{Z}\mathbf{Z}^{\dagger} \tag{3.52}$$

$$\mathbf{Z} = \begin{bmatrix} x(1) & x(2) & ... & x(N_s - L + 1) \\ x(2) & x(3) & ... & x(N_s - L + 2) \\ \vdots & \vdots & \vdots & \vdots \\ x(L) & x(L+1) & ... & x(N_s) \end{bmatrix}, \tag{3.53}$$

where matrix $\mathbf{Z}$ is constructed by stacking the time-delayed version of $\mathbf{x}$ in each rows. Next step is similar to SSM, eigenvalue decomposition is applied to the correlation matrix $\mathbf{R}$ and signal subspace is determined based on some pre-defined threshold or estimated using Akaike's information criterion (AIC) and Minimum Description Length (MDL) [93, 94, 97].

$$\mathbf{R} = \mathbf{U}_{\text{sig}}\mathbf{\Sigma}_{\text{sig}}\mathrm{U}_{\text{sig}}^{\dagger} + \mathbf{U}_{\text{w}}\mathbf{\Sigma}_{\text{w}}\mathbf{U}_{\text{w}}^{\dagger} \tag{3.54}$$

$$\mathbf{Q}_{\text{w}} = \mathbf{U}_{\text{w}}\mathbf{U}_{\text{w}}^{\dagger}, \tag{3.55}$$

where $\mathbf{U}_{\text{sig}}$ and $\mathbf{\Sigma}_{\text{sig}}$ are eigenvector matrix and eigenvalue matrix for the signal subspace, $\mathbf{U}_{\text{w}}$ and $\mathbf{\Sigma}_{\text{w}}$ are eigenvector matrix and eigenvalue matrix for the noise subspace. $\mathbf{Q}_{\text{w}}$ denotes the noise subspace. Based on the orthogonality of the signal and noise subspaces, $\mathbf{U}_{\text{sig}}$ and $\mathbf{U}_{\text{w}}$, or equivalently $\mathbf{s}(f)$ and $\mathbf{U}_{\text{w}}$, the pseudo MUSIC spectrum can be computed as,

$$\begin{aligned} P_{\text{MUSIC}}(f) &= \frac{1}{\mathbf{s}^{\dagger}(f)\mathbf{Q}_{\text{w}}\mathbf{Q}_{\text{w}}^{\dagger}\mathbf{s}(f)} \\ &= \frac{1}{\mathbf{s}^{\dagger}(f)\mathbf{U}_{\text{w}}\mathbf{U}_{\text{w}}^{\dagger}\mathbf{s}(f)}. \end{aligned} \tag{3.56}$$

Therefore, the dominant spectral peaks are identified as respiration and heartbeat frequencies.

3.6 Our Approach

Popular methods such as CSD and AD cannot provide robust heart-rate estimates over time. Robust heart-rate monitoring methods are proposed in Chapter Chapter 4 based on a novel result: spectrally the fundamental heartbeat frequency is respiration-interference-limited while its higher-order harmonics are noise-limited. The higher-order statistics related to heartbeat can be a robust indication when the fundamental heartbeat is masked by the strong lower-order harmonics of respiration or when phase calibration is not accurate if phase-based method is used. In order to reveal the weak heartbeat signal and its higher-order harmonics, the received pulses are coherently combined to achieve sufficient processing gain. Analytical spectral analysis is performed to validate that the higher-order harmonics of heartbeat is almost respiration-interference free. Extensive experiments have been conducted to justify an adaptive heart-rate monitoring algorithm.

State of the art methods are fundamentally related to process the phase variation due to vital signs motions. Their performance are determined by a phase calibration procedure. Existing methods fail to consider the time-varying nature of phase noise. There is no prior knowledge about which of the corrupted I/Q samples need to corrected. A precise phase calibration routine is proposed based on the respiration pattern. The I/Q samples from every breath are more likely to experience similar motion noise and therefore they should be corrected independently. High slow-time sampling rate is used to ensure phase calibration accuracy. Occasionally, a 180-degree phase shift error occurs after the initial calibration step and should be corrected as well. All phase trajectories in the I/Q plot are only allowed in certain angular spaces. This precise phase calibration routine is presented in Chapter Chapter 5.

Chapter 4

ROBUST HEART-RATE MONITORING METHODS

Popular signal processing techniques rely on processing the complex-baseband signal and exploiting spectral isolation in order to estimate heartbeat spectral peak but it is not possible without suppressing the nearby respiration harmonics. On the other hand, methods exploit the fact that the extracted phase variation is directly related to vital signs and therefore they generate a relatively clean spectrum. But a judicious phase calibration step is required otherwise distortion can be introduced to the vital signs spectrum. The goal of this Chapter is to provide a robust heart-rate estimation method suitable for continuously monitoring.

4.1 Harmonics-Based Heartbeat Detection

In this section, an effective heart-rate detection algorithm based on recovering the fundamental heartbeat frequency from its 2^{nd}-order harmonics is proposed. The key idea is illustrated in Fig. Figure 4.1. A numerical justification of the proposed method is provided in next section.

Based on the Doppler energy presented in frequency domain, the range bin of interest is chosen. Spectral analysis is then performed to locate the dominant spectral peak, which corresponds to the respiration frequency. Next, an bandpass filter is applied to emphasize the 2^{nd}-order harmonics of heartbeat spectrum with negligible respiration-inference.

Once the 2^{nd}-order harmonics of heartbeat frequency $f_{2\text{nd}}$ is identified, the fundamental heartbeat frequency, or heart rate, can be recovered accordingly, $f_h = f_{2\text{nd}}/2$.

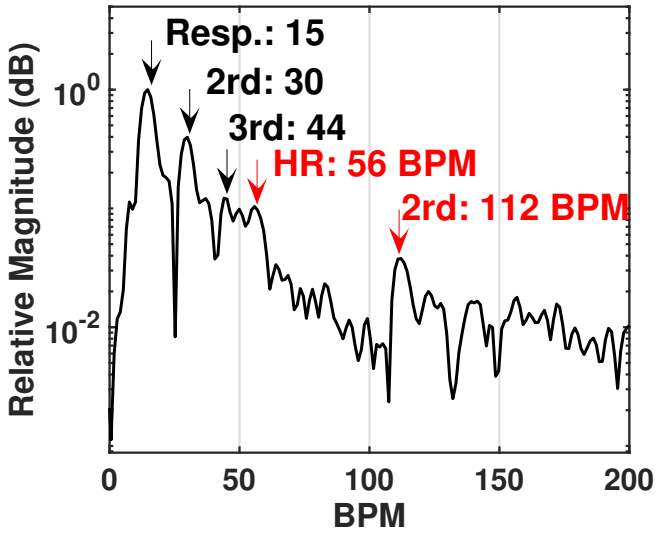


Figure 4.1: Harmonics-based heart rate estiamtion

4.2 Advantages: Free of Respiration Harmonics

Phased-based methods AD and its variations have been proposed to suppress respiration harmonics and intermodulations. Theoretically, these algorithms can successfully eliminate the respiration harmonics and intermodulations. Their performance, however, are not guaranteed as demonstrated in reference [74] since the required phase calibration can never be perfect in real system.

Instead of separating fundamental heartbeat frequency from the strong respiration harmonics and related intermodulations in the relatively low frequency domain, the proposed method focuses in the relatively higher frequency region and tries to locate the 2^{nd}-order harmonics of the fundamental heartbeat frequency. In this way, the fundamental heartbeat frequency can be easily recovered. At this frequency region, the 2^{nd}-order harmonic of heartbeat competes with higher-order harmonics of respiration, e.g., 8^{th} respiration harmonics, or higher-order harmonics of intermodulations. As the order number increases, the harmonic strength decreases dramatically. The 2^{nd}-order

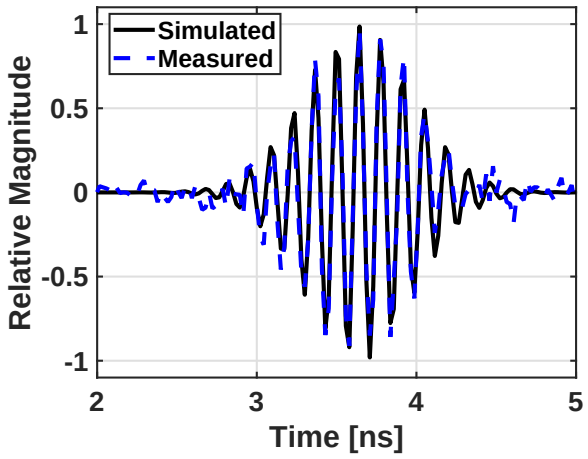


Figure 4.2: Transmitted UWB pulse

harmonic of heartbeat thus can be easily identified as if there is no interference from the respiration harmonics.

To further validate the theory, a quantitative analysis of the harmonics strength in the spectrum domain is provided based on the complex-baseband signal model in Eqn. (Equation (3.10)). Ignoring the common terms, the relative strength of each frequency harmonics in $\delta(f - kf_b - lf_h)$ is determined by $|C^{\mathrm{B}}_{k,l}(\tau_0)|$. A coarse representation of the harmonics strength of interest can be carried out based on $C^{\mathrm{B}}_{k,l}(\tau_0)$ in Eqn. (Equation (3.10)).

$$C^{\mathrm{B}}_{k,l}(\tau_0) = \int_{-BW/2}^{BW/2} d\nu \; P(\nu + F_c) J_k\Big(\frac{4\pi(\nu + F_c)M_b}{c}\Big) \; J_l\Big(\frac{4\pi(\nu + F_c)M_h}{c}\Big) \tag{4.1}$$

$$= \int_{-BW/2+F_c}^{BW/2+F_c} d\nu \; P(\nu) \; J_k\Big(\frac{4\pi\nu M_b}{c}\Big) \; J_l\Big(\frac{4\pi\nu M_h}{c}\Big) \tag{4.2}$$

$$\approx BW \; P(F_c) \; J_k\Big(\frac{4\pi F_c M_b}{c}\Big) \; J_l\Big(\frac{4\pi F_c M_h}{c}\Big), \tag{4.3}$$

where BW denotes the system bandwidth, and change of variable and mean value approximation have been invoked to derive Eqn. (Equation (4.3)).

A more accurate evaluation is performed to calculate the harmonics strength. Instead of using mean value approximation to evaluate Eqn. (Equation (4.1)) [12],

Table 4.1: Vital Signs Simulation Parameters

Chest Motion	**Resp. Rate**	**Heartbeat Motion**	**Heart Rate**
0.5∼5.5 mm	**15 BPM**	**0.08 mm**	**70 BPM**

the actual transmitted waveform has been taken into consideration. The synthesized transmitted pulse is modeled as cosine wave with a Gaussian envelope [98],

$$\begin{aligned} p(\tau) &= p_0(\tau)\cos(2\,\pi\ F_c\ \tau) \\ &= V_{\mathrm{Tx}}\ e^{-\frac{\tau^2}{2\sigma^2}}\ \cos(2\,\pi\ Fc\ \tau), \end{aligned} \tag{4.4}$$

where V_{Tx} is pulse amplitude of the Gaussian pulse envelope $p_0(\tau)$ and the Gaussian parameter σ determines the -10 dB bandwidth,

$$\sigma = \frac{1}{2\pi(BW/2)\sqrt{\log_{10}(e)}}. \tag{4.5}$$

Given the radar system parameters, center frequency $F_c = 7.3$ GHz and operating bandwidth $BW = 1.4$ GHz, the synthesized pulse waveform matches the measurement as seen in Fig. Figure 4.2.

For clarity, the strength of the respiration harmonics is compared to that of the heartbeat harmonics up to the 2$^{\mathrm{nd}}$-order. Then the strength of the higher-order inter-modulations is compared to that of the heartbeat harmonics of interest. The normal resting breathing rate for an adult is about 12-20 BPM and the heart rate is about 60 to 80 BPM on average [99]. For numerical analysis, the breathing rate is chosen as 15 BPM and the heart rate is chosen as 70 BPM. In this case, the 2$^{\mathrm{nd}}$-order harmonic of heartbeat (140 BPM) is competing against the 8, 9, and 10$^{\mathrm{th}}$-order harmonics of the respiration, ranging from 120 to 150 BPM. Here the higher-order harmonics that are close to the 2$^{\mathrm{nd}}$-order harmonic of heartbeat are considered, otherwise they can be easily filtered out. The spectrum magnitude of the harmonics of interest are compared

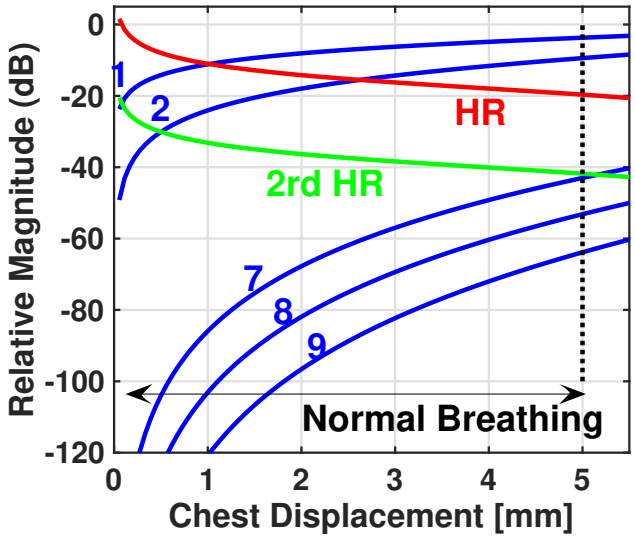


Figure 4.3: Harmonics strength as a function of chest movement

in Fig. Figure 4.3 as a function of chest displacement (respiration) from 0.5 mm to 5.5 mm with a fixed heartbeat magnitude 0.08 mm [75, 100]. In general, the magnitude of chest motion is on the order of millimeter and the heartbeat magnitude is about 0.01 millimeter [101]. For normal respiratory activities, the 2^{nd}-order harmonic of heartbeat is much stronger than those of the higher-order harmonics of respiration (8, 9, 10^{th}). For different chest displacement, the fundamental heartbeat experiences interference from the lower-order harmonics of respiration (3^{rd}). It should be noted that in general higher-order harmonics with order number $m = k + l \geq 4$, where k and l are from $C^{\text{B}}_{k,l}(\tau_0)$, cannot be easily observed due to the weak vital signs motion and the background noise. The main challenge of monitoring fundamental heartbeat continuously is the spurious spectrum peaks such as 2^{nd} and 3^{rd}-order harmonics of the respiration. Fortunately, they are spectrally further away from the 2^{nd}-order harmonic of heartbeat frequency. Therefore, it makes locating the heartbeat harmonics a respiration-interference free task.

Similarly, the strength of the higher-order intermodulations is compared against

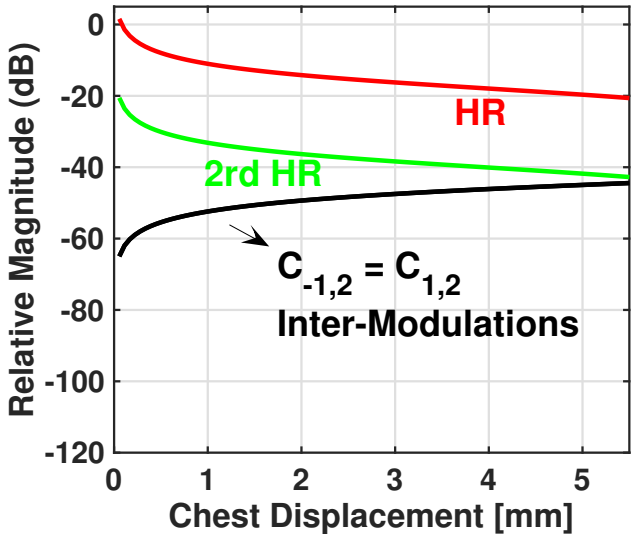


Figure 4.4: Intermodulations strength as a function of chest movement

the strength of the 2nd-order harmonic of the heartbeat signal in Fig. Figure 4.4. The associated intermodulations close to 140 BPM are $C^{\mathrm{B}}_{k=-1,l=2}(\tau_0)$ and $C^{\mathrm{B}}_{k=1,l=2}(\tau_0)$. Only the order numbers of the intermodulations $m \leq 3$ are considered.

4.3 Robustness Analysis

4.3.1 Two-Subject at Same Range

In this section, the higher-order spectral features are demonstrated to be robust statistics for recovering the fundamental heart-rate in a challenging scenario. Heart-rates are simultaneously estimated from two subjects. They are at an equal distance to the radar and perform normal breathing.

Two stationary subjects are seated 0.8 meter away from the recording devices. An UWB radar is placed on a tripod with a height of 1 meters and a Logitech webcam is placed on another tripod with a height of 1.3 meters. The experiment setup is shown in Fig. Figure 6.1. Each subject is wearing a Polar H10 chest sensor to provide a

reference. As for a second reference, a webcam-based heart-rate estimation system is implemented. The standard red, green and blue (RGB) video data recording the facial skins of multiple subjects is processed to produce the frequency analysis. The key processing components are multiple-face detection and tracking algorithm, and a color diferencing algorithm [102]. The real-time processing for radar and camera are implemented in Matlab. A 20-second moving processing window is applied for both systems.

In Fig. Figure 4.5 and Figure 4.6, a snapshot of the above experiments is provided. The two subject heart-rates estimation performance is compared to the other two types of references: a webcam system and chest heart-rate sensor. In Fig. Figure 4.5(a), one video frame is displayed. Two faces are detected and tracked as indicated by the square boxes, and the heart-rates for each detected subjects are printed out as well. In Fig. Figure 4.5(b), the heart-rate readings from the chest sensors are shown. In Fig. Figure 4.6, the cardiac harmonics spectrum of the two subjects from the radar system is shown. The 2^{nd}-order harmonics of subject 1 and subject 2 are 108.6 and 161.4, as indicated by the red and blue markers, thus the recovered fundamental heart-rates for the two subjects are 54 and 81 (rounded to BPM). The webcam and the radar have consistent performance, and the radar heart-rate readings are only one beat different from the chest heart-rate sensor. The experiment results are summarized in Table Table 4.2.

In the previous example, the two subjects' heart-rates are far apart about 30 beats difference. In the second example, the 2^{nd}-order spectral features of heartbeat are still visible even when the two subjects' heart-rates are relatively close. In Fig. Figure 4.7, the two heartbeats can be easily identified. There is only a fraction of beat difference between the radar and the camera estimates.

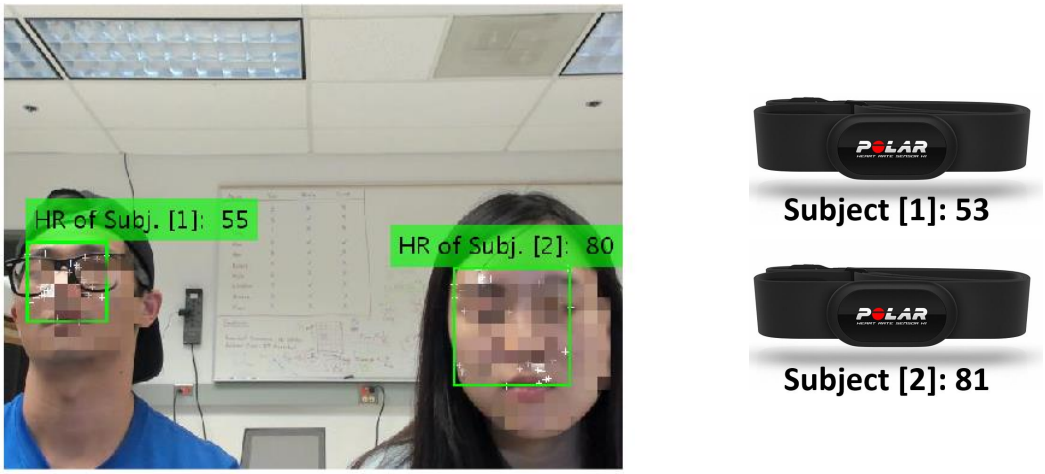


Figure 4.5: Heart rate readings from the reference systems: (a) camera based monitoring system; (b) chest strap heart-rate monitor

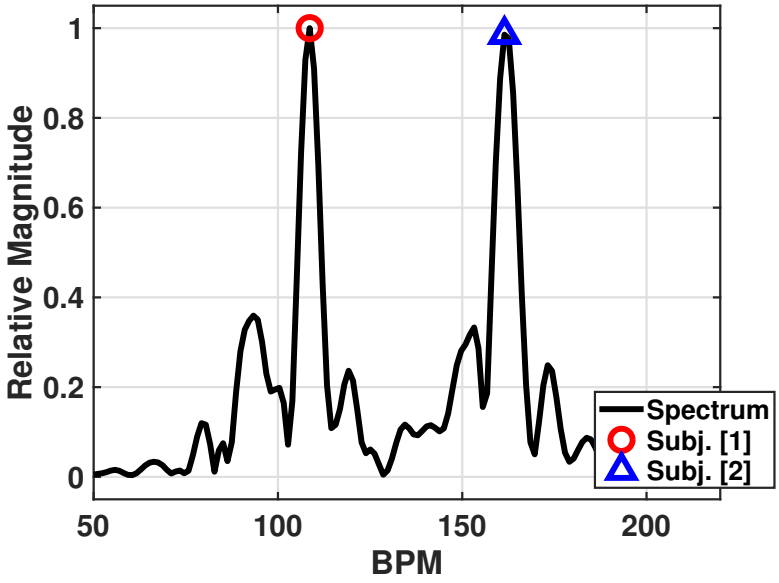


Figure 4.6: Second-order heartbeat harmonics spectrum of the two subjects measured from the radar system

Table 4.2: Summary of Experiment Results (Unit in BPM)

	Subject [1]	Subject [2]
Radar	***54***	***81***
Camera	***55***	***80***
Chest sensor	***53***	***81***



Figure 4.7: Two heart-rates detection at equal distance

4.3.2 Small-scale Motion Resistance

In references [12][14][13], the higher-order harmonics related to the heartbeat activity have been shown numerically and experimentally to be a robust statistics when the test subject is stationary.

Additionally, the higher-order harmonics of heartbeat is robust against the small body motion. In this realistic example, the test subject is sitting about 0.6 meter away from the radar and facing the radar sensor sideway about 45 degrees. During the experiment, the test subject is constantly using cellphone . In Fig. Figure 4.8(a), the

range-slow-time heatmap is shown. The strong energy reflection due to chest motion occurs at about 0.6 meter. The motion is spread across quite a few range bins, up to 1 meter. In the range direction from 0.67 to 0.85 meter, the discontinuity of the energy spread occurs during the entire recording. The respiration pattern fades way at these distances because of the hand motion noise. In order to demonstrate the robustness against the hand motion noise, a range bin at 0.69 meter is carefully chosen which contains both the vital signs and the hand motion. The corresponding results are shown in Fig. Figure 4.8(b)(c). In Fig. Figure 4.8(b), the vital signs spectra from different methods are compared. Front the top to the bottom plots, they are results from CSD method, phase-based method and the 2^{nd}-order method. Interestingly, the lower frequency region up to the possible fundamental heartbeat region is very noisy due to the hand motion while in the relatively higher frequency region the trace of the 2^{nd} heartbeat harmonics is clearly visible and therefore can be easily isolated. Finally, in Fig. Figure 4.8(c), the continuous measurement results from the CSD method, the phased-based method and the 2^{nd}-order harmonic of the heartbeat are shown. Only the 2^{nd}-order method can provide consistent and slow-varying estimates over time in present of hand motion.

4.4 Limitation Analysis

In previous section, the feasibility analysis of recovering the fundamental heartbeat frequency with the aid of its 2^{nd}-order harmonic in the spectral domain is demonstrated. In this section, a few limitations for continuous heart rate monitoring for stationary subject using the harmonics-based approach are identified. Sufficient signal-to-noise ratio (SNR) is needed in order to detect the 2^{nd}-order harmonic of the heartbeat signal. The spectrum energy of the heartbeat signal is about 20 dB lower than that of the fundamental respiration. One would expect heartbeat harmonics

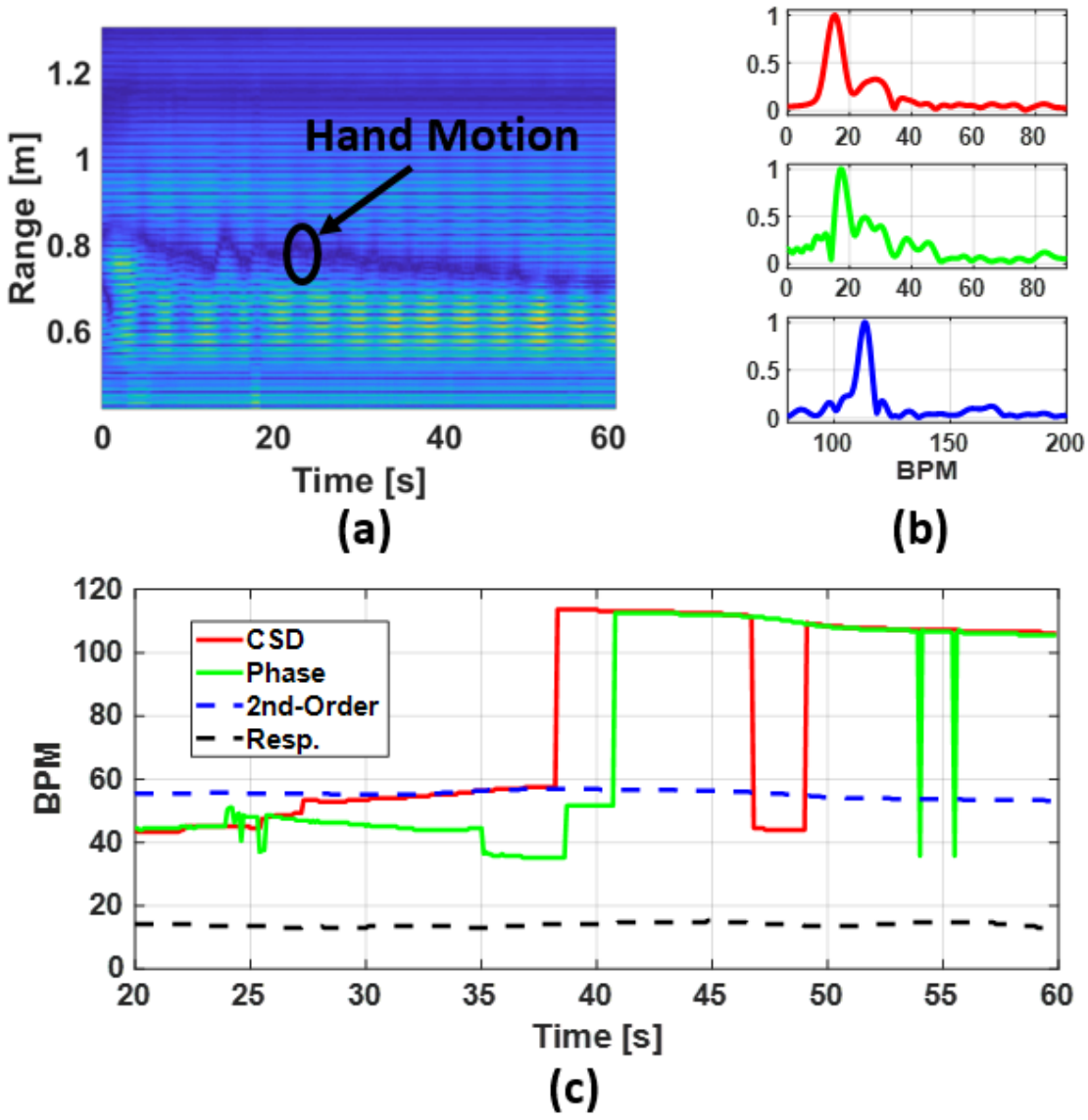
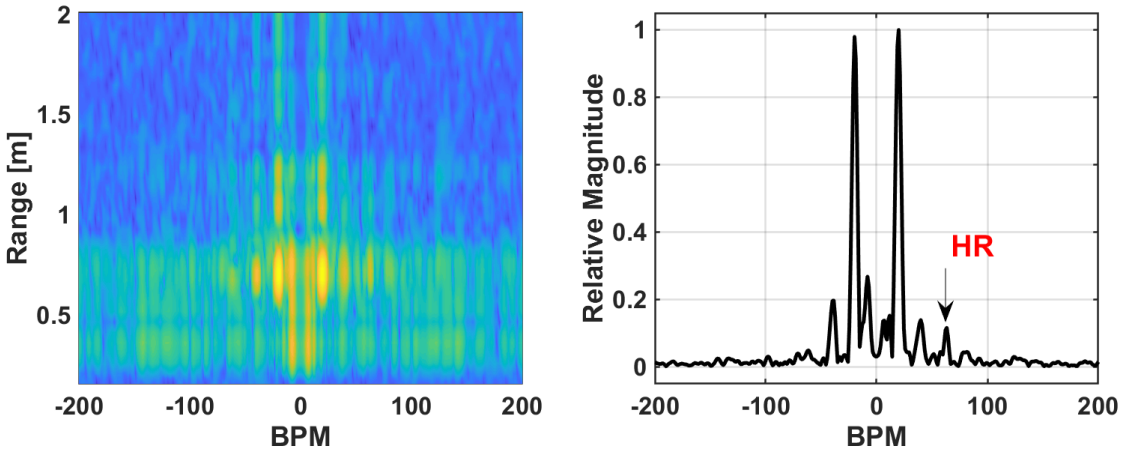


Figure 4.8: Small-scale motion performance example. (a) range-slow-time heatmap; (b) vital signs spectrum comparison, top plot: CSD; middle plot: phase-based; bottom plot: 2nd heartbeat harmonic; (c) heart-rate evolution comparison. Note that (b)(c) are generated using range bin 0.69 meter which contains both vital signs motion and hand motion.



(a) Range-Doppler map (b) Spectrum at the range bin of interest

Figure 4.9: Example when heartbeat harmonics is not visible

to be even weaker. The monitoring performance is very sensitive to the background noise and random body motion. This method therefore fails when the test subject is seated further away, or wearing thick clothes. In order to boost the vital signs SNR, the output frame rate of the radar is set to as low as 10 Hz. The maximum pulse rate is about 50 MHz and processing gain is achieved by coherently combining many pules.

4.5 An Adaptive Heart-Rate Combination Algorithm

Heartbeat Harmonics Filter Design

In this section, adaptively utilizing the available fundamental heartbeat and its associated harmonics is proposed in order to make continuous measurement possible. Relying solely on recovering the fundamental heartbeat frequency or heart-rate from its 2^{nd}-order harmonic can lead to inaccurate estimation as seen in Fig. Figure 4.9 when the heartbeat harmonics spectrum becomes noisy. In order to alleviate the heart-rate drifting effect, two bandpass heartbeat harmonics filters are designed. The

primary filter γ is to filter out the spectrum content for the 2^{nd} or 3^{rd}-order heartbeat harmonic and therefore estimate its frequency f_{HCS}. The secondary filter η is to estimate the fundamental heartbeat frequency f_{1st}. Only the lower cut-off frequencies need to be determined while the upper cut-off frequencies are trivial. According the resting adult heart rate statistics in Section Section 4.2, the frequency limits of the two harmonics filter are determined as,

$$\begin{aligned} &\gamma, \text{filter range}: \ 1.5 \leq f \leq 4\text{Hz}; \\ &\eta, \text{filter range}: \ 0.7 \leq f \leq 4\text{Hz}. \end{aligned} \tag{4.6}$$

Thus, in addition to recover the heartbeat frequency from its harmonics, the secondary filter η provides a second way to estimate the heartbeat frequency. The goal is to selectively combine different sources of frequency estimates and generate more robust estimate, so continuous real-time monitoring is possible.

4.5.1 Spectral Peak Selection Criterion

To further improve the robustness of our heart-rate estimation algorithm, two efficient processing steps are proposed. First, full frequency spectrum are used for spectral peak localization, meaning that both the negative and positive spectrum are utilized since the I and Q data are used for spectral analysis. As demonstrated in Fig. Figure 4.10, the spectral peak is present in the negative spectrum part not the positive part. Second, when two spectral peaks with similar absolute frequency locations are present in the positive and negative spectrum as shown in Fig. Figure 4.11, the selection is based a new criterion, called peak to noise level (P2NL), instead of solely relying on the peak height,

$$\text{P2NL} = \frac{\sum_{i=\text{pos}-2}^{\text{pos}+2} V_i}{\sum_{j=\text{pos}-50}^{\text{pos}+50} \text{V}_j}, \tag{4.7}$$

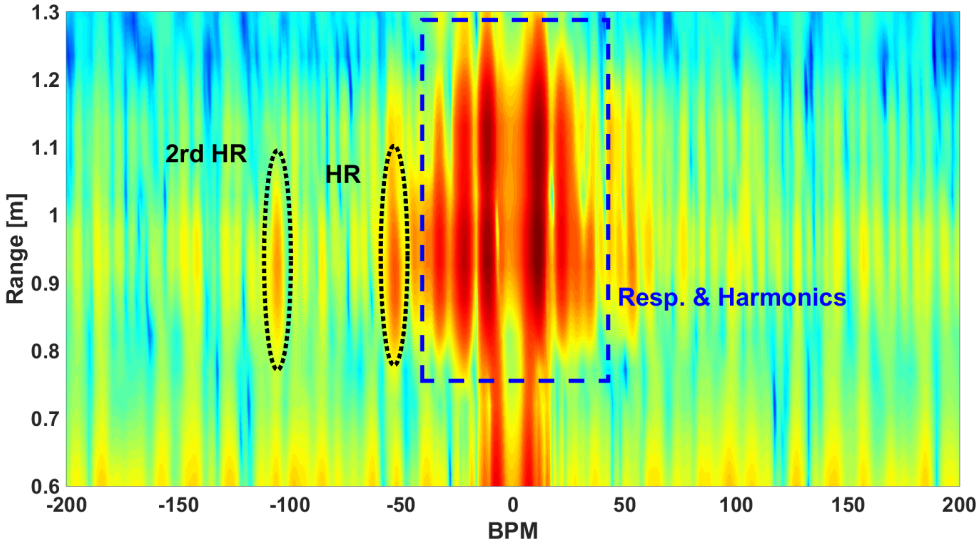


Figure 4.10: Heartbeart frequency & its 2nd-order harmonic present in the negative spectrum

where V_{pos} is the peak spectral value at pos-th position. The numerator is sum of the peak value and nearby 2 data samples to the right and to the left, total 5 data samples. The denominator is sum of the corresponding 101 data values include the peak values and the noise-like data values. Based on this criterion, one of the two competing peaks with larger P2NL value is selected. A more noise-robust peak spectrum gives a larger P2NL value.

4.5.2 Adaptive Heart Rate Selection Scheme

In this section, an adaptive heart-rate selection scheme is presented by summarizing the results in previous sections [14]. A 20-second moving processing window is used and shifted by one sample each time when a new frame is captured. The algorithm starts outputting the heart-rate reading only if the frequency estimate of the 2nd-order harmonic of the heartbeat is stable for one second, meaning that the

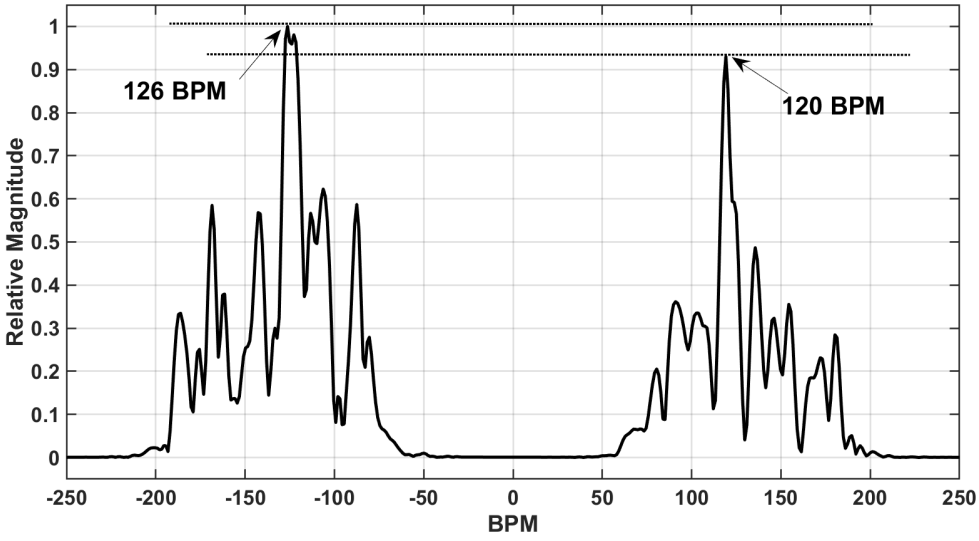


Figure 4.11: Potential estimation error due to spectral peak selection

heart-rate estimate $f_h = f_{\text{HCS}}/2$ is stable for 10 consecutive estimates and the variation is less than 3 beats. These estimates are obtained by applying the primary bandpass filter γ and selecting the peak location based on the P2NL criterion in Eqn. (Equation (4.7)). The purpose of waiting for stable estimates is to make sure the spectral peak is heartbeat harmonics not some random peaks. As demonstrated in Section Section 4.2, a stable spectral peak in the 2^{nd}-harmonic frequency region is the result of the cardiac activity with high probability.

Similarly, the secondary heart-rate estimate is obtained using the filter η. These estimates are stored along with the primary estimates from γ. But they are only checked when the primary estimate start fluctuating wildly, such that the difference between the current estimate at time instance t and the previous output heart-rate at time instance $t-1$ is larger than 3 beats, $|f_h^{t-1} - f_{\text{HCS}}^t/2| > 3$ and $|f_h^{t-1} - f_{\text{HCS}}^t/3| > 3$. Here two situations are considered. The dominant spectral peak location f_{HCS} can be either the 2^{nd}-order harmonic of heartbeat or occasionally the 3^{rd}-order harmonic.

If the current estimate f_{HCS}^t is is different from the two possibilities $2f_h^{t-1}$ and $3f_h^{t-1}$ by more than 3 beats, then the secondary estimate is compared against the previous output heart rate f_h^{t-1}. The secondary estimate is used when the difference is small such that $|f_h^{t-1} - f_{1\text{st}}^t| \leq 3$ and thus is chosen as the current output heart-rate $f_h^t = f_{1\text{st}}^t$. Otherwise, both the current primary and the secondary estimates are ignored. The algorithm stops and print out warning message "Possible unreliable estimate due to body movement!"

Above procedure is repeated every time when a new data frame comes in until the recording time is reached. The proposed adaptive heart-rate selection scheme is summarized in Table Table 4.3.

Table 4.3: Adaptive HR Selection Scheme

Moving processing window 20-s, with 1 sample increment each time

$t = t_0 \rightarrow$ **Start** processing when 200 frames of data is available

$\vdots$

$t = t_1 \rightarrow$ **Output** the first HR reading $f_h = f_{\text{HCS}}/2$

if f_{HCS} is stable for 1-s or 10 consecutive estimates

$\vdots$

$t = t_2 \rightarrow$ **Check** the difference between the current f_{HCS} and the previous f_h

if $|f_h - f_{\text{HCS}}/2| \leq= 3$,

then output $f_h = f_{\text{HCS}}/2$

else

check if f_{HCS} is close to the 3rd HR

if $|f_h - f_{\text{HCS}}/3| \leq= 3$

then output $f_h = f_{\text{HCS}}/3$

else

check the secondary estimate

if $|f_h - f_{1\text{st}}| \leq= 3$

then output $f_h = f_{1\text{st}}$

else

print out warning message and stop algorithm

end

end

end

$\vdots$

$t = t_3 \rightarrow$ **Repeat** previous procedure until reach the recording time

Chapter 5

A PRECISE PHASE CALIBRATION ALGORITHM FOR IMPROVED HEARTBEAT DETECTION

In this chapter, in-depth discussion about the phase calibration required by phase-based method for heartbeat detection is provided. The situations when the existing phase calibration technique fails are examined. A precise phase calibration routine

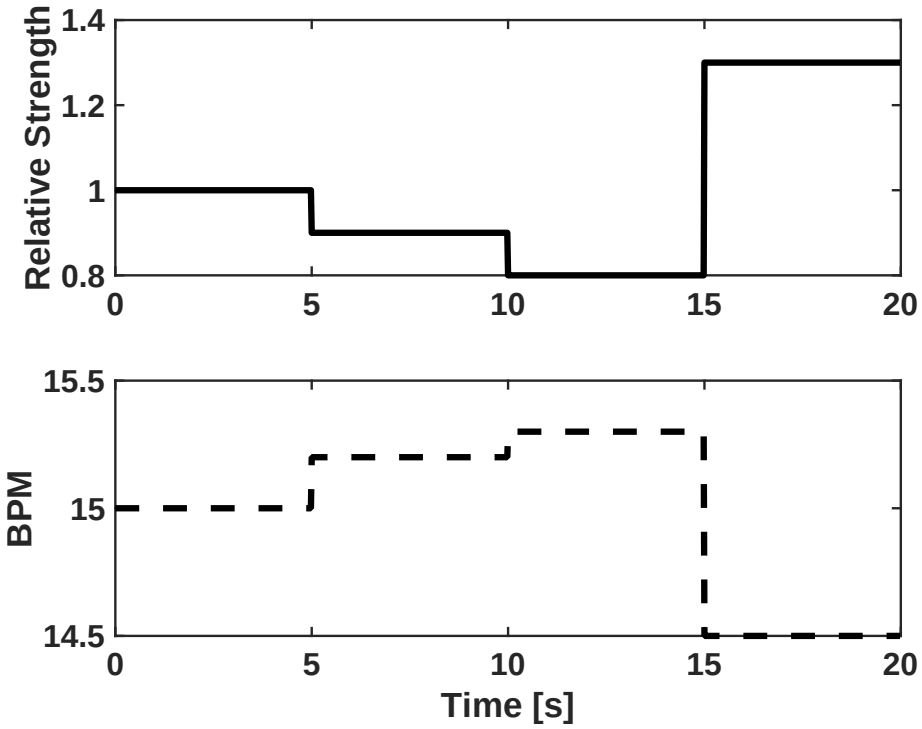


Figure 5.1: Piece-wise stationary respiration parameters. Top Plot: received signal levels relative to the nominal received signal magnitude; bottom plot: the corresponding respiration frequencies in BPM.

guided by some intuitive observations is proposed.

5.1 Respiration Modeling

The most convenient way to model vital signs is to use two sinusoids with different amplitudes and frequencies as shown in Eqn. Equation (3.1). Though it is a simplified model but it allows analytical analysis in the spectral domain. Other model was considered in reference [103]. However, these models are static and cannot capture the time-varying nature of respiratory activity. Therefore one way to model respiration is to using a time varying target response A_T and f_{b}. A piece-wise stationary model is considered for the target response and the nominal respiratory frequency. Note that these two parameters determines the received signal strength and the duration of each breath. An example of the time-varying model is shown in Fig. Figure 5.1. During a 20-s observation, there are 4 stages with different target response and different instantaneous respiratory frequencies. The levels of target response are normalized to the vital signs signal strength and the respiratory frequencies are normalized to the nominal frequency. Also the two parameters are negatively related. That's because more chest area is involved in a strong or deep breath. Increased signal level is received due to the increased radar cross-section. At the same time, breath interval generally increases and thus the instantaneous respiratory frequency decreases.

5.2 Sources of Phase Noises

Two types of phase noises should be considered in order to extract the phase variations directly related to vital signs. The first one is large-scale phase noise, DC-offset. This DC-offset is determined by the nominal distance between radar and human subject, and the radar system parameters as shown in Eqn. Section 3.4.1. In literature, the DC-offset is often treated as a constant phase noise term during

the coherent processing window by practitioners. However, this is not the case in realistic situation. Especially for continuous measurement, the center location of the human subject drifts over time. The central idea of DC-offset compensation is to circle-fit a group of I/Q samples that experience similar motion noise. There is no prior knowledge about which of these I/Q samples need to be corrected as pointed out in references [13][14]. The different choices of phase calibration intervals produce very different results as shown in Fig. Figure 5.2 and Figure 5.3. The second type is small-scale phase noise, which is mainly hardware-limited. This sort of phase noise is often treated as added random noise independently present in the I/Q channels.

5.3 Simulation Analysis

An simulated example is illustrated in Fig. Figure 5.2 and Figure 5.3 to demonstrate the effect of the time-varying modeling on the phase calibration results. The simulation results are generated using the piece-wise stationary model in Section Section 5.1 with the other vital signs parameters in Table Table 4.1. Similarly, a piece-wise stationary DC-offsets are considered, in which the DC-offset changes every 5 seconds. The DC-offset level is about 25% of the nominal magnitude of vital signs signals. The small-scale phase noise in I/Q channels is modeled as zero-mean Gaussian random variable with a standard deviation of 1/30 of the vital signs signal magnitude.

With the prior knowledge about the simulation model, the I/Q data samples experience similar phase noise are corrected together. In this way, the precise phase variation is extracted as show in Fig. Figure 5.2. One intuitive example is demonstrated in Fig. Figure 5.3 to graphically show that circle-fitting operation fails without considering the non-stationary nature of respiratory activity.

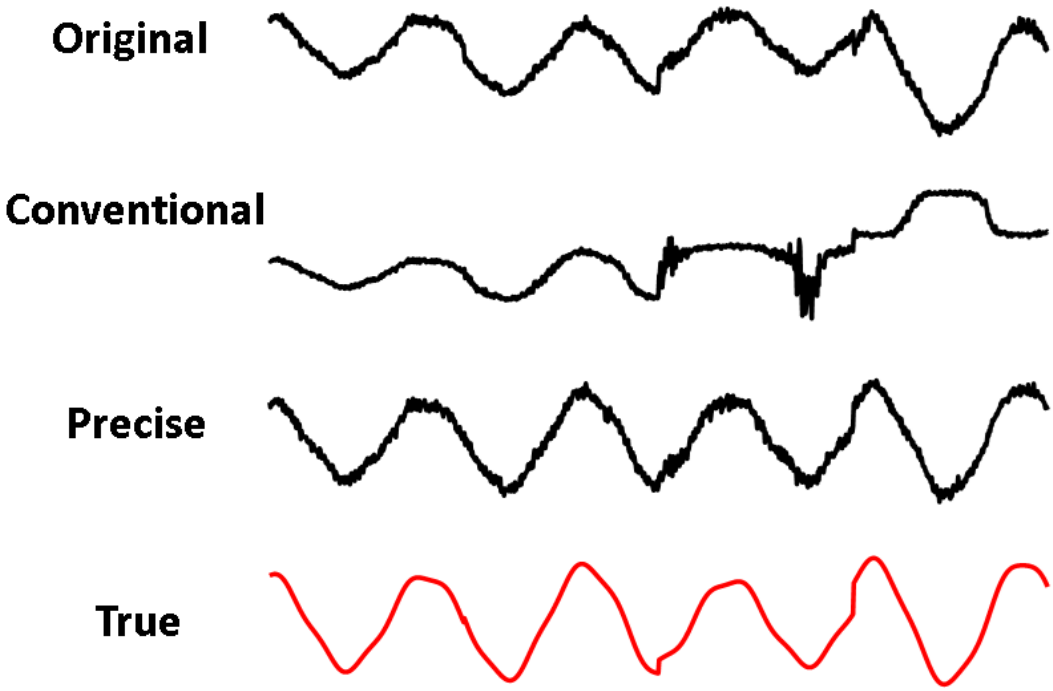


Figure 5.2: Comparison of phase recovering performance. X-axis denotes time in seconds.

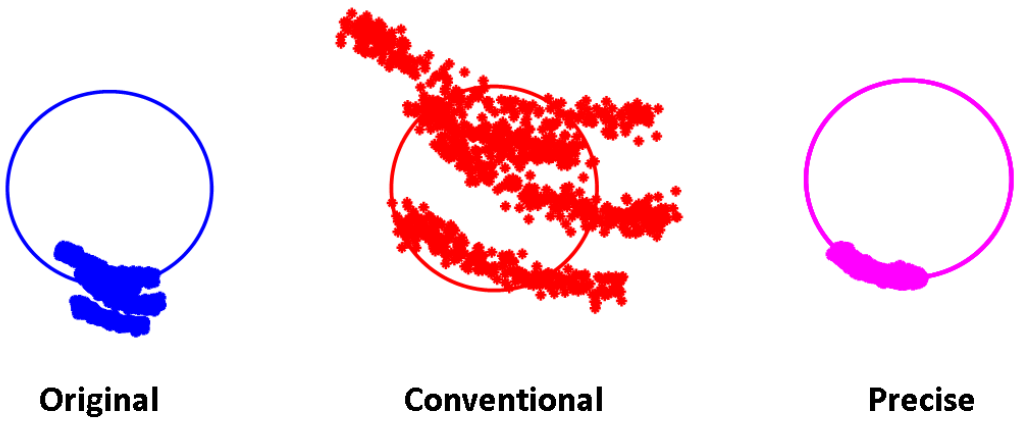


Figure 5.3: Circle-fitting results for non-stationary motion. Note the above results are normalized with respect to the unit circle.

5.4 Proposed Phase Calibration Criteria

One intuitive idea to find the I/Q sample points belonging to same phase arc in the constellation plot is to use the respiration pattern. If nearby breaths have similar shape, the corresponding I/Q sample points are mostly to be experiencing the same phase noise. Therefore the circle-fitting technique is applied to the selected I/Q samples to correctly recover the DC-offset and compensate for it.

5.5 Automated Phase Calibration Algorithm

In this section, an automated phase calibration algorithm capturing the time-varying nature of the phase noise is presented by summarizing the above results. In particular, the reconstructed respiration pattern is used to guide phase calibration. For a normal breathing or a non-controlled breathing pattern, each breath can be different from the other. Some breaths have larger magnitude and some have smaller magnitude while some have longer interval and some have shorter interval. Therefore, the circle-fitting operation is proposed to apply to each breath independently for precisely DC-offset compensation.

First, the respiration pattern is accurately estimated using the direct sampled RF signal. As shown in references [75][13], the RF signal preserves the vital signs information. The variations of the RF signal across the slow-time at the range of interest is a good approximation of the chest motion. The other advantage of using RF signal for estimating respiration pattern is to avoid the I/Q channel selection in the complex-baseband due to the null detection point problem [73]. An comparison of a reconstructed respiration waveform and the reference respiration signal from a chest sensor is provided in Fig. Figure 5.4.

Second, the reconstructed respiration waveform is further processed by separat-

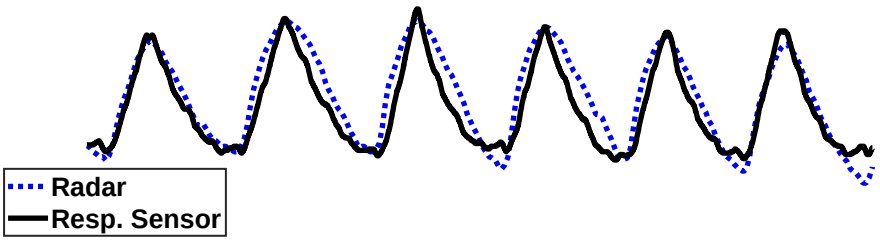


Figure 5.4: Respiration pattern estimation

ing out each breath. For this purpose, the waveform is multiplied by -1 and each local peaks in the inversed waveform can be located since the peak to peak interval corresponds to one breath. To reduce false peak detection, the respiration waveform is passed through a smoothing filter at the respiration frequency of interest.

Third, the raw RF data samples that correspond each breath within every coherent processing interval are associated and grouped using the results in the second step. The reason for using raw RF signal is that before performing phase calibration the DC information should be retained for accurately DC-offset estimation and compensation [72]. After down-conversion to the complex-baseband, the circle-fitting operation is independently applied to the I/Q sample data points associated to every breath. For convenience, the incomplete cycles of breath before the first peak and after the last peak are ignored. In this way, the DC-offset from each breathing cycle is accurately estimated and compensated. Occasionally, a 180-degree phase shift error occurs as shown in Fig. Figure 5.7 as indicated by the green curve. This phase error is corrected by flipping the signs of the DC-offsets in I/Q channels. In practice, the starting position of the phase variation from vital signs can be arbitrary. Then the chest motion generates a different arc at every breath on the unit circle after initial phase calibration. But all these arcs should approximately be in a same direction with respect to the I/Q axes as shown in Fig. Figure 5.5. Additionally, in order to minimize the occurrence of the 180-degree phase shifting error from the circle-fitting

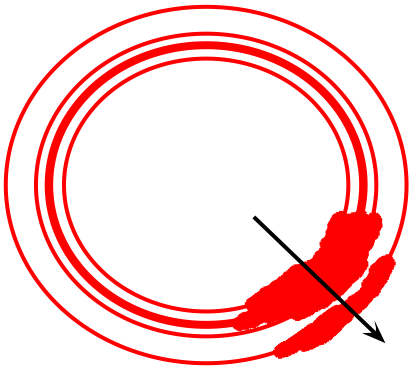


Figure 5.5: The common direction of the finely corrected I/Q samples

algorithm, a higher slow-time sampling rate is used, in which the sampling rate is increased from 10 to 50 frames per second. By doing so, the circle-fitting algorithm has sufficient I/Q sample from every breath to process and therefore reduces the phase discontinuity due to these phase shift errors.

Finally, the desired phase variation inform is obtained by combing the result from each breath after correcting the DC-offsets and the 180-degree phase shift errors. Note that normalization of the corrected phase signal is not necessary once the DC-offsets are correctly compensated. The automated precise phase calibration algorithm is illustrated in Fig. Figure 5.6. An graphical representation of this routine is shown in Fig. Figure 5.7. In this representative example, the precise phase calibration method (purple curve) achieves a much better fit than the conventional method.

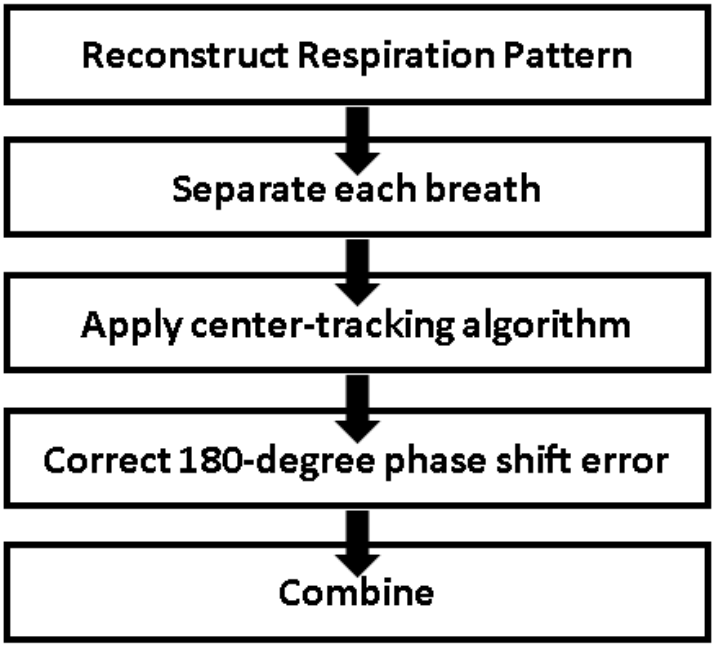


Figure 5.6: High-level processing diagram of an automated phase calibration routine

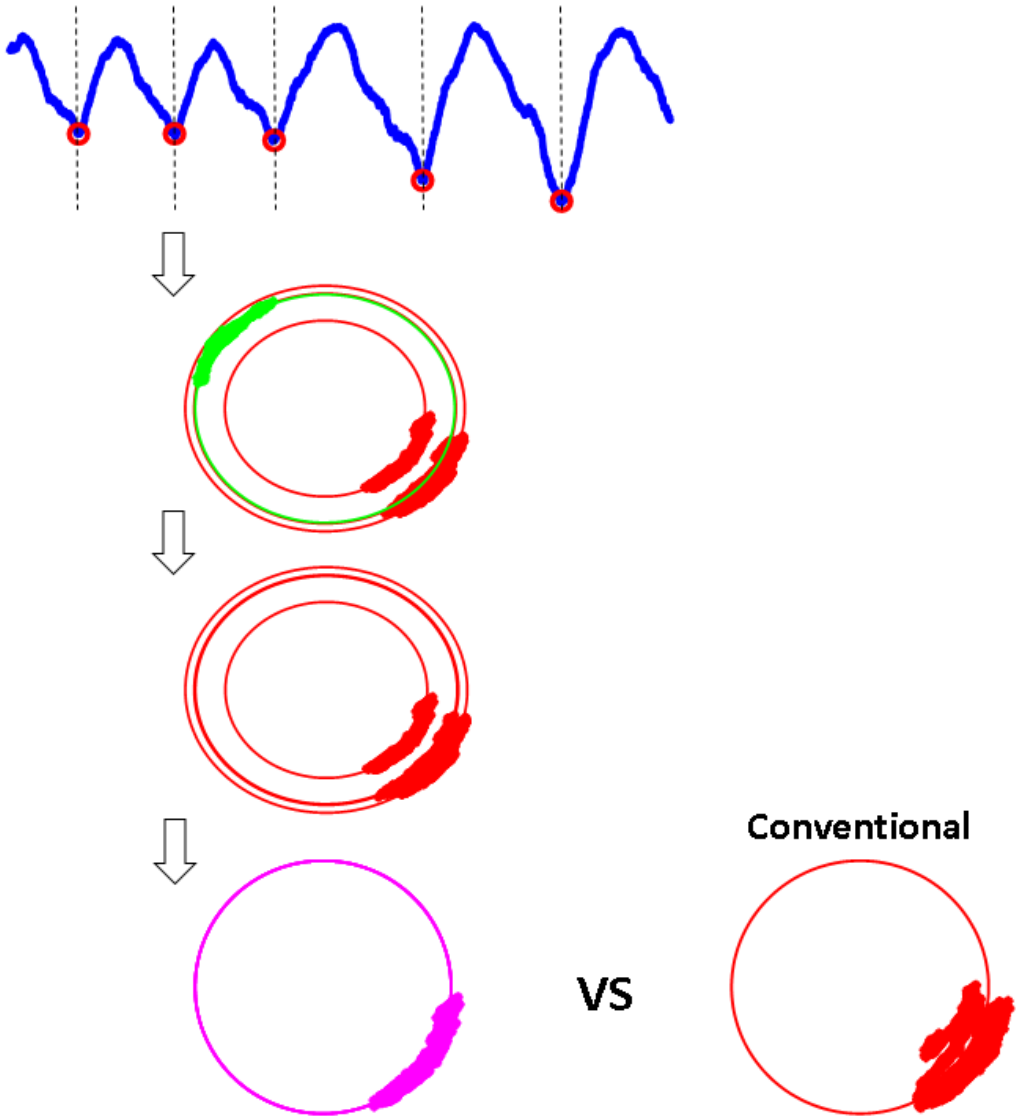


Figure 5.7: Graphical representation of the phase calibration routine

Chapter 6

MEASUREMENT SYSTEMS

Different types of devices are used for taking heart-rate measurement through out the experiment. They are radar-based system, camera-based system and conventional devices that require direct contact to human body. The radar-based technology is the focus. The proposed heart-rate monitoring algorithm is validated by comparing heart-rate estimation performance to the conventional devices such as ECG sensor or PPG sensor. Additionally, the heart-rate monitoring performance using the radar technology is compared to the RIPPG sensor, a camera-based system. A typical experimental setup is shown in Fig. Figure 6.1.

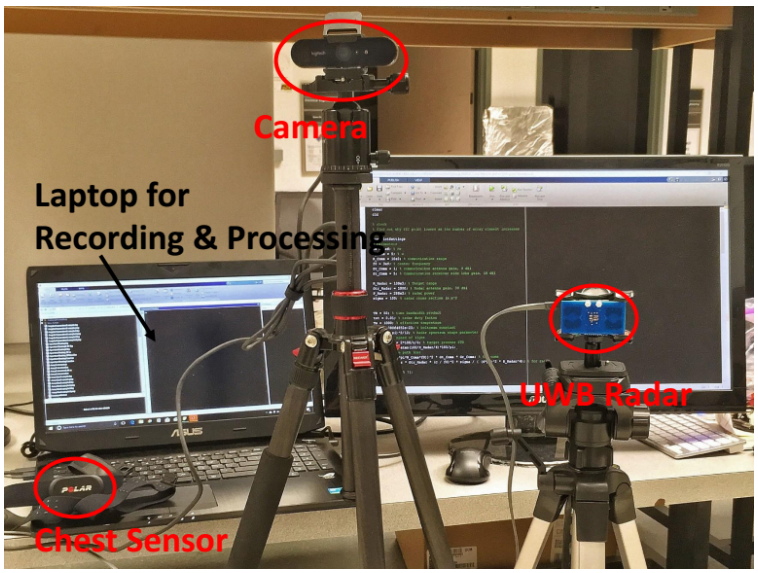


Figure 6.1: Typical experimental setup

Table 6.1: Radar System Parameters

Specification	**Values**
Center frequency	7.29 GHz
Bandwidth	1.4 GHz
Fast-time (RF) sampling rate	23.328 GHz
Slow-time sampling rate after coherent combing	10 Hz
Detection range	up to 5 m
Coherent processing time	20 s

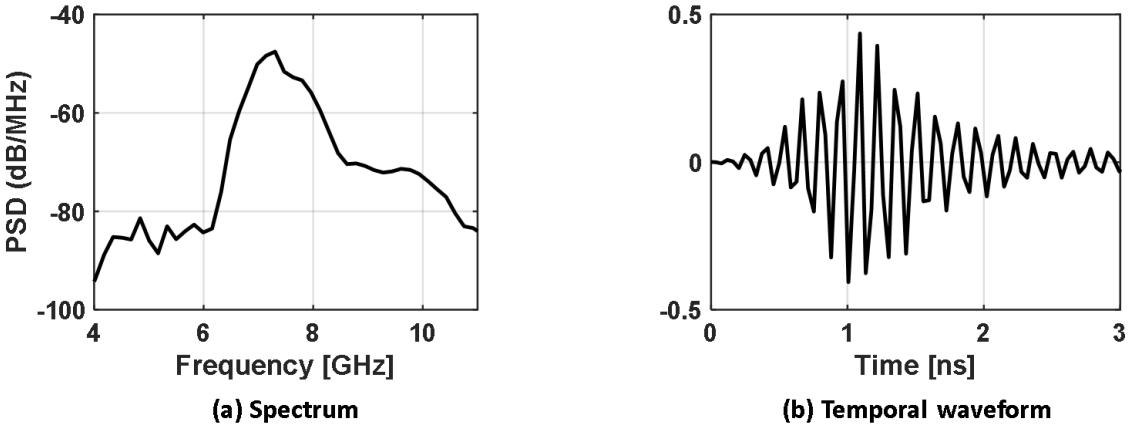


Figure 6.2: Characteristics of the UWB signal in frequency and time domains

6.1 Radar Sensor Parameters

The UWB impulse radar sensor is the Xethru X4M03 development kit*. The impulse pulse shape has the form of higher-order Gaussian derivative function as shown in Fig. Figure 6.2. The detailed hardware design can be found in reference [98]. The radar system parameters are summarized in Table Table 6.1.

* https://www.xethru.com/shop/x4m03-development-kit.html

6.1.1 System Features: Vital Signs Radar

Traditional radar approaches are based on transmitting high energy levels to obtain the necessary SNR in applications, which is not feasible for daily life usage. No one wants a high-power radar sitting nearby. UWB impulse radar is able to provide a robust vital signs monitoring solution at a low cost, with low power consumption and low RF emission, providing highly accurate vital signs data for consumer applications.

Some of the key features implemented in Xethru X4M03 development kit is illustrated in Fig. Figure 6.3. One of the key features is digital lossless integration, and the ability to gain a high SNR, which is especially needed when tracking respiration pattern and monitoring heart-rate. The system coherence, absolute timing control, and a sampling rate of 23.328 Giga-Samples/second enables highly accurate distance measurement.

The highly compact UWB radar system architecture based on integration and a highly power-efficient transmitter emitting extremely low transmit power illustrated in Fig. Figure 6.4, is a result of tight regulatory and system power constraints. As a result, a comforting feature with the UWB implementation is that a maximum of -41.3 dBm/MHz is emitted, which is the 47 CFR Part 15 limit defining how much electronic devices can emit unintentionally, such as alarm clocks, hair dryers or toasters.

6.2 Remote Imaging PPG System

The completing remote sensing technology for radar technology is RIPPG. Such technology like camera-based approach for vital signs has been successfully implemented in references [24, 102]. The challenge faced by the radar systems is not present in the camera-based systems since the heartbeat pulse is extracted from the reflected light due to blood changes in the facial skins. Given sufficient lighting condition, for

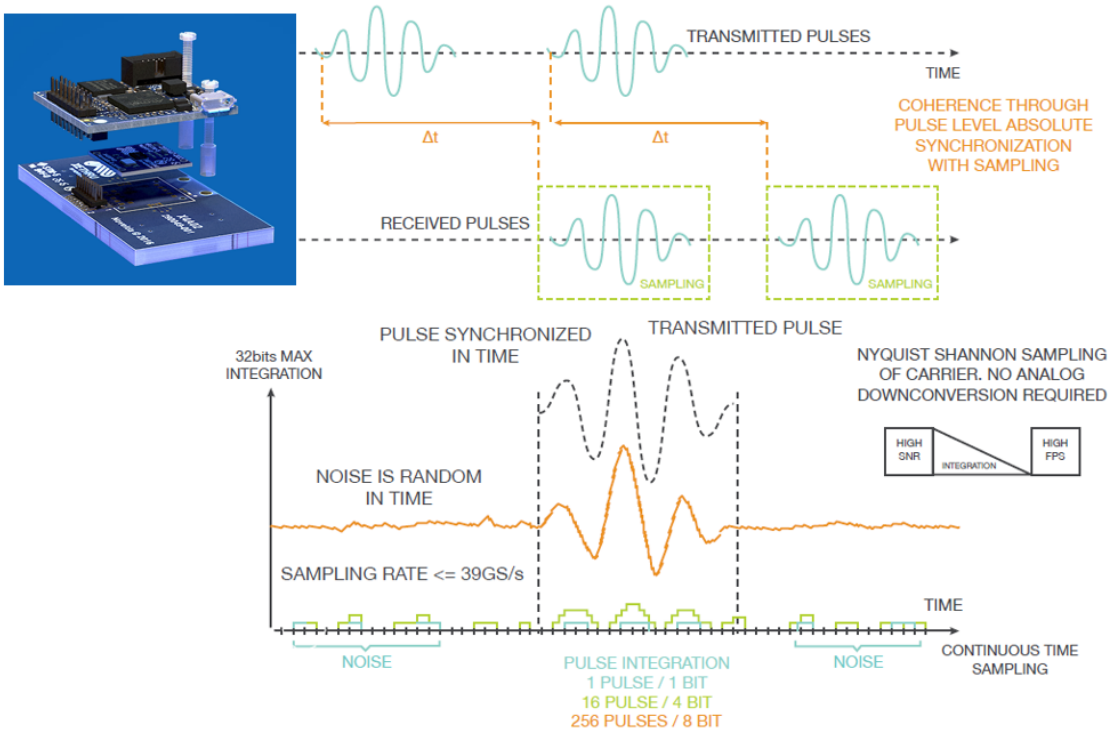


Figure 6.3: Operating Principle*

stationary subject, the camera-based systems can be used as a reference system for the radar-based heart-rate monitoring systems. Additionally, the camera-based systems can be readily extended to include multiple-face tracking and multiple-heartbeats monitoring functions. Therefore, the heartbeat detection performance of multiple subjects using radar system is benchmarked against the camera system. Some of the key system parameters of the implemented camera-based heart-rate monitoring system is summarized in Fig. Table 6.2.

.

* https://www.xethru.com/community/resources/categories/xethru-resources.2/

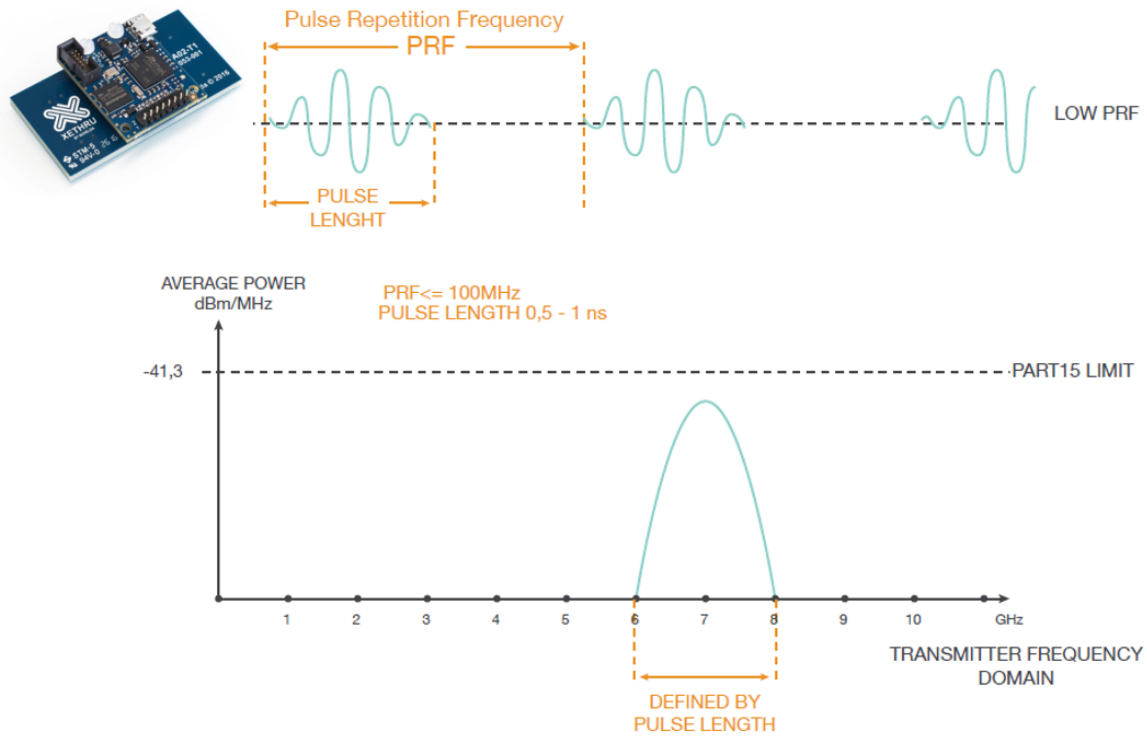


Figure 6.4: Low-Power UWB pulse*

Table 6.2: Imaging System Parameters

Device	**Logitech web cam**
Resolution	**640 x 480**
Frame rate	**30 fps**
Coherent processing time	**20 s**
Camera to target distance	**0.8∼1 m**

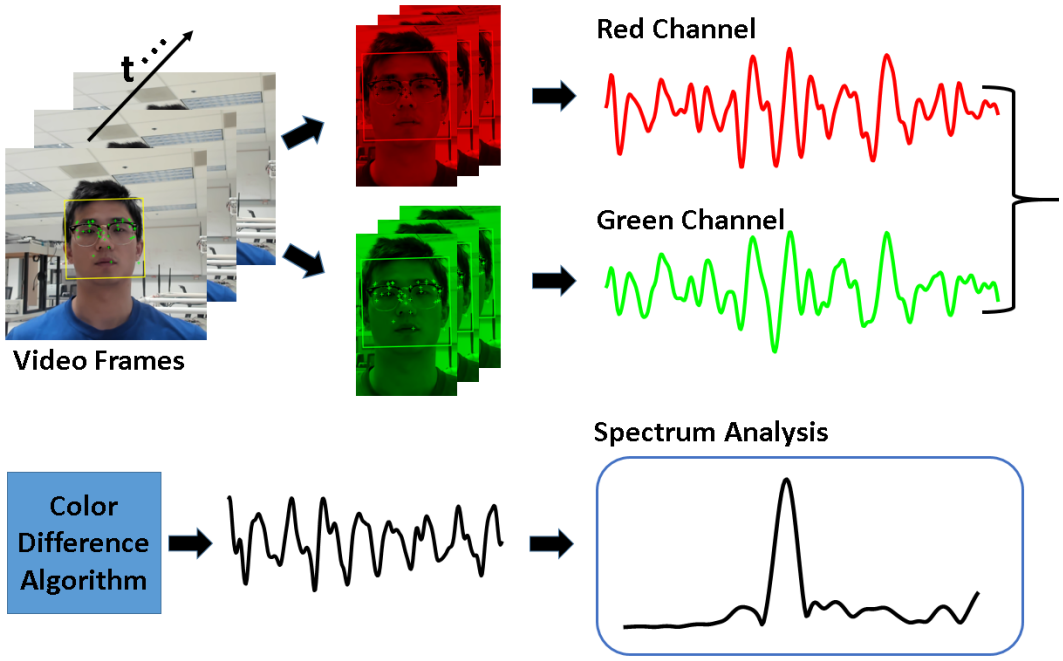


Figure 6.5: A signal processing diagram for camera-based heart-rate estimation

6.2.1 Principle of Operation

PPG is an optical technique that measures the intensity of light reflected (transmitted) through tissue in order to extract physiological information including the heartbeat pulse. A well-known commercial device that utilizes this principle is the pulse oximeter. In a pulse-oximeter, light (usually green light) travels from a source from one surface of the subject's finger to reach a photodetector on the other surface since the light traverses though the finger tissue and interacts with the vasculature contained within the tissue. The intensity of the received (light) signal shows oscillations due to pulsatile flow, which in turn is used to obtain the heart-rate. The RIPPG systems, such as cameras, function in the same fundamental principle but remotely. By applying signal processing techniques, the standard RGB video frames from exposed skin are processed to produce a periodic time-domain signal whose dominant spectral frequency is the heart-rate of the subject being recorded. A high-level signal

processing diagram of camera-based heart-rate estimation using a color differencing algorithm [102] is illustrated in Fig. Figure 6.5

6.2.2 Signal Model

The mathematical model of vital signs extraction using RIPPG signal is reviewed [102]. The raw RIPPG signal is obtained by averaging all the image pixel values within the facial region of interest (ROI) in each color channel,

$$\begin{aligned} \mathrm{RIPPG}_i(t) &= \frac{\sum_{x,y\in \mathrm{ROI}} P_i(x,y,t)}{|\mathrm{ROI}|} \\ i &= \textbf{Red, Green, and Blue}, \end{aligned} \tag{6.1}$$

where |ROI| denotes the number of pixels in the facial ROI and $P_i(x, y, t)$ is the pixel value located as $(x,\ y)$, at time instance t. The RIPPG signal originates from the light absorption variation of the skin with blood volume changes. The amplitude of light absorption variation with blood volume change is very small compared with that of the average remittance, appearing as a small AC (a non-constant) component added to a larger DC component. For the reflection mode of contacted PPG signal, the AC/DC ratio of the PPG signal is wavelength dependent as shown in Fig. Figure 6.6. For the RIPPG signal, the peak AC/DC ratio is even smaller about 2%. The optical signal of the RIPPG is represented as,

$$I_i = \alpha_i \beta_i \big(S_0 + \gamma_i \, S_0 \, \mathrm{Pulse}(t) + R_0\big), \tag{6.2}$$

where Pulse(t) is the normalized ideal RIPPG signal, S_0 is the average scattered light intensity from the facial ROI with light illumination. R_0 is the diffuse reflection light intensity from the surface of the facial ROI. α_i is the power of the i-th color light in the normalized illumination spectrum, β_i is the power of the i-th color light in the normalized diffuse reflection spectrum of the skin, and γ_i is the AC/DC ratio

of a RIPPG signal in the i-th color channel. The spectral characteristics of the environmental illumination and the skin remittance are considered in this optical signal model of RIPPG. Eqn. Equation (6.2) can describe the RIPPG model in an ideal case. When the head motion occurs, this motion will modulate the RIPPG signals in the RGB color channels in the same way. The motion effect can be expressed as,

$$I_i(t) = \alpha_i \ \beta_i \ \left(S_0 + \gamma_i S_0 \text{Pulse}(t) + R_0\right) \ M(t), \tag{6.3}$$

where $M(t)$ is the motion modulation on the ideal RIPPG signal. The goal of the color differencing operation is to reduce the motion artifacts by the weighted subtraction of one RIPPG signal from another RIPPG signal in different color channels. This motion reduction operation is described as,

$$\begin{aligned} D(t) &= \frac{I_i(t)}{\alpha_i \beta_i} - \frac{I_j(t)}{\alpha_j \beta_j} \\ &= (\gamma_i - \gamma_j) \ S_0 \ \text{Pulse}(t) M(t), \end{aligned} \tag{6.4}$$

where $i \neq j$, and $i, \ j \in$ [Red, Green, Blue]. The motion-modulated common terms $S_0 M(t)$ and $R_0 M(t)$ are removed and thus the remainder is $\text{Pulse}(t)M(t)$. The motion related term $M(t)$ is still present. Since the facial ROI tracking algorithm is performed the before the color differencing operation, the motion residual in Eqn. Equation (6.4) is expected to be small.

To achieve the maximum pulse signal sensitivity, the i and j are selected by maintaining a large value of $\gamma_i - \gamma_j$. The wavelengths of red light are 620 to 750 nm, the wavelengths of green light are from 495 to 570 nm, and the wavelengths of blue light are from 450 to 495 nm. Accordingly, $\gamma_G > \gamma_B > \gamma_R$ in Fig. Figure 6.6. Therefore, the green and red channels are used in the color differencing operation. Before applying Eqn. Equation (6.4), the raw RIPPG signal is passed through a bandpass filter with frequency ranges $0.7 - 4$Hz in order to locate the heartbeat

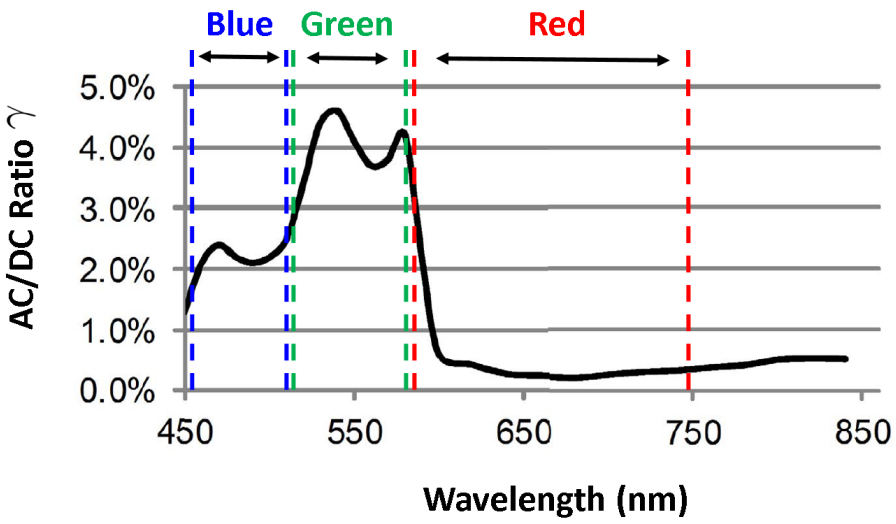


Figure 6.6: Wavelength dependence of the AC/DC ratio γ in contact PPG signal. The ratio of the RGB lights follows $\gamma_{\mathrm{G}} > \gamma_{\mathrm{B}} > \gamma_{\mathrm{R}}$.

frequency component. The weights for the filtered green and red channels can be estimated as,

$$\hat{\alpha}_G \hat{\beta}_G = \frac{I_G(t)}{\sqrt{\mathrm{RIPPG}_{BP}(t)}} \tag{6.5}$$

$$\hat{\alpha}_R \hat{\beta}_R = \frac{I_R(t)}{\sqrt{\mathrm{RIPPG}_{BP}(t)}}, \tag{6.6}$$

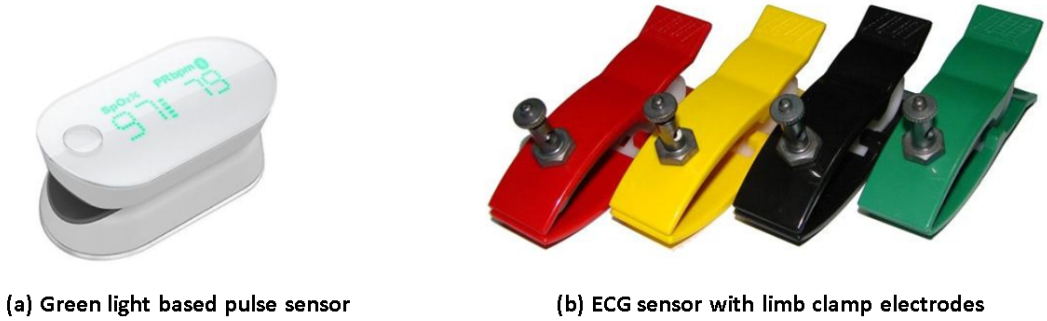
where RIPPG_{BP} denotes the bandpass-filtered spatial-averaged RIPPG signal. The green-red difference signal (GRD) is obtained,

$$\begin{aligned} \mathrm{GRD}(t) &= \frac{I_G(t)}{\hat{\alpha}_G \hat{\beta}_G} - \frac{I_R(t)}{\hat{\alpha}_R \hat{\beta}_R} \\ &= \left(\hat{\gamma}_G - \hat{\gamma}_R\right)\, S_0\, \mathrm{Pulse}(t)\, M_{BP}(t), \end{aligned} \tag{6.7}$$

where $M_{BP}(t)$ is the filtered motion residual.

6.3 Standard Reference Devices

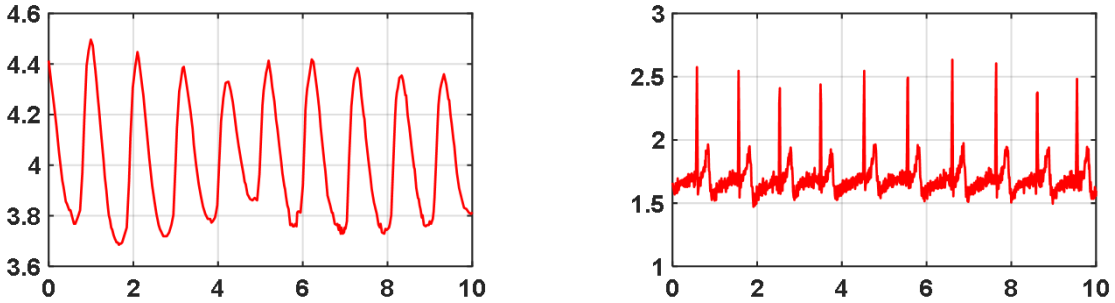
In the experimental studies, various reference devices are used to provide an accurate reference signal. Two of the most useful devices are pulse sensor and ECG



(a) Green light based pulse sensor

(b) ECG sensor with limb clamp electrodes

Figure 6.7: Example of standard reference devices in the experiment



(a) Captured pulse waveform for 10-s

(b) Captured ECG waveform for 10-s

Figure 6.8: Example pulse waveforms from the standard reference devices in Fig. Figure 6.7

sensor as shown in Fig. Figure 6.7. They can both provide the pulse waveform as shown in Fig. Figure 6.8. The ECG sensor however provides more details about the overall rhythm of cardiac activity.

Chapter 7

RESEARCH HIGHLIGHT: HEART-RATE DETECTION/MONITORING PERFORMANCE DEMONSTRATION

In this chapter, extensive examples are provided to validate the proposed theory and the proposed heart-rate estimation algorithm. For performance demonstration, a time-frequency (2-D) analysis is considered in addition to the conventional spectral (1-D) analysis since vital signs signals are a time-varying process. Two experimental scenarios are considered: controlled motorized vital signs simulator and human subjects as shown in Fig. Figure 7.1. First, vital signs detection performance using direct RF signal Eqn. (Equation (3.3)), IQ data Eqn. (Equation (3.4)) and (Equation (3.12)), and phase information Eqn. (Equation (3.17)) are demonstrated. Second, time-frequency waterfall plots from popular algorithms CSD, AD, Log and DACM methods are compared. The accuracy of the proposed heart-rate estimation algorithm is demonstrated by comparing against the reference pulse signal.

7.1 A Comparative Study

7.1.1 1-D Spectral Analysis

In Chapter Chapter 3, the vital signs are shown to be extracted in different data formats: direct RF signal in Eqn. (Equation (3.3)), two types of complex-baseband signals in Eqn. (Equation (3.4)) and (Equation (3.12)), and phase information in Eqn. (Equation (3.17)). These results are demonstrated with experimental examples from (a) vital signs simulator and (b) human subject. The vital signs simulator is built with two DC motor with a control circuit for speed management. Two metal balls are attached to two circulating platforms driven by motors as shown in Fig.

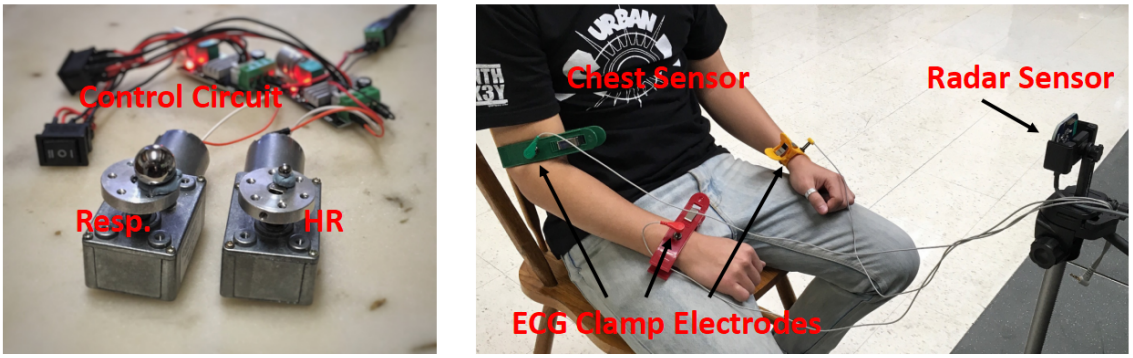


Figure 7.1

Figure 7.1(a). The larger metal ball about 2.5 cm is used to represent the chest movement and the smaller metal ball about 2 mm is used to represent the heartbeat motion. The following results are generated from a 20-s data set. Five different approaches are presented, in which RF denotes the results from Eqn. (Equation (3.3)), Magnitude denotes the results of absolute value of the complex-baseband signal in Eqn. (Equation (3.4)), CSD_1 and CSD_2 denote the results from Eqn. (Equation (3.4)) and (Equation (3.12)), and the phase-based method is implemented using Actangent method with DC-offset calibration.

Results from the controlled vital signs simulator are shown in Fig. Figure 7.2. The motorized circulating frequencies are set to 26 BPM and 58 BPM corresponding to the respiration rate and heart-rate. In this representative example, all five methods are able to identify the respiration frequency and the heartbeat frequency in the first five spectral plots. In the RF spectrum, the heartbeat signal is competing with the 2^{nd}-order harmonic of respiration. In the Magnitude spectrum, the heartbeat signal is the dominant component compared to the respiration harmonics. In the CSD_1 and CSD_2 spectrum results, the 2^{nd}-order harmonic of respiration is stronger than

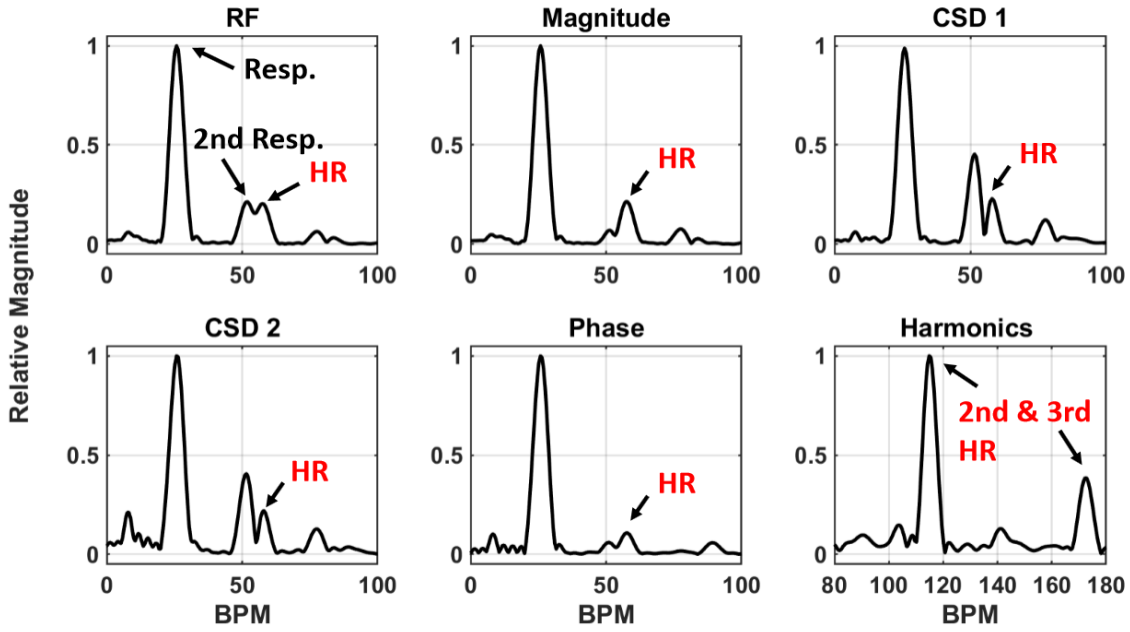


Figure 7.2: 1-D spectral analysis: controlled motorized vital signs simulator. Predefined heart-rate: 58 BPM, respiration rate: 26 BPM.

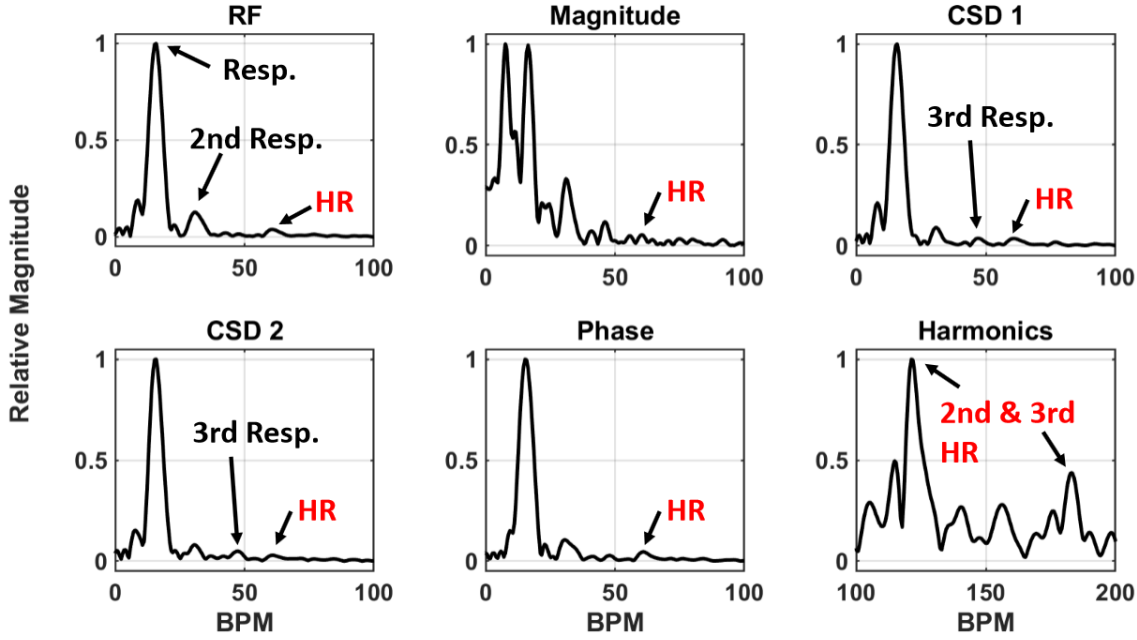


Figure 7.3: 1-D spectral analysis: stationary human subject seated 0.8 meters away.

the heartbeat signal. The heartbeat signal is thus very difficult to isolate. However, phase-based method suppresses the respiration harmonics significantly and provides better identifiability for heartbeat. For our proposed approach, at the heartbeat harmonics frequency region, the 2^{nd}-order and even the 3^{rd}-order harmonics are very distinct as if there is no interference from the respiration and thus correct heart-rate can be obtained.

Results from human subject are illustrated in Fig. Figure 7.3. With the help of external reference and human eye visualization, vital signs are identified in the first five spectrum plots. RF and phase-based methods generate similar spectrum and the heartbeat spectrum can be easily identified since the respiration harmonics are far away from the heartbeat spectrum. CSD_1 and CSD_2 generate similar spectrum but the heartbeat detection performance is worse than the previous two methods. Since an extra 3^{rd}-order harmonic of respiration is present in CSD_1 and CSD_2 spectrum, it leads to possible ambiguity to select the right spectrum peak. The worst detection performance goes to the Magnitude spectrum. There is a potential peak at the reference heartbeat location but the overall spectrum is very noisy to provide any confidant heat-rate estimate. On the contrary, for the proposed method, two dominant peaks are present in the heartbeat harmonics spectrum, corresponding to the 2^{nd}- and 3^{rd}-order harmonics. Therefore, the heart-rate can be accurately estimated with the help of the corresponding higher-order harmonics even though the lower frequency region is noisy.

To show the performance of the phase calibration process, the spectrum results before and after DC-offset calibration are shown in Fig. Figure 7.4 and Figure 7.5. The result of Fig. Figure 7.4 is from the vital signs simulator and Fig. Figure 7.5 is from human subject. It is clearly that a more correct spectrum is revealed after the calibration as shown in Fig. Figure 7.4, in which the 2^{nd}-order harmonic of the respi-

ration is significantly suppressed. In Fig. Figure 7.5, before calibration the spectrum near the heartbeat frequency is very noisy and there are many spurious peaks nearby the true heartbeat peak. While, after the phase calibration, the overall spectrum of interest is less noisy and a more meaningful observation can be made. Now there are four dominant spectral peaks in the plot. They are from the fundamental respiration and its 2^{nd}- and 3^{rd}-order harmonics, and the distinct heartbeat peak to the right side of the plot. Often, the phase calibration might not provide improved performance in terms of heartbeat detection as shown in Fig. Figure 7.6. This observation is consistent with the experimental results in references [78, 101]. The time domain sequence or the respiration pattern for generating Fig. Figure 7.6 is shown in Fig. Figure 7.7. The problem is to determine which of these data points need to be corrected at every processing window. Ideally, the data points corresponding to the same micro-motion, meaning that they belong to the same phase trajectory in the I/Q constellation plot as seen in Fig. Figure 3.1, should be corrected every time. In reality, the respiratory activity, the stronger motion in the vital signs, can be quite different from breath to breath as seen in Fig. Figure 7.7 and thus the calibration should be performed on similar respiration pattern. An automatically approach should be developed to perform this task.

7.1.2 2-D Time-Frequency Analysis

In Chapter Chapter 3, the existing popular heart-rate estimation algorithms are reviewed. Here a time-frequency (2-D) analysis using waterfall plots is considered Instead of the conventional 1-D spectrum analysis. Essentially, the respiration and heartbeat activities are slowly time-varying processes even for stationary subject. The following results are generated from a 60-s data set with 20-s processing window and 1 sample increment each processing time. Again, the results from controlled simulator

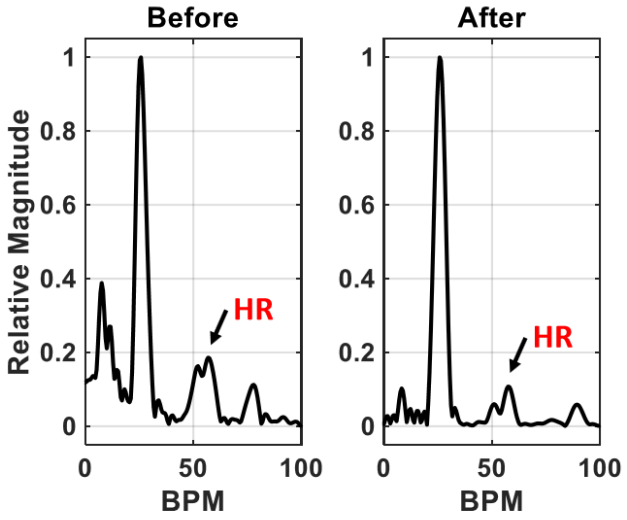


Figure 7.4: Phase calibration result: simulator.

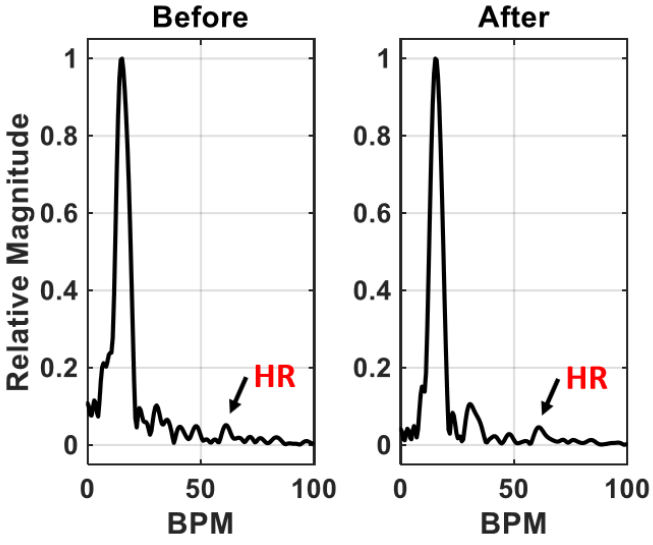


Figure 7.5: Phase calibration result: human subject example 1.

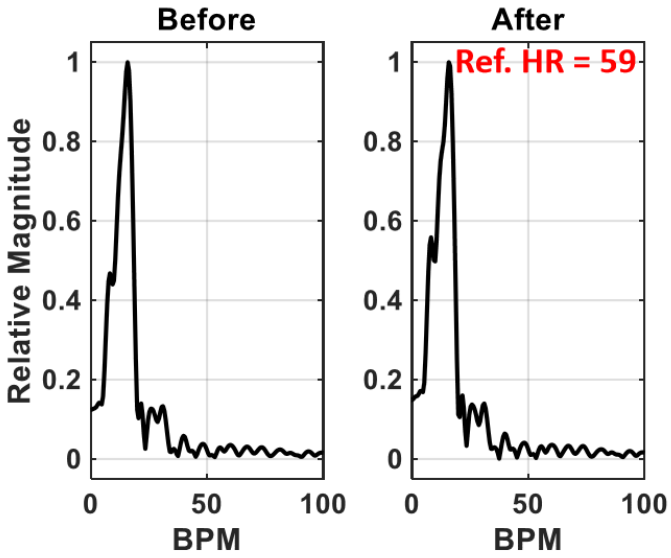


Figure 7.6: Phase calibration result: human subject example 2.



Figure 7.7: Irregular respiration pattern in data for generating Fig. Figure 7.6

and the results from human subject are shown. In Fig. Figure 7.8, the respiration rate and heart-rate over time are traced using CSD, AD, Log, DACM, SSM and MUSIC methods. CSD result is generated using Eqn. (Equation (3.4)). Based on the pre-defined respiration and heartbeat rates, all the significant spectral energies can be identified and associated. In the CSD waterfall plot, there are four significant spectral energies, corresponding to the respiration and its higher-order harmonics, and the heartbeat. The spectral location of the 2^{nd}-order harmonic of respiration is close to that of the heartbeat. Besides, the 2^{nd}-order harmonic of respiration has stronger energy than the heartbeat signal, making it very difficult to identify

and isolate the heartbeat signal. The effectiveness of the DC-correction is observed in the AD, Log, DACM, SSM and MUSIC waterfall plots. These five algorithms have similar results since they all operate on the corrected phase signal. After DC-correction, the respiration related harmonics are suppressed significantly, and the fundamental heartbeat and the intermodulation between the 2^{nd}-order harmonic of the heartbeat and the respiration $(2f_h - f_b)$ are better revealed. Among the five algorithms, the MUSIC approach has finer spectral resolution as expected. For the proposed method, the higher-order harmonics 2^{nd} and 3^{rd} are clearly identifiable and therefore the heart-rate can be estimated correctly.

On the other hand, the results from human subject in Fig. Figure 7.9 show that when the spectrum is noisy around the fundamental heartbeat frequency, it becomes very difficult to isolate the heartbeat without any prior knowledge in the six subplots to the left. From the CSD to the MUSIC waterfall plots, the heartbeat evolution over time can be barely traced without the external pulse reference since the energy of the respiration harmonics spreads across spectrum of interest. It is not possible to isolate the heartbeat signal automatically. The advantage of tracing the higher-order harmonics of the heartbeat signal becomes obvious as demonstrated in the proposed harmonics waterfall plot. In the heartbeat harmonics frequency region, the 2^{nd}-order harmonic has the most significant spectrum energy over time and therefore is easily identified.

Another typical experimental example is illustrated in Fig. Figure 7.10. The evolution of the heart-rate is clearly observable in all the existing algorithms. The heartbeat signal can be easily separated by a bandpass filter since the respiration energy and its harmonics are limited to a low frequency region relatively far way from the heartbeat frequency region. Similarly, the corresponding 2^{nd}-harmonic of the heartbeat is visible in the harmonics waterfall plot.

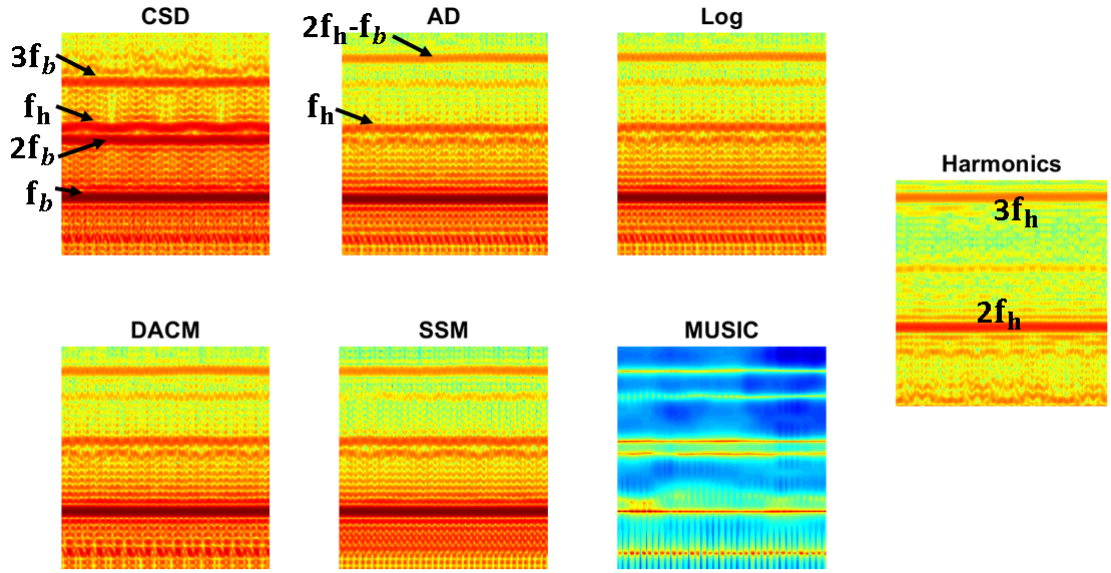


Figure 7.8: Time-frequency analysis waterfall plots from vital signs simulator. X axis denotes time scale in 40-second interval; y axis denotes frequency scale in BPM.

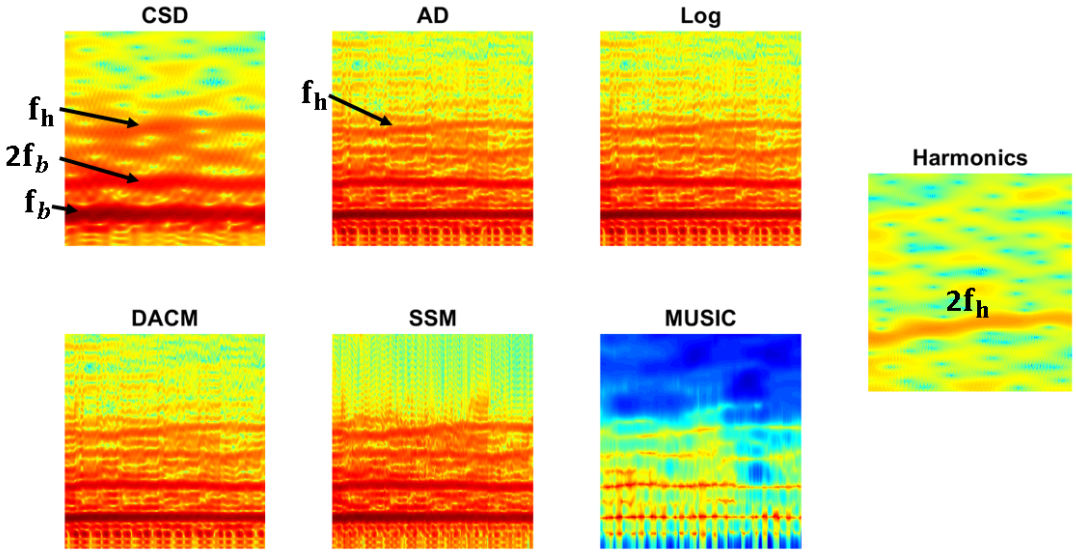


Figure 7.9: Time-frequency analysis waterfall plots from human subject 1. X axis denotes time scale in 40-second interval; y axis denotes frequency scale in BPM.

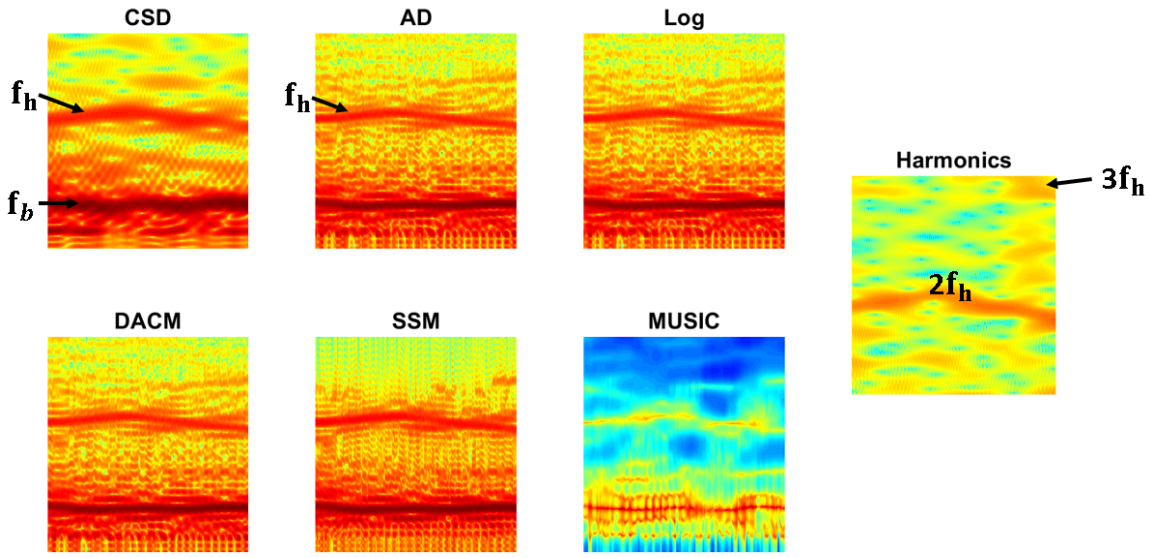


Figure 7.10: Time-frequency analysis waterfall plots from human subject 2. X axis denotes time scale in 40-second interval; y axis denotes frequency scale in BPM.

7.2 Continuous Heart-Rate Monitoring Performance

7.2.1 Single Subject

In this section, the continuous heart-rate monitoring performance of the proposed algorithm is demonstrated. The analysis in Section Section 7.1.1 and Section 7.1.2 is from the post-processing perspective and thus the estimates are obtained with the help of visualization and external pulse reference. It should be noted that phased-based methods are not fast enough for real-time processing due to an iterative phase calibration process. For comparison purpose, two 2-minute datasets are recorded and processed off-line. Three algorithms: the conventional CSD method, AD method and harmonics-based methods are compared. The proposed algorithm is implemented following Table Table 4.3.

In Fig. Figure 7.11 and Figure 7.12, the heart-rate monitoring results from the

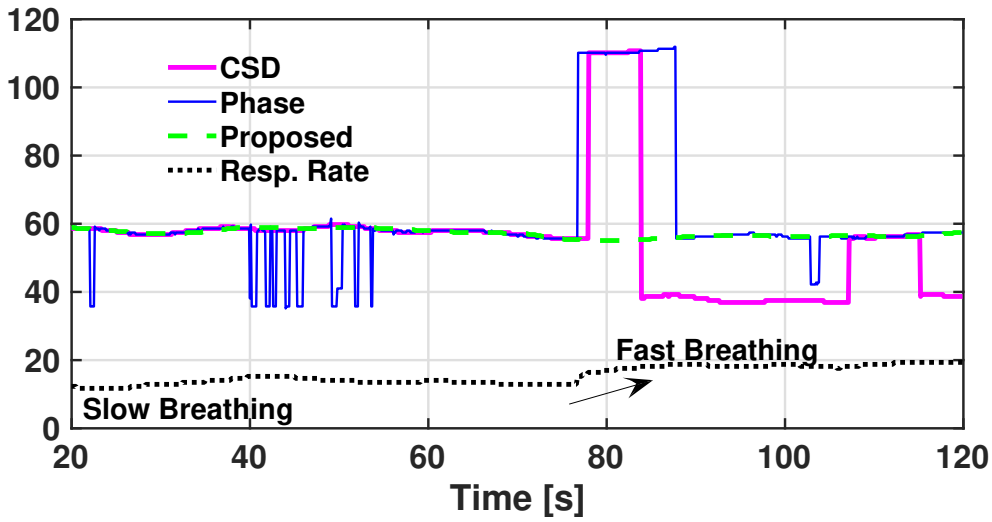


Figure 7.11: Continuous heart-rate monitoring performance of different algorithms.

human subjects are shown. In Fig. Figure 7.11, the continuous heart-rate monitoring performance of the proposed method and other popular algorithms are compared. The proposed method provides stable estimates, which gradually changes with time. While the results from the other two methods experience huge deviations, which are not physically possible for stationary subject. Heart-rate variation within a few beats is expected. To be more specific, from 20-s to 78-s, the CSD method has similar performance as that of the proposed method. That's because the respiration rate is relative low at about 14 BPM and the heart-rate is about 58 BPM. The 2^{nd}- and 3^{rd}-order harmonics of the respiration is relatively far away from the fundamental heartbeat frequency. Therefore, a bandpass filter is able to separate the heartbeat and attenuate these respiration harmonics. From about 78-s to 85-s, the human subject starts increasing the respiratory activity to 19 BPM and maintains at this level until the recording completes. Now the 2^{nd}-order harmonic of respiration is getting closer to the fundamental heartbeat frequency and the 3^{rd}-order harmonic is almost colocated with fundamental heartbeat frequency. At the respiration acceleration stage (78-s to

85-s), the spectral region near the fundamental heartbeat frequency becomes noisy, and the fundamental heartbeat frequency peak fades away. The 2nd-order harmonic of heartbeat is the dominant frequency component and therefore the estimate of the CSD method jumps to about 110 BPM. Once the respiration rate is stable (after 85-s), the spectrum at the relatively lower frequency region becomes less noisy. The 2nd-order harmonic of respiration dominants the spectrum even after the bandpass filter since usually respiration and its harmonics are much stronger than the heartbeat. As a result, the estimate jumps to the 2nd-order harmonic of respiration at about 38 BPM. Similar jumps of heart-rate estimate occur at 115-s for the same reasoning. The phase-based method (AD) performs poorly compared to the other two methods. On top of the overall trend of heart-rate, there are lots of fluctuations from the phase-based method. This is an important result, showing that the phased-based method cannot provide consistent estimates. This undesirable result is due to the fact that there is no prior knowledge about which of the I/Q data points need to be corrected. The precise phase calibration procedure is still unknown. Here the phase calibration is performed on a sliding window of 20-s data and it occasionally introduces phase distortion in the spectrum. That's why the heart-rate estimate from the phase-based method (solid blue curve) fluctuates wildly as seen in Fig. Figure 7.11.

In Fig. Figure 7.12, the accuracy of the proposed heart-rate monitoring algorithm is highlighted by comparing against the gold standard reference ECG sensor. The heart-rate estimates is gradually varying over time. The accuracy is well within 2% error interval about (+/-) 1.1 beats from 20-s to 120-s in dataset 2.

7.2.2 Multiple Subjects

In this section, the continuous vital signs monitoring performance of multiple subjects is demonstrated. The experiment setup is shown in Fig. Figure 7.13. Two

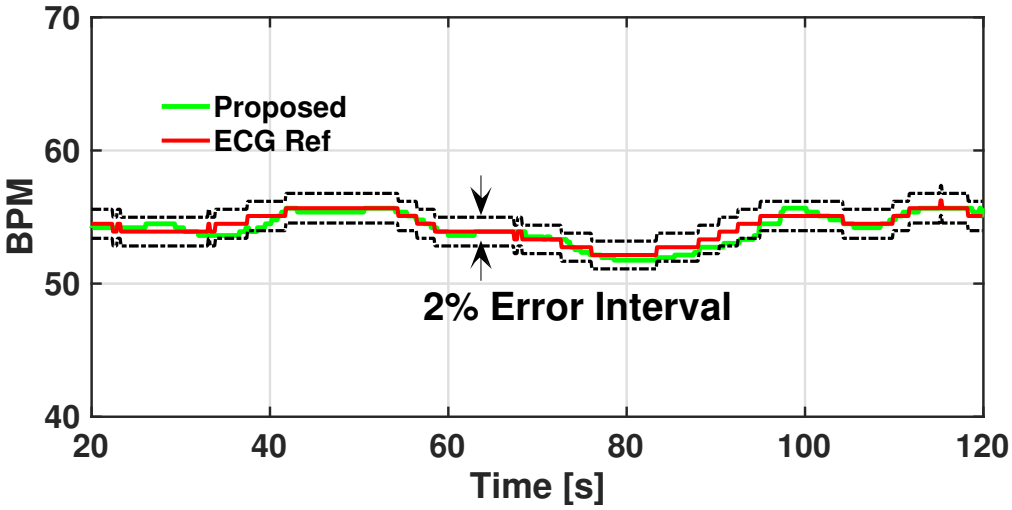


Figure 7.12: Accuracy demonstration

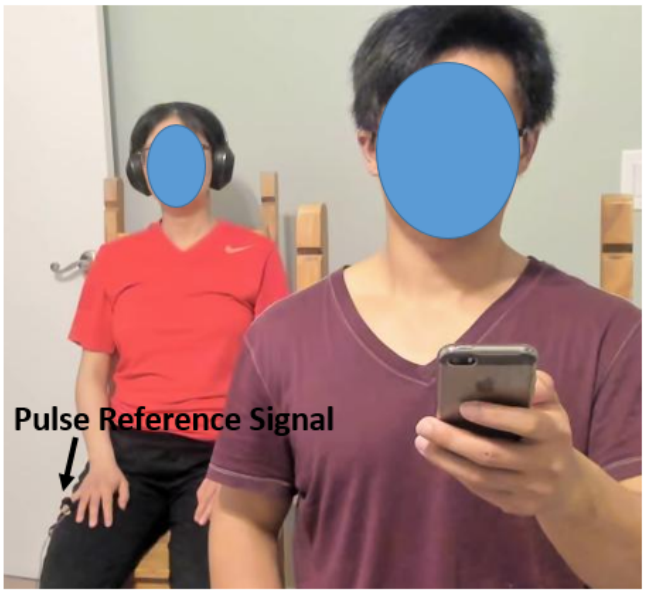


Figure 7.13: Two subject heart-rate monitoring setup

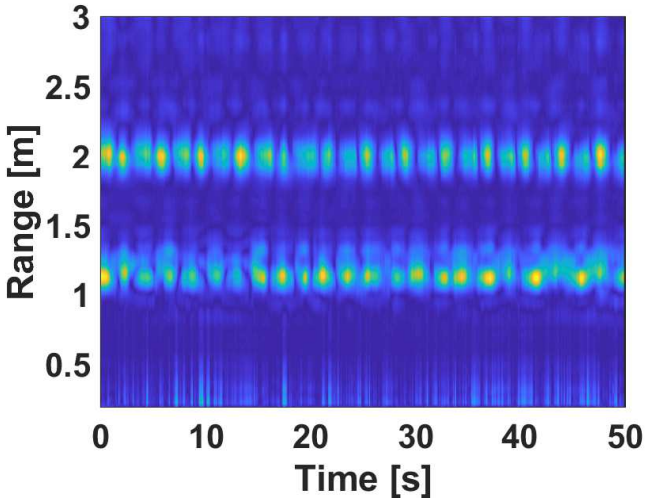


Figure 7.14: Two subject heart-rate monitoring: signal after static background removed

subjects are present. One subject constantly uses the cellphone and breathes normally while the other subject is asked to perform the same task but listen to music during the experiment. For comparison, a RIPPG system using a webcam is used simultaneously to record the scene and extract the pulse information. A pulse reference sensor is used on one of the subjects (subject in red) to demonstrate the accuracy of the radar system performance. In Fig. Figure 7.14, the spatial-temporal representation of the signal is provided. Subject 1 is located about 2 meters and subject 2 is about 1.2 meters away from the radar sensor.

First, a snapshot of the vital signs spectra from different measurement systems is shown, the radar system, the RIPPG system, and the contact-based pulse reference system. In Fig. Figure 7.15 and Figure 7.16, the 2^{nd}-order heartbeat spectra from the two subjects from the radar system are compared with the fundamental heartbeat spectra extracted from the RIPPG system. The recovered heart-rate estimates from the radar system match the spectrum peak locations from the imaging system. The

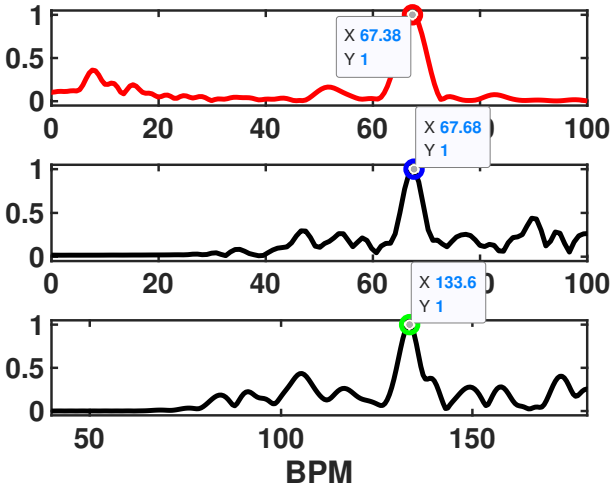


Figure 7.15: Spectra comparison of subject 1 from various systems. From the top to the bottom plots are the reference system, the camera system, and the radar system.

radar estimate is also consistent with the pulse reference for human subject 1.

In Fig. Figure 7.17 and Figure 7.18, the heart-rate evolutions of the two subjects from the proposed radar system are shown side by side with these from the imaging system. Heart-rate results from both systems align with each other. The radar heart-rate estimates for subject 1 are consistent with the pulse reference signal. The absolute error is within a 2% error interval of the pulse reference. For subject 2, the heart-rate estimates from the radar system and the camera system only differ by a fraction of beat.

7.3 Comparison With Existing Remote Sensing Technology

The continuous heart-rate monitoring performance between the radar-based system implemented using the proposed signal processing technique and the camera-based system are compared in order to further validate the proposed radar technology. As pointed in previous chapters, the remote PPG system such as camera can be

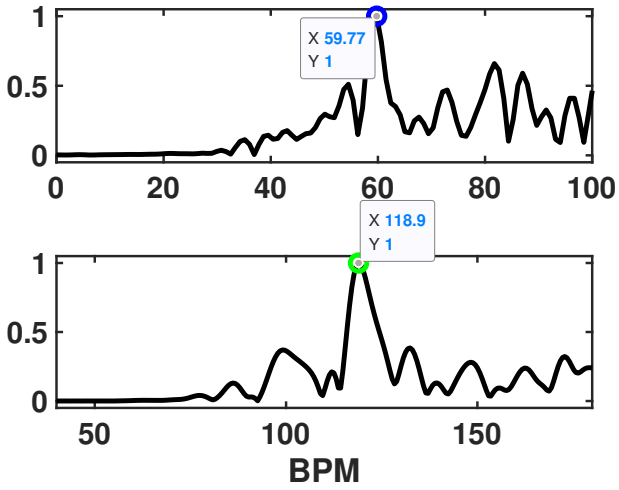


Figure 7.16: Spectra comparison of subject 2 from various systems. From the upper to the lower plots are the camera system and the radar system.

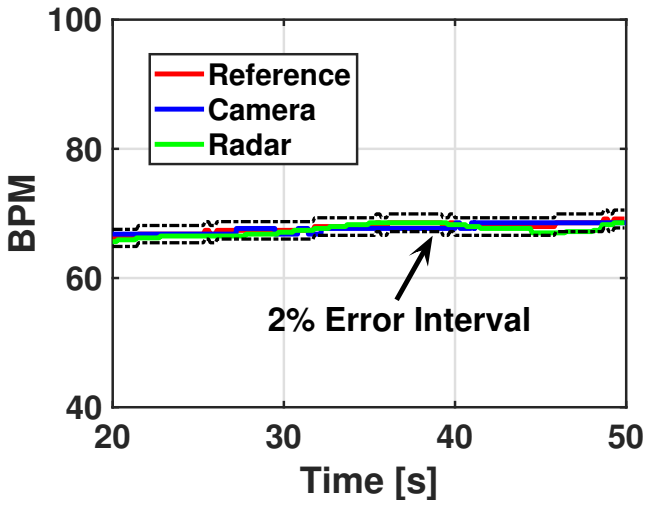


Figure 7.17: Heart-rate estimation accuracy demonstration of subject 1

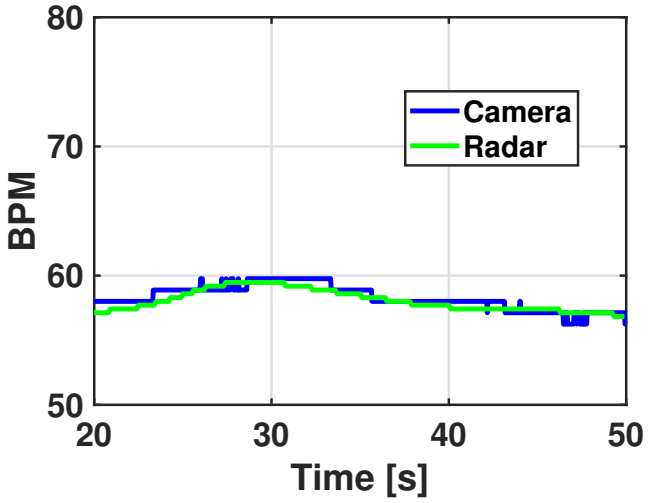


Figure 7.18: Heart-rate monitoring demonstration of subject 2

used as as benchmark for heart-rate monitoring since there is almost no respiration-interference.

In Fig. Figure 7.19, the proposed signal processing technique enables continuous heart-rate monitoring using radar technology because the 2^{nd}-order harmonic of heartbeat is almost respiration-interference free. While the conventional approach cannot achieve consistent heart-rate estimates as seen in the figure such that CSD method is consistently underestimating the heart-rate due to the interference from the 3^{rd}-order harmonic of respiration.

In Fig. Figure 7.20, the radar measurement can accurately estimate the heart-rate during the entire recording. The difference between the radar estimates and the reference are within only 1 beat. The reference heart-rate is obtained by processing the ECG signal using a 20-s processing window.

In Fig. Figure 7.21, the radar performance is compared to other remote sensing technology for vital signs monitoring. The heart-rate evolution from both the radar and the camera systems are consistent and the deviation is well within 1 beat.

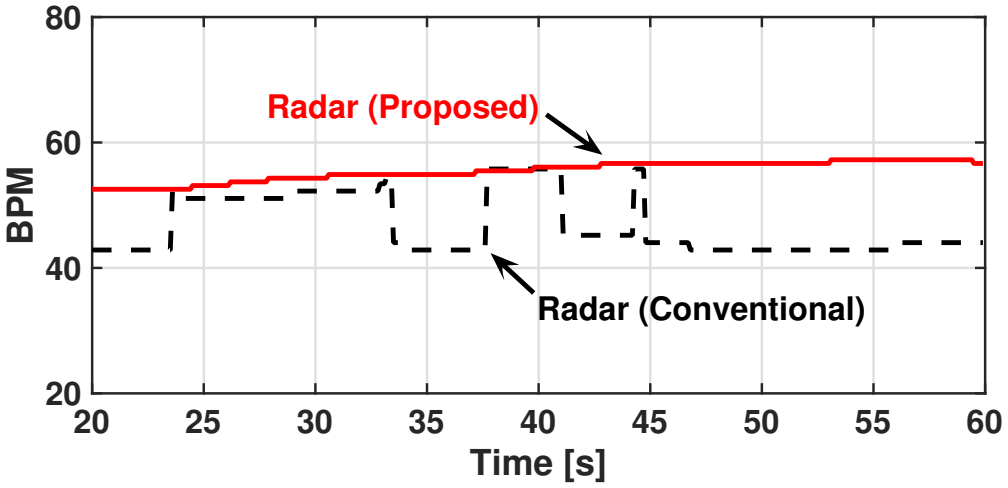


Figure 7.19: Radar performance demonstration: proposed method vs conventional CSD method

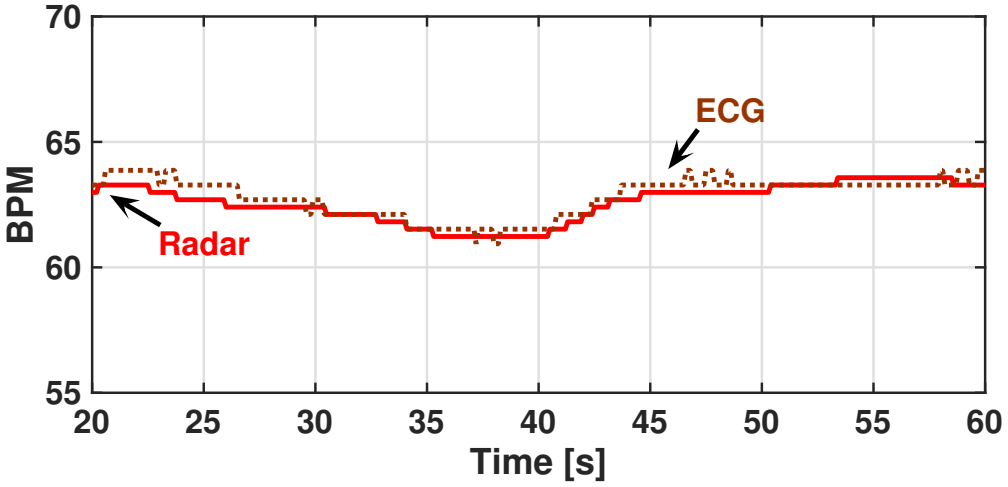


Figure 7.20: Radar performance against heart-rate extracted from the reference ECG signal

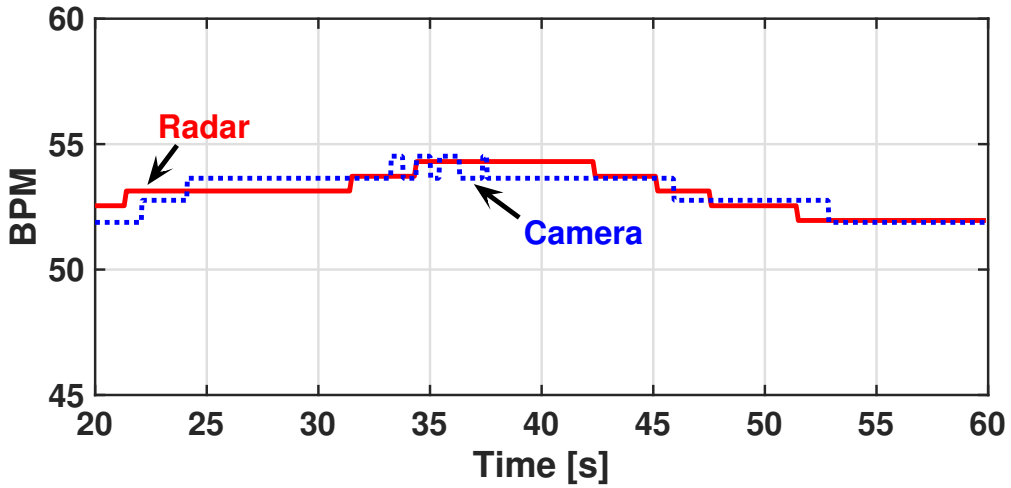


Figure 7.21: Radar performance compared with the camera-based system

7.4 Through Wall Heart-Rate Monitoring

In this section, a through wall multiple subjects vital signs monitoring algorithm is described. Information about the respiratory and heartbeat activities are extracted. Information about the respiratory activity includes the instantaneous waveform and the averaged performance, the number of beats per minute. As for the heartbeat activity, the averaged number of beats per minute or heart-rate is provided.

In the experiment setup, two human subjects are present in a normal office room. They are seated far apart at different distances to a radar sensor behind wall. The radar is about 0.4 meter to the wall. The test subjects are required to sit still and breath normally during the experiment.

In the processing stage, the received RF signals are stored. The small micro-motion due to vital signs is extracted by processing the slow-time samples in a row vector at the range of interest. First, the number of targets in this room is determined. This is done by analyzing the range-slow-time heatmap and the range-Doppler map after removing the static DC component. If there are two energy strips across the slow-

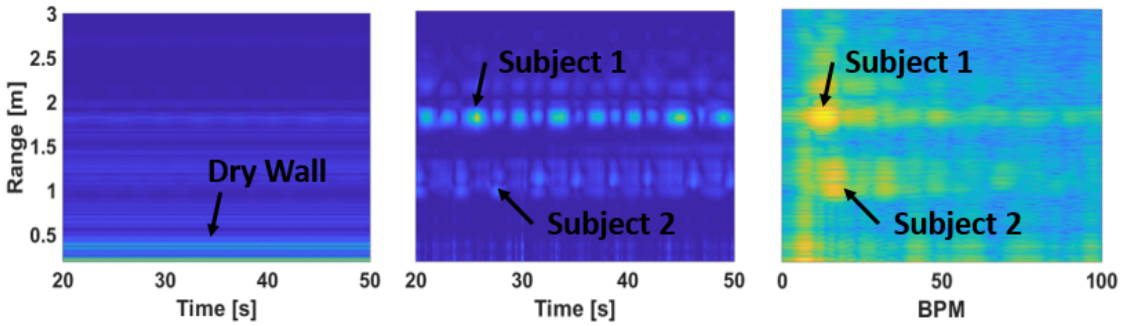


Figure 7.22: Two-dimensional analysis of vital signs monitoring. Left plot: the range-slow-time heatmap of the raw data. The strong energy reflection at about 0.4 meter is from a dry wall. Middle plot: the range-slow-time heatmap after removing the static background. Right plot: the corresponding range-Doppler map.

time in the range-slow-time heatmap, and at the same locations there are two distinct energy clusters at the normal respiration frequency region in the range-Doppler map, then the number of targets is two. An example of the range-slow-time heatmap and the range-Doppler plot in present of two test subjects are provided in Fig. Figure 7.22.

Once the number of targets is determined. The range bin for each target can be located. The slow-time variation of the RF signal at the selected range bin is a good approximation of the chest motion or respiration pattern.

As shown in Eqn. (Equation (3.7)), the vital signs information is preserved in the RF domain. Spectral analysis is applied at the of range bins containing most of the vital signs activity. Therefore, the respiration rate is estimated from the location of the dominant spectral peak, and the heart-rate is obtained from the proposed adaptive combination scheme. A high level signal processing diagram of the proposed algorithm is illustrated in Fig. Figure 7.23.

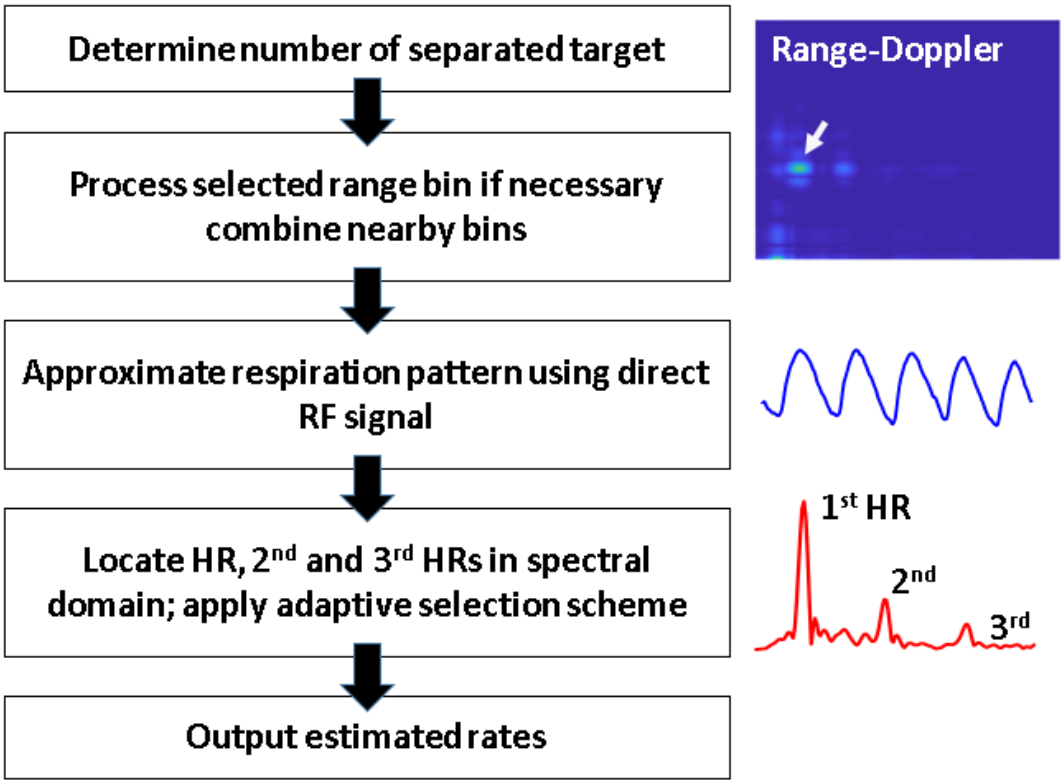


Figure 7.23: High-level processing diagram for through wall vital signs monitoring

7.4.1 Single Subject

In this example, the test subject is seated 1 meter away from the radar breathing normally with a dry wall in between. In Fig. Figure 7.24, the estimated heart-rate using the proposed method outperforms CSD method since CSD method cannot provide consistent heart-rate estimates over time. The evolution of respiration rate is provided as well.

In the second example, the though wall heart-rate monitoring performance is demonstrated by comparing to the ECG reference signal. In Fig. Figure 7.25, the spatial-temporal representation of the raw RF signal is provided. There is strong energy reflection up to 1 meter since the dry wall is located about 1 meter away from

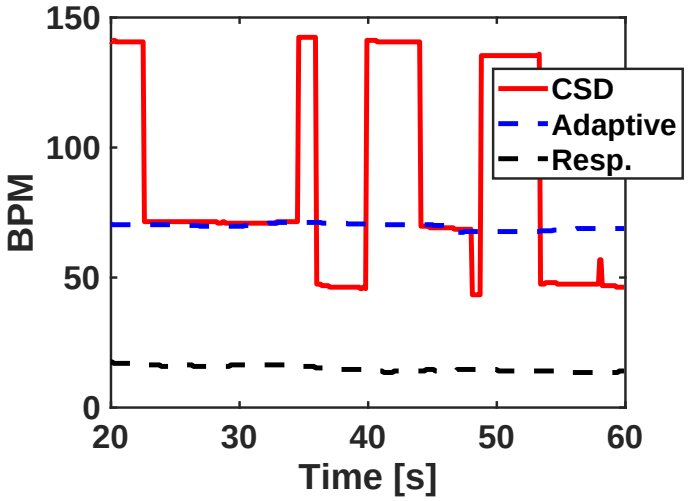


Figure 7.24: Through wall single subject monitoring performance against the CSD method

the radar. In Fig. Figure 7.26, the vital signs energy is clearly revealed after removing the static background. The human subject is about 1.5 meters away from the radar sensor. The accuracy of the proposed adaptive heart-rate monitoring algorithm is demonstrated in Fig. Figure 7.27. The heart-rate estimation error is within 3% error interval of the reference signal and the maximum error is less than 2 beats.

7.4.2 Multiple Subjects

In this multiple subjects scenario, a snapshot of range-slow-time heatmap and the range-Doppler map is shown in Fig. Figure 7.22. The traces of the energy reflection from the wall and two subjects are clearly visible. The absolute locations between the radar and the wall, and between the radar and each target match the true geometry of the experiment setup. In Fig. Figure 7.28, the vital signs of all subject including respiration rate and heart-rate are successfully extracted using the proposed method.

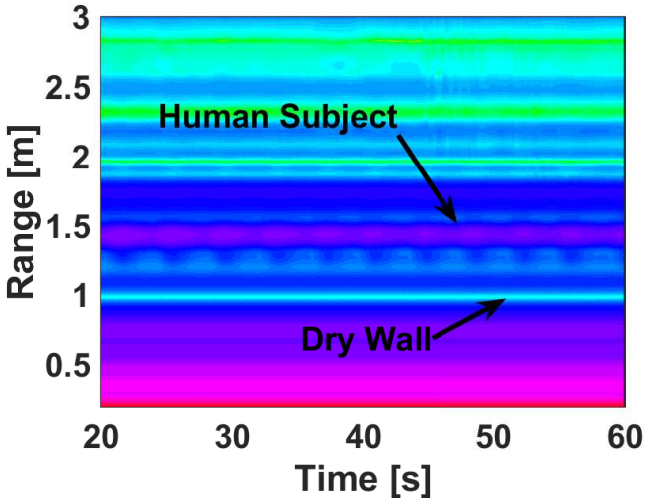


Figure 7.25: Raw RF signal

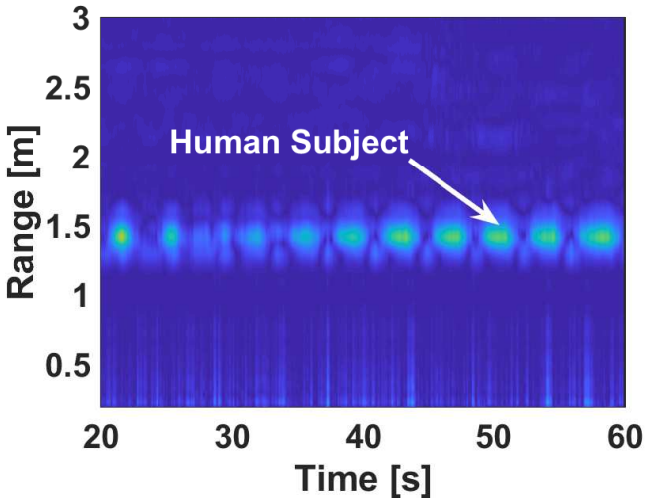


Figure 7.26: Signal after static background removed

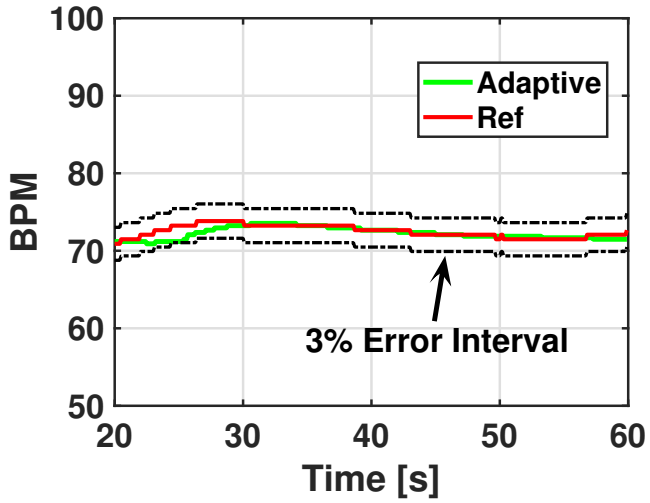


Figure 7.27: Through wall heart-rate monitoring performance against the ECG reference signal

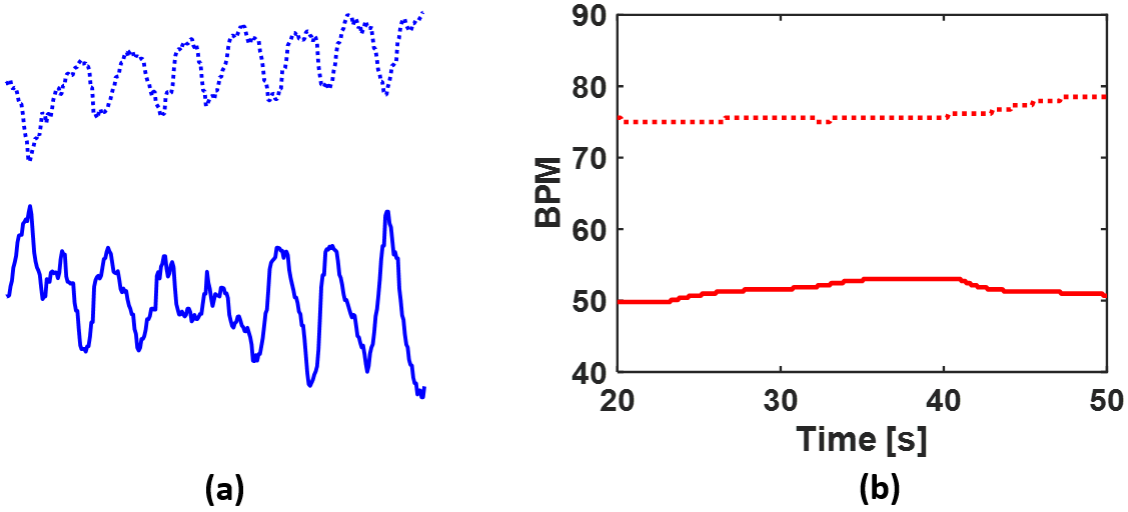


Figure 7.28: Through wall two subjects monitoring performance. (a) respiration patterns; (b) heart-rate evolutions.

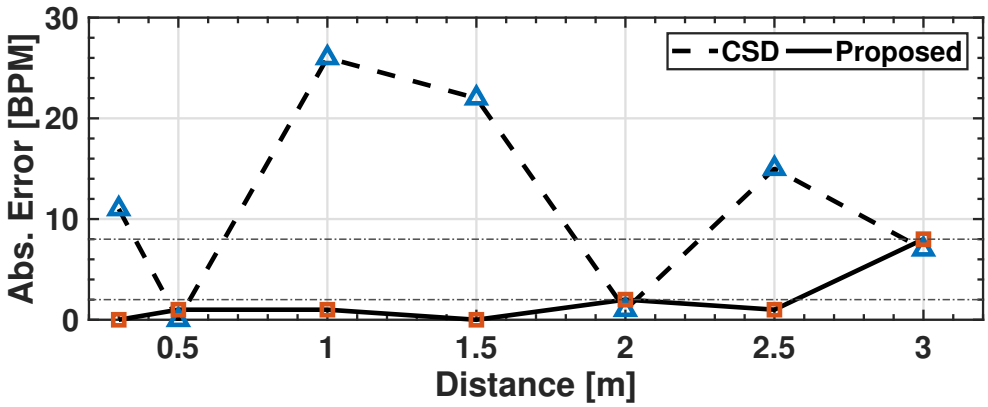


Figure 7.29: Heartbeat detection performance at different ranges.

7.5 Heart-Rate Detection Performance In Further Distances

In this section, experimental results are provided to show the heartbeat detection performance at different ranges in Fig. Figure 7.29. In this example, seven measurements are captured ranging from 0.3 to 3 meters. The proposed harmonics-based heart-rate estimation algorithm can correctly detect the heartbeat up to 2.5 meters with a maximum error 2 BPM at 2 meters. While the conventional CSD method does not provide consistent estimates and the large errors is due to strong respiration harmonics. These results are summarized in Table. Table 7.1.

7.6 Precise Phase Calibration Technique for Improved Heartbeat Detectability

In this section, three different types of analyses are considered to validate the proposed theory. First, the precise phase calibration procedure is compared to the conventional phase calibration method on simulated data. A realistic time-varying vital signs model is considered in order to mimic the respiration activity. Second, the proposed method is tested on a mechanic system as shown in Fig. Figure 7.1(a). Two motorized rotating systems are used to present chest motion and heartbeat, with pre-defined rotary frequencies. The purpose of this experiment is to show that the

Table 7.1: Summary: Performance (Unit in BPM) At Various Ranges

	CSD	Proposed	Reference
0.3 m	**70**	**59**	**59**
0.5 m	**56**	**57**	**56**
1 m	**37**	**62**	**63**
1.5 m	**35**	**57**	**57**
2 m	**60**	**63**	**61**
2.5 m	**45**	**59**	**60**
3 m	**70**	**55**	**63**

existing phase calibration method works in a controlled environment, in which the simulators have very regular motions and experience constant DC-offsets. However, in real situation, even for very relaxed and stationary human subject, the respiratory activity can be very irregular and the phase variation has a slowly time-varying DC-offset. This is especially true for continuous heart-rate monitoring. Finally, the experiment results on the human subject are highlighted. The proposed method outperforms the conventional method in terms of heartbeat detectability.

7.6.1 Computer Simulation

In Fig. **????**, the resulting vital signs spectra from different methods are shown. The proposed method (green curve) achieves similar result as a scenario (black curve), in which there is only constant DC-offset. To be more specific, all the unwanted harmonics are suppressed. Without considering the time-varying phase offset, the conventional phase calibration method cannot effectively suppress the respiration harmonics and intermodulations.

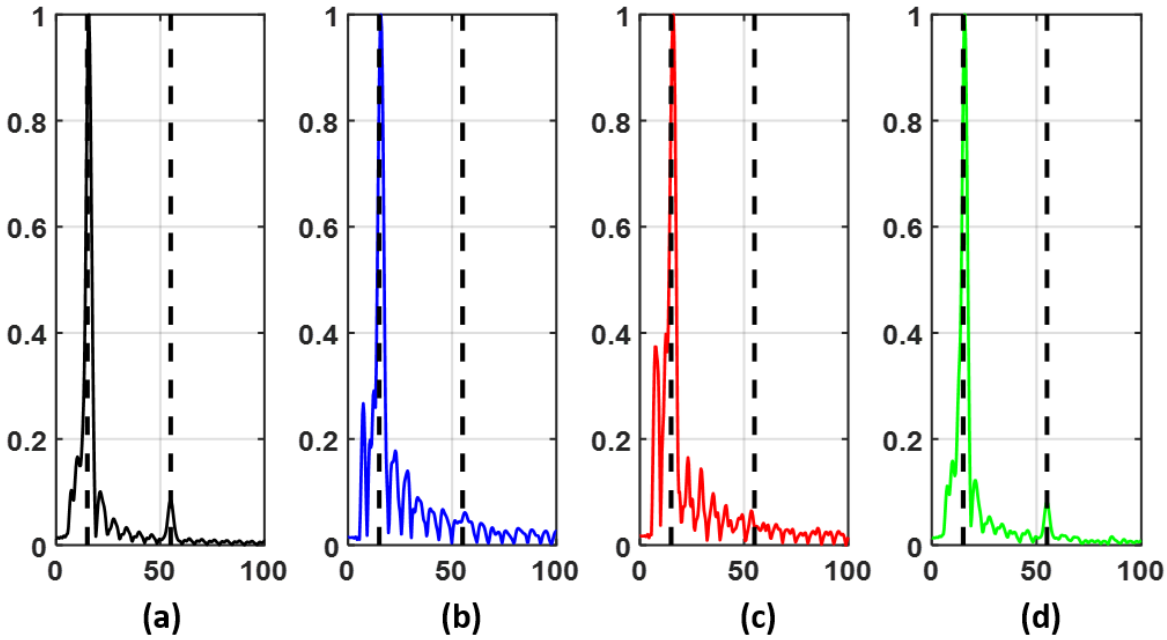


Figure 7.30: Respiration suppression performance demonstration: computer simulation. (a) Phase calibration results when constant DC-offset is applied; (b) CSD result assuming time-varying phase noise; (c) conventional phase calibration result assuming time-varying phase noise; (d) precise phase calibration result in present of time-varying phase noise. Dashed vertical lines denote the nominal respiratory rate and heart-rate.

7.6.2 Controlled Mechanic System

In Fig. **????**, the vital signs spectrum results from different methods are shown. The two methods, including the proposed method (green curve), and the conventional method (red curve), generate similar spectrum as expected since the mechanic system generates very regular motion pattern. In particular, the interferencing respiration related harmonics and intermodulation are significantly reduced and therefore the heartbeat spectrum peak is easily isolated. Besides, the CSD method (back curve) is used as a reference to show the original vital signs spectrum before phase calibration.

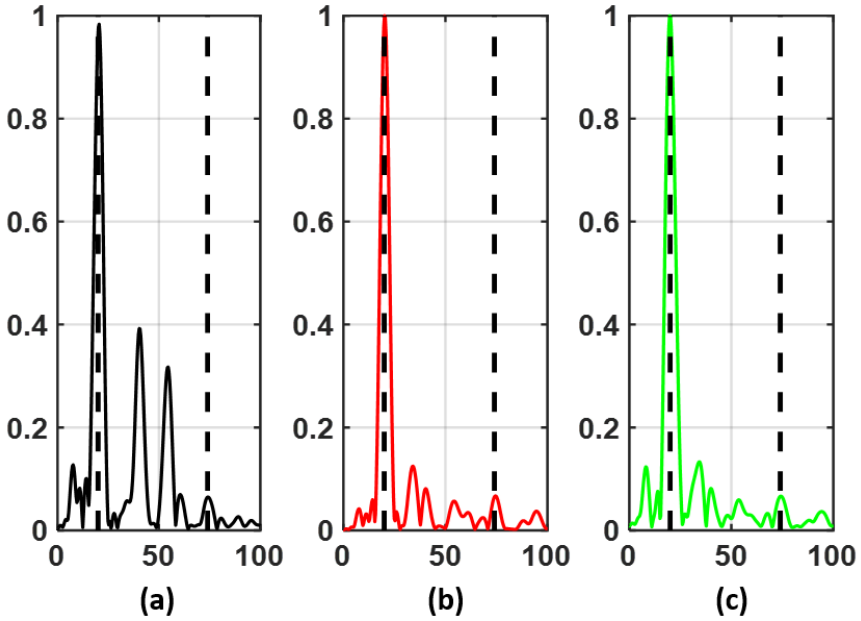


Figure 7.31: Respiration suppression performance demonstration: mechanic system. (a) CSD method; (b) conventional method; (c) precise phase calibration method. Dashed vertical lines denote the pre-defined respiratory rate and heart-rate.

7.6.3 Human Subject

In Fig. **????**, the continuous heart-rate monitoring performance from different methods is demonstrated. Additionally, the reconstructed respiration pattern (blue curve) is plotted on top of the hear-rate evolutions from the different methods. In particular, the proposed method (green curve) and the conventional method (red curve) accurately estimate the heart-rate when the respiration pattern is regular while the results from the conventional method fluctuates and the proposed method maintains the estimation accuracy when the respiration pattern is irregular. The proposed method also provides consistent and accurate heart-rate estimate during this recording by comparing against the reference ECG signal (magenta curve).

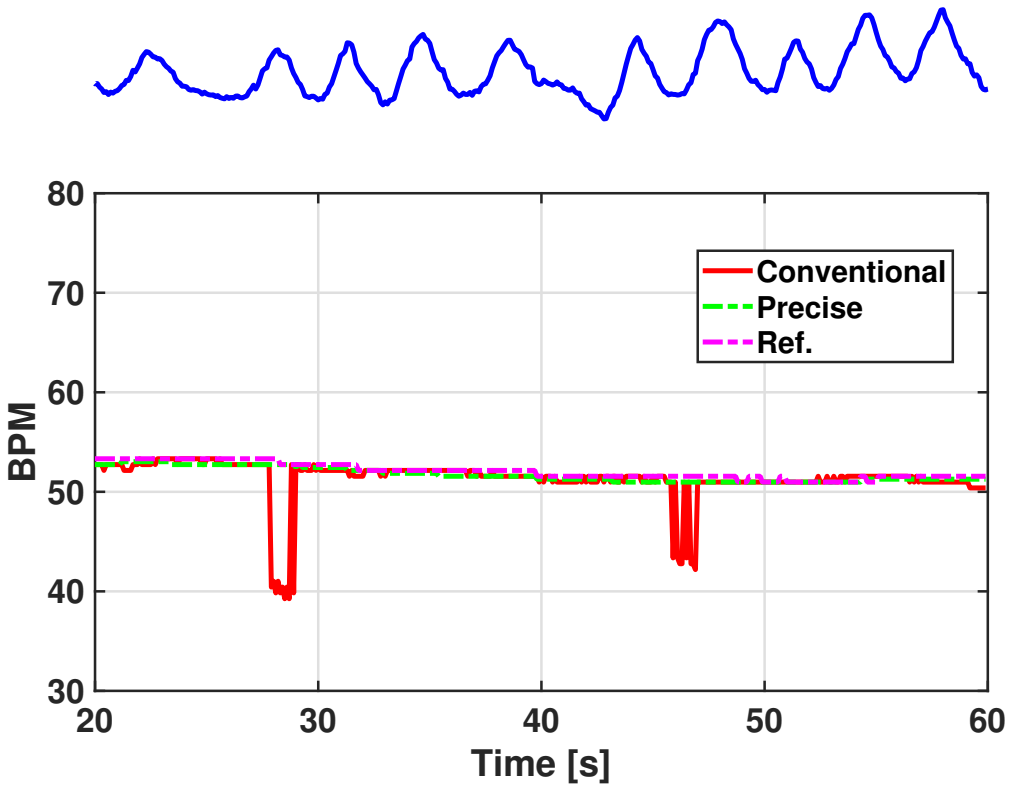


Figure 7.32: Heart-rate monitoring performance from different phase calibration methods. The upper plot and the lower plot are the extracted respiration pattern and the heart-rate evolutions from different methods.

Chapter 8

SUMMARY

The theory and implementation of remote vital signs monitoring radar system are presented in this thesis. The non-contact vital signs monitoring system provides heart-rate estimates and displays the reconstructed respiration pattern in real-time. A novel heart-rate monitoring algorithm based on a concept that estimates the fundamental heart-rate from its higher-order signatures in the spectral domain is presented. The performance is demonstrated in present of small-scale motion, multiple subjects and though wall. A precise phase calibration routine for dealing with time-varying phase noise is elaborated, simulated with realistic respiration model, tested on controlled mechanic system and human subject with non-controlled respiratory activity. The work presented in the thesis carries significant practical importance in development of next general personal health and life saving applications using advanced radar signal processing techniques.

REFERENCES

[1] D. W. Bliss and Y. Rong, "Effects of channel estimation errors on in-band full-duplex mimo radios using adaptive transmit spatial mitigation," in *Signals, Systems and Computers, 2013 Asilomar Conference on*. IEEE, 2013, pp. 9–13.

[2] ——, "Full-duplex self-interference mitigation performance in nonlinear channels," in *Signals, Systems and Computers, 2014 48th Asilomar Conference on*. IEEE, 2014, pp. 1696–1700.

[3] Y. Rong, S. Werth, and D. Bliss, "Source number detection performance of minimum redundancy and uniform linear arrays," in *Phased Array Systems and Technology, 2016 IEEE International Symposium on*, 2016.

[4] Y. Rong and D. W. Bliss, "Multiple source detection performance of linear sparse arrays," in *Signals, Systems and Computers, 2016 50th Asilomar Conference on*. IEEE, 2016, pp. 1513–1517.

[5] Y. Rong, A. A. Samuel, and D. W. Bliss, "Model order identification and parameters estimation using array processings for small sample support," in *Radar Conference (RadarConf), 2017 IEEE*. IEEE, 2017, pp. 1165–1169.

[6] Y. Rong and D. W. Bliss, "Underdetermined source number estimation based on complex wishart distribution using nested arrays," in *Military Communications Conference (MILCOM), MILCOM 2017-2017 IEEE*. IEEE, 2017, pp. 525–530.

[7] ——, "Model order and parameter estimation for underdetermined source scenarios using sparse arrays with filled co-arrays," *IEEE transactions on signal processing*, 2018.

[8] Y. Rong, A. R. Chiriyath, and D. W. Bliss, "Multiple-antenna multiple-access joint radar and communications systems performance bounds," in *2017 51st Asilomar Conference on Signals, Systems, and Computers*. IEEE, 2017, pp. 1296–1300.

[9] ——, "Mimo radar and communications spectrum sharing: A multiple-access perspective," in *2018 IEEE 10th Sensor Array and Multichannel Signal Processing Workshop (SAM)*. IEEE, 2018, pp. 272–276.

[10] R. M. Gutierrez, H. Yu, Y. Rong, and D. W. Bliss, "Time and frequency dispersion characteristics of the uas wireless channel in residential and mountainous desert terrains," in *Consumer Communications & Networking Conference (CCNC), 2017 14th IEEE Annual*. IEEE, 2017, pp. 516–521.

[11] A. Herschfelt, C. R. Birtcher, R. M. Gutierrez, Y. Rong, H. Yu, C. A. Balanis, and D. W. Bliss, "Consumer-grade drone radar cross-section and micro-doppler phenomenology," in *Radar Conference (RadarConf), 2017 IEEE*. IEEE, 2017, pp. 0981–0985.

[12] Y. Rong and D. W. Bliss, "Harmonics-based multiple heartbeat detection at equal distance using uwb impulse radar," *Radar Conference (RadarConf), IEEE*, 2018.

[13] ——, "Direct rf signal processing for heart-rate monitoring using uwb impulse radar," in *2018 Asilomar Conference on Signals, Systems and Computers,*. IEEE, 2018.

[14] ——, "Remote sensing for vital information based on spectrum-domain harmonic signatures," *IEEE Transactions on Aerospace and Electronic Systems*, 2018.

[15] ——, "Smart homes: See multiple-heartbeats through wall using wireless signals," in *Radar Conference (RadarConf), 2019 IEEE*. IEEE, 2019.

[16] ——, "Is radar cardiography (rcg) possible? – a radar approach," in *Radar Conference (RadarConf), 2019 IEEE*. IEEE, 2019.

[17] ——, "Precise phase calibration routine for spectral-based heartbeat detection using uwb impulse radar," *IEEE transactions on Biomedical Engineering*, 2019.

[18] K. Fox, J. S. Borer, A. J. Camm, N. Danchin, R. Ferrari, J. L. L. Sendon, P. G. Steg, J.-C. Tardif, L. Tavazzi, M. Tendera *et al.*, "Resting heart rate in cardiovascular disease," *Journal of the American College of Cardiology*, vol. 50, no. 9, pp. 823–830, 2007.

[19] F. P. Wieringa, F. Mastik, and A. F. van der Steen, "Contactless multiple wavelength photoplethysmographic imaging: a first step toward "spo 2 camera" technology," *Annals of biomedical engineering*, vol. 33, no. 8, pp. 1034–1041, 2005.

[20] K. Humphreys, T. Ward, and C. Markham, "Noncontact simultaneous dual wavelength photoplethysmography: a further step toward noncontact pulse oximetry," *Review of scientific instruments*, vol. 78, no. 4, p. 044304, 2007.

[21] C. Takano and Y. Ohta, "Heart rate measurement based on a time-lapse image," *Medical Engineering and Physics*, vol. 29, no. 8, pp. 853–857, 2007.

[22] J. Zheng, S. Hu, V. Chouliaras, and R. Summers, "Feasibility of imaging photoplethysmography," in *BioMedical Engineering and Informatics, 2008. BMEI 2008. International Conference on*, vol. 2. IEEE, 2008, pp. 72–75.

[23] W. Verkruysse, L. O. Svaasand, and J. S. Nelson, "Remote plethysmographic imaging using ambient light." *Optics express*, vol. 16, no. 26, pp. 21 434–21 445, 2008.

[24] M.-Z. Poh, D. J. McDuff, and R. W. Picard, "Non-contact, automated cardiac pulse measurements using video imaging and blind source separation." *Optics express*, vol. 18, no. 10, pp. 10 762–10 774, 2010.

[25] C. N. Paulson, J. T. Chang, C. E. Romero, J. Watson, F. J. Pearce, and N. Levin, "Ultra-wideband radar methods and techniques of medical sensing and imaging," in *Smart Medical and Biomedical Sensor Technology III*, vol. 6007. International Society for Optics and Photonics, 2005, p. 60070L.

[26] Y. Yang and A. E. Fathy, "See-through-wall imaging using ultra wideband short-pulse radar system," in *Antennas and Propagation Society International Symposium, 2005 IEEE*, vol. 3. IEEE, 2005, pp. 334–337.

[27] M. Chia, S. Leong, C. Sim, and K. Chan, "Through-wall uwb radar operating within fcc's mask for sensing heart beat and breathing rate," in *Radar Conference, 2005. EURAD 2005. European.* IEEE, 2005, pp. 267–270.

[28] R. M. Narayanan, "Through-wall radar imaging using uwb noise waveforms," *Journal of the Franklin Institute*, vol. 345, no. 6, pp. 659–678, 2008.

[29] S. Hantscher, A. Reisenzahn, and C. G. Diskus, "Through-wall imaging with a 3-d uwb sar algorithm," *IEEE Signal Processing Letters*, vol. 15, pp. 269–272, 2008.

[30] L. Jofre, A. Broquetas, J. Romeu, S. Blanch, A. P. Toda, X. Fabregas, and A. Cardama, "Uwb tomographic radar imaging of penetrable and impenetrable objects," *Proceedings of the IEEE*, vol. 97, no. 2, pp. 451–464, 2009.

[31] M. Klemm, I. Craddock, J. Leendertz, A. Preece, D. Gibbins, M. Shere, and R. Benjamin, "Clinical trials of a uwb imaging radar for breast cancer," in *Antennas and Propagation (EuCAP), 2010 Proceedings of the Fourth European Conference on.* IEEE, 2010, pp. 1–4.

[32] L. A. Shepp and J. Kruskal, "Computerized tomography: the new medical x-ray technology," *The American Mathematical Monthly*, vol. 85, no. 6, pp. 420–439, 1978.

[33] F. Arfelli, M. Assante, V. Bonvicini, A. Bravin, G. Cantatore, E. Castelli, L. Dalla Palma, M. Di Michiel, R. Longo, A. Olivo *et al.*, "Low-dose phase contrast x-ray medical imaging," *Physics in Medicine & Biology*, vol. 43, no. 10, p. 2845, 1998.

[34] S. K. Davis, B. D. Van Veen, S. C. Hagness, and F. Kelcz, "Breast tumor characterization based on ultrawideband microwave backscatter," *IEEE transactions on biomedical engineering*, vol. 55, no. 1, pp. 237–246, 2008.

[35] M. Klemm, I. Craddock, J. Leendertz, A. Preece, and R. Benjamin, "Breast cancer detection using symmetrical antenna array," 2007.

[36] S. Venkatesh, C. R. Anderson, N. V. Rivera, and R. M. Buehrer, "Implementation and analysis of respiration-rate estimation using impulse-based uwb," in *Military Communications Conference, 2005. MILCOM 2005. IEEE.* IEEE, 2005, pp. 3314–3320.

[37] C. G. Bilich, "Bio-medical sensing using ultra wideband communications and radar technology: A feasibility study," in *Pervasive Health Conference and Workshops, 2006*. IEEE, 2006, pp. 1–9.

[38] Y. Xu, S. Dai, S. Wu, J. Chen, and G. Fang, "Vital sign detection method based on multiple higher order cumulant for ultrawideband radar," *IEEE Transactions on Geoscience and Remote Sensing*, vol. 50, no. 4, pp. 1254–1265, 2012.

[39] B. Schleicher, I. Nasr, A. Trasser, and H. Schumacher, "Ir-uwb radar demonstrator for ultra-fine movement detection and vital-sign monitoring," *IEEE transactions on microwave theory and techniques*, vol. 61, no. 5, pp. 2076–2085, 2013.

[40] J. Sachs, M. Helbig, R. Herrmann, M. Kmec, K. Schilling, and E. Zaikov, "Remote vital sign detection for rescue, security, and medical care by ultra-wideband pseudo-noise radar," *Ad Hoc Networks*, vol. 13, pp. 42–53, 2014.

[41] M. P. Tarvainen, P. O. Ranta-Aho, and P. A. Karjalainen, "An advanced detrending method with application to hrv analysis," *IEEE Transactions on Biomedical Engineering*, vol. 49, no. 2, pp. 172–175, 2002.

[42] J.-P. Niskanen, M. P. Tarvainen, P. O. Ranta-Aho, and P. A. Karjalainen, "Software for advanced hrv analysis," *Computer methods and programs in biomedicine*, vol. 76, no. 1, pp. 73–81, 2004.

[43] M. P. Tarvainen, J.-P. Niskanen, J. A. Lipponen, P. O. Ranta-Aho, and P. A. Karjalainen, "Kubios hrv–heart rate variability analysis software," *Computer methods and programs in biomedicine*, vol. 113, no. 1, pp. 210–220, 2014.

[44] S. Yu, S. Hu, V. Azorin-Peris, J. A. Chambers, Y. Zhu, and S. E. Greenwald, "Motion-compensated noncontact imaging photoplethysmography to monitor cardiorespiratory status during exercise," *Journal of biomedical optics*, vol. 16, no. 7, p. 077010, 2011.

[45] Y. Sun, S. Hu, V. Azorin-Peris, R. Kalawsky, and S. E. Greenwald, "Noncontact imaging photoplethysmography to effectively access pulse rate variability," *Journal of biomedical optics*, vol. 18, no. 6, p. 061205, 2012.

[46] S. Kwon, H. Kim, and K. S. Park, "Validation of heart rate extraction using video imaging on a built-in camera system of a smartphone," in *Engineering in Medicine and Biology Society (EMBC), 2012 Annual International Conference of the IEEE*. IEEE, 2012, pp. 2174–2177.

[47] L. Kong, Y. Zhao, L. Dong, Y. Jian, X. Jin, B. Li, Y. Feng, M. Liu, X. Liu, and H. Wu, "Non-contact detection of oxygen saturation based on visible light imaging device using ambient light," *Optics express*, vol. 21, no. 15, pp. 17 464–17 471, 2013.

[48] D. J. McDuff, J. R. Estepp, A. M. Piasecki, and E. B. Blackford, "A survey of remote optical photoplethysmographic imaging methods," in *Engineering in Medicine and Biology Society (EMBC), 2015 37th Annual International Conference of the IEEE*. IEEE, 2015, pp. 6398–6404.

[49] W. Wang, S. Stuijk, and G. De Haan, "Exploiting spatial redundancy of image sensor for motion robust rppg." *IEEE Trans. Biomed. Engineering*, vol. 62, no. 2, pp. 415–425, 2015.

[50] ——, "A novel algorithm for remote photoplethysmography: Spatial subspace rotation." *IEEE Trans. Biomed. Engineering*, vol. 63, no. 9, pp. 1974–1984, 2016.

[51] Y. Sun and N. Thakor, "Photoplethysmography revisited: from contact to noncontact, from point to imaging," *IEEE Transactions on Biomedical Engineering*, vol. 63, no. 3, pp. 463–477, 2016.

[52] W. Wang, A. C. den Brinker, S. Stuijk, and G. de Haan, "Algorithmic principles of remote ppg," *IEEE Transactions on Biomedical Engineering*, vol. 64, no. 7, pp. 1479–1491, 2017.

[53] B. Miller, "Vital signs of identity [biometrics]," *IEEE spectrum*, vol. 31, no. 2, pp. 22–30, 1994.

[54] E. Greneker, "Radar sensing of heartbeat and respiration at a distance with applications of the technology," 1997.

[55] G. Wang, J.-M. Munoz-Ferreras, C. Gu, C. Li, and R. Gomez-Garcia, "Application of linear-frequency-modulated continuous-wave (lfmcw) radars for tracking of vital signs," *IEEE Transactions on Microwave Theory and Techniques*, vol. 62, no. 6, pp. 1387–1399, 2014.

[56] F. Adib, H. Mao, Z. Kabelac, D. Katabi, and R. C. Miller, "Smart homes that monitor breathing and heart rate," in *Proceedings of the 33rd annual ACM conference on human factors in computing systems*. ACM, 2015, pp. 837–846.

[57] J. Liu, Y. Wang, Y. Chen, J. Yang, X. Chen, and J. Cheng, "Tracking vital signs during sleep leveraging off-the-shelf wifi," in *Proceedings of the 16th ACM International Symposium on Mobile Ad Hoc Networking and Computing*. ACM, 2015, pp. 267–276.

[58] Z. Peng, J. M. Muñoz-Ferreras, Y. Tang, C. Liu, R. Gómez-García, L. Ran, and C. Li, "A portable fmcw interferometry radar with programmable low-if architecture for localization, isar imaging, and vital sign tracking," *IEEE Transactions on Microwave Theory and Techniques*, vol. 65, no. 4, pp. 1334–1344, 2017.

[59] C.-P. Lai and R. M. Narayanan, "Through-wall imaging and characterization of human activity using ultrawideband (uwb) random noise radar," in *Sensors, and Command, Control, Communications, and Intelligence (C3I) Technologies for Homeland Security and Homeland Defense IV*, vol. 5778. International Society for Optics and Photonics, 2005, pp. 186–196.

[60] Y. Wang and A. E. Fathy, "Micro-doppler signatures for intelligent human gait recognition using a uwb impulse radar," in *Antennas and Propagation (APSURSI), 2011 IEEE International Symposium on*. IEEE, 2011, pp. 2103–2106.

[61] J. Li, Z. Zeng, J. Sun, and F. Liu, "Through wall detection of human being's movement by uwb radar," in *International Workshop on Gravity, Electrical & Magnetic Methods and Their Applications 2011: International Workshop on Gravity, Electrical & Magnetic Methods and Their Applications, Beijing, China, October 10–13, 2011*. Society of Exploration Geophysicists, 2011, pp. 71–71.

[62] G. E. Smith, F. Ahmad, and M. G. Amin, "Micro-doppler processing for ultra-wideband radar data," in *Radar Sensor Technology XVI*, vol. 8361. International Society for Optics and Photonics, 2012, p. 83610L.

[63] R. M. Narayanan and M. Zenaldin, "Radar micro-doppler signatures of various human activities," *IET Radar, Sonar & Navigation*, vol. 9, no. 9, pp. 1205–1215, 2015.

[64] N. V. Rivera, S. Venkatesh, C. R. Anderson, and R. M. Buehrer, "Multi-target estimation of heart and respiration rates using ultra wideband sensors." in *EUSIPCO*. Citeseer, 2006, pp. 1–6.

[65] V. M. Lubecke, O. Boric-Lubecke, A. Host-Madsen, and A. E. Fathy, "Through-the-wall radar life detection and monitoring," in *Microwave Symposium, 2007. IEEE/MTT-S International*. IEEE, 2007, pp. 769–772.

[66] O. Boric-Lubecke, A. Host-Madsen, and V. Lubecke, "Determining presence and/or physiological motion of one or more subjects with multiple receiver doppler radar systems," Mar. 27 2008, uS Patent App. 11/803,669.

[67] O. Boric-Lubecke, V. M. Lubecke, B.-K. Park, W. Massagram, and B. Jokanovic, "Heartbeat interval extraction using doppler radar for health monitoring," in *Telecommunication in Modern Satellite, Cable, and Broadcasting Services, 2009. TELSIKS'09. 9th International Conference on*. IEEE, 2009, pp. 139–142.

[68] T. Cheng, G. C. Migliaccio, J. Teizer, and U. C. Gatti, "Data fusion of real-time location sensing and physiological status monitoring for ergonomics analysis of construction workers," *Journal of Computing in Civil engineering*, vol. 27, no. 3, pp. 320–335, 2012.

[69] Y. Wang, Q. Liu, and A. E. Fathy, "Simultaneous localization and respiration detection of multiple people using low cost uwb biometric pulse doppler radar sensor," in *Microwave Symposium Digest (MTT), 2012 IEEE MTT-S International*. IEEE, 2012, pp. 1–3.

[70] G. Ossberger, T. Buchegger, E. Schimback, A. Stelzer, and R. Weigel, "Non-invasive respiratory movement detection and monitoring of hidden humans using ultra wideband pulse radar," in *Ultra Wideband Systems, 2004. Joint with Conference on Ultrawideband Systems and Technologies. Joint UWBST & IWUWBS. 2004 International Workshop on*. IEEE, 2004, pp. 395–399.

[71] J. C. Lin, "Microwave sensing of physiological movement and volume change: A review," *Bioelectromagnetics*, vol. 13, no. 6, pp. 557–565, 1992.

[72] B.-K. Park, O. Boric-Lubecke, and V. M. Lubecke, "Arctangent demodulation with dc offset compensation in quadrature doppler radar receiver systems," *IEEE transactions on Microwave theory and techniques*, vol. 55, no. 5, pp. 1073–1079, 2007.

[73] C. Li and J. Lin, "Complex signal demodulation and random body movement cancellation techniques for non-contact vital sign detection," in *Microwave Symposium Digest, 2008 IEEE MTT-S International*. IEEE, 2008, pp. 567–570.

[74] J. Wang, X. Wang, L. Chen, J. Huangfu, C. Li, and L. Ran, "Noncontact distance and amplitude-independent vibration measurement based on an extended dacm algorithm," *IEEE Transactions on Instrumentation and Measurement*, vol. 63, no. 1, pp. 145–153, 2014.

[75] A. Lazaro, D. Girbau, and R. Villarino, "Analysis of vital signs monitoring using an ir-uwb radar," *Progress In Electromagnetics Research*, vol. 100, pp. 265–284, 2010.

[76] L. Ren, Y. S. Koo, Y. Wang, and A. E. Fathy, "Noncontact heartbeat detection using uwb impulse doppler radar," in *Biomedical Wireless Technologies, Networks, and Sensing Systems (BioWireleSS), 2015 IEEE Topical Conference on*. IEEE, 2015, pp. 1–3.

[77] L. Ren, Y. S. Koo, H. Wang, Y. Wang, Q. Liu, and A. E. Fathy, "Noncontact multiple heartbeats detection and subject localization using uwb impulse doppler radar," *IEEE Microwave and Wireless Components Letters*, vol. 25, no. 10, pp. 690–692, 2015.

[78] L. Ren, H. Wang, K. Naishadham, O. Kilic, and A. E. Fathy, "Phase-based methods for heart rate detection using uwb impulse doppler radar," *IEEE Transactions on Microwave Theory and Techniques*, vol. 64, no. 10, pp. 3319–3331, 2016.

[79] J. Yan, H. Hong, H. Zhao, Y. Li, C. Gu, and X. Zhu, "Through-wall multiple targets vital signs tracking based on vmd algorithm," *Sensors*, vol. 16, no. 8, p. 1293, 2016.

[80] R. A. Fathy, H. Wang, and L. Ren, "Comparison of uwb doppler radar and camera based photoplethysmography in non-contact multiple heartbeats detection," in *Biomedical Wireless Technologies, Networks, and Sensing Systems (BioWireleSS), 2016 IEEE Topical Conference on*. IEEE, 2016, pp. 25–28.

[81] L. C. Andrews and L. C. Andrews, *Special functions of mathematics for engineers*. McGraw-Hill New York, 1992.

[82] E. W. Weisstein, "Bessel function of the first kind," 2002.

[83] N. Chernov and C. Lesort, "Least squares fitting of circles," *Journal of Mathematical Imaging and Vision*, vol. 23, no. 3, pp. 239–252, 2005.

[84] M. Zakrzewski, H. Raittinen, and J. Vanhala, "Comparison of center estimation algorithms for heart and respiration monitoring with microwave doppler radar," *IEEE Sensors Journal*, vol. 12, no. 3, pp. 627–634, 2012.

[85] A. Singh, X. Gao, E. Yavari, M. Zakrzewski, X. H. Cao, V. M. Lubecke, and O. Boric-Lubecke, "Data-based quadrature imbalance compensation for a cw doppler radar system," *IEEE Transactions on Microwave Theory and Techniques*, vol. 61, no. 4, pp. 1718–1724, 2013.

[86] S. Guan, J. A. Rice, C. Li, and C. Gu, "Automated dc offset calibration strategy for structural health monitoring based on portable cw radar sensor," *IEEE Transactions on Instrumentation and Measurement*, vol. 63, no. 12, pp. 3111–3118, 2014.

[87] R. Schmidt, "Multiple emitter location and signal parameter estimation," *IEEE transactions on antennas and propagation*, vol. 34, no. 3, pp. 276–280, 1986.

[88] D. W. Bliss and S. Govindasamy, *Adaptive Wireless Communications: MIMO Channels and Networks*. Cambridge University Press, 2013.

[89] J. Piou, "A state identification method for 1-d measurements with gaps," in *AIAA Guidance, Navigation, and Control Conference and Exhibit*, 2005, p. 5943.

[90] L. Ren, H. Wang, K. Naishadham, Q. Liu, and A. E. Fathy, "Non-invasive detection of cardiac and respiratory rates from stepped frequency continuous wave radar measurements using the state space method," in *Microwave Symposium (IMS), 2015 IEEE MTT-S International*. IEEE, 2015, pp. 1–4.

[91] K. Naishadham, J. E. Piou, L. Ren, and A. E. Fathy, "Estimation of cardiopulmonary parameters from ultra wideband radar measurements using the state space method," *IEEE transactions on biomedical circuits and systems*, vol. 10, no. 6, pp. 1037–1046, 2016.

[92] S.-Y. Kung, K. S. Arun, and D. B. Rao, "State-space and singular-value decomposition-based approximation methods for the harmonic retrieval problem," *JOSA*, vol. 73, no. 12, pp. 1799–1811, 1983.

[93] M. Wax and T. Kailath, "Detection of signals by information theoretic criteria," *IEEE Transactions on Acoustics, Speech and Signal Processing,*, vol. 33, no. 2, pp. 387–392, 1985.

[94] H. Bozdogan, "Model selection and akaike's information criterion (aic): The general theory and its analytical extensions," *Psychometrika*, vol. 52, no. 3, pp. 345–370, 1987.

[95] H.-T. Wu, J.-F. Yang, and F.-K. Chen, "Source number estimator using gerschgorin disks," in *Acoustics, Speech, and Signal Processing, 1994. ICASSP-94., 1994 IEEE International Conference on*, vol. 4. IEEE, 1994, pp. IV–261.

[96] R. O. Schmidt, "A signal subspace approach to multiple emitter location and spectral estimation." 1982.

[97] M. Wax, "Detection and localization of multiple sources via the stochastic signals model," *IEEE Transactions on Signal Processing*, vol. 39, no. 11, pp. 2450–2456, 1991.

[98] N. Andersen, K. Granhaug, J. A. Michaelsen, S. Bagga, H. A. Hjortland, M. R. Knutsen, T. S. Lande, and D. T. Wisland, "A 118-mw pulse-based radar soc in 55-nm cmos for non-contact human vital signs detection," *IEEE Journal of Solid-State Circuits*, vol. 52, no. 12, pp. 3421–3433, 2017.

[99] *Emergency Care for You: ER 101.* American College of Emergency Physicians Foundation, 2014.

[100] M. Singh and G. Ramachandran, "Reconstruction of sequential cardiac in-plane displacement patterns on the chest wall by laser speckle interferometry," *IEEE transactions on biomedical engineering*, vol. 38, no. 5, pp. 483–489, 1991.

[101] C. Li, *Doppler phase modulation effect for non-contact accurate measurement of vital signs and other periodic movements-from theory to CMOS system on chip integrations.* University of Florida, 2009.

[102] L. Feng, L.-M. Po, X. Xu, Y. Li, and R. Ma, "Motion-resistant remote imaging photoplethysmography based on the optical properties of skin," *IEEE Transactions on Circuits and Systems for Video Technology*, vol. 25, no. 5, pp. 879–891, 2015.

[103] Y. Seppenwoolde, H. Shirato, K. Kitamura, S. Shimizu, M. Van Herk, J. V. Lebesque, and K. Miyasaka, "Precise and real-time measurement of 3d tumor motion in lung due to breathing and heartbeat, measured during radiotherapy," *International Journal of Radiation Oncology* Biology* Physics*, vol. 53, no. 4, pp. 822–834, 2002.

APPENDIX A

LIST OF ACRONYMS

APPENDIX A

List of Acronyms

2-D two-dimensional

CW continuous-wave

UWB ultra-wideband

RIPPG remote imaging photoplethymography

PPG photoplethymography

I in-phase component

Q quadrature component

ECG electrocardiogram

CT computerized tomography

HRV Heart rate variability

FM frequency modulated

CSD complex signal demodulation

AD Arctangent demodulation

RF radio frequency

DSP digital signal processing

Log Logarithmic method

DACM differentiate and cross-multiply

LM Levenberg-Marquardt

SSM State-Space method

MUSIC Multiple-Signal Classification

BPM breaths/beats per minute

P2NL peak to noise level

RGB red, green and blue

ROI region of interest

GRD green-red difference signal

SVD singuar-value decomposition

LEDs light-emitting diodes

SNR signal-to-noise ratio

AIC Akaike's information criterion

MDL Minimum Description Length